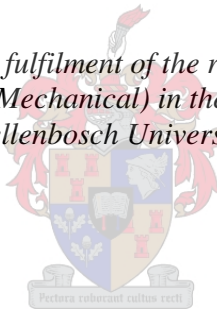


An Investigation of the Effect of Inlet Swirl on the Flow through a Micro-Gas Turbine Combustion Chamber

by
Chenelle Basson

Thesis presented in partial fulfilment of the requirements for the degree of Master of Engineering (Mechanical) in the Faculty of Engineering at Stellenbosch University



Supervisor: Prof. C. J. Meyer

March 2016

DECLARATION

By submitting this thesis electronically, I declare that the entirety of the work contained therein is my own, original work, that I am the sole author thereof (save to the extent explicitly otherwise stated), that reproduction and publication thereof by Stellenbosch University will not infringe any third party rights and that I have not previously in its entirety or in part submitted it for obtaining any qualification.

March 2016

ABSTRACT

An Investigation of the Effect of Inlet Swirl on the Flow through a Micro-Gas Turbine Combustion Chamber

C. Basson

Department of Mechanical and Mechatronic Engineering, Stellenbosch University, Private Bag XI, Matieland 7602, South Africa

Thesis: MEng. (Research), (Mechanical)

March 2016

Previous research on the BMT120-KS micro-gas turbine engine has revealed that there is a component of swirl present at the compressor outlet. The effect of this inlet swirl on the flow through a micro-gas turbine combustion chamber is unknown. This project investigated the influence of the inlet swirl on the mass flow distribution and flow structures within the combustion chamber. An axial or non-swirl flow case was used as a control with which the swirling flow cases could be compared. Computational Fluid Dynamics (CFD) was used to investigate the mass flow distributions and internal flow structures of both the axial and the swirling flow cases. The axial and swirling mass flow distributions were determined experimentally as well. In order to determine the mass flow distribution experimentally with the test rig available at Stellenbosch University, certain assumptions were made. One assumption was that the pressure drop across the liner of the combustion chamber was constant along the liner. It was found that the experimental results validated the numerical results, with no more than 1.5 % difference for most of the sets of holes. The assumption was validated for the outer liner. However, the pressure drop over the inner liner varied with as much as 178 Pa, proving the assumption invalid. The discovery that the assumption was incorrect indicated that the experimental method was not accurate for this combustion chamber. However, it was concluded that the experimental results validated the numerical results, due to the good correlation obtained for the outer liner. The conclusion was made that the flow structures obtained numerically were a fairly accurate representation of the physical flow phenomena. When comparing the swirling flow cases to the axial flow case it was found that inlet swirl had a negligible influence on the mass flow distribution, but did have a negative impact on the flow structures within the combustion chamber. The recirculation zones for the swirling flow cases were not as well defined as for the axial flow case. It is therefore advised that the combustion performance be analysed with inlet swirl, in order to evaluate the effect of inlet swirl on the performance of the combustion chamber.

UITTREKSEL

Die Onderzoek van die Invloed van Dwarrelende Inlaat Vloei op die Vloei deur 'n Mikro-gasturbine Verbrandingskamer

C. Basson

Departement van Meganiese en Megatroniese Ingenieurswese, Stellenbosch Universiteit, Privaatsak XI, Matieland 7602, Suid-Afrika

Tesis: MIng. (Navorsing), (Meganies)

Maart 2016

Reeds bestaande navorsing oor die BMT120-KS mikrogasturbine-enjin het aangedui dat daar dwarrelende vloei by die kompressoruitlaat voorkom. Geen navorsing is tot dusver onderneem om die effek van die dwarrelende vloei te ondersoek nie. Die invloed van dwarrelende inlaatvloei op die massavloei-verspreiding en vloeistrukture in die verbrandingskamer is ondersoek. 'n Aksiale vloei geval (of nie-dwarrel geval) is as kontrole, waarmee die dwarrelende vloei geval vergelyk kon word, gebruik. Numeriese vloedinamika is gebruik om die massavloei-verspreiding en die interne vloeistrukture te bepaal. Die massavloei-verspreiding is ook eksperimenteel bepaal vir beide die aksiale en dwarrelende vloei gevalle. Sekere aannames is gemaak om die massavloei-verspreiding eksperimenteel te kon bepaal, met die fasiliteite beskikbaar by die Universiteit van Stellenbosch. Een van die aannames was dat die drukval oor die verbrandingskamer se wand konstant bly. Die eksperimentele resultate het die numeriese resultate bevestig, met verskille van kleiner as 1.5 % vir die massavloei-verspreiding vir meeste van die stelle gate. Die aanname is bevestig vir die buitewand van die verbrandingskamer, maar is vir die binnewand ongeldig bewys. Drukvalle oor die binnewand het met soveel as 178 Pa gewissel. Daarom is dit afgelei dat die eksperimentele metode wat gebruik is, nie akkuraat vir hierdie verbrandingskamer is nie. Die eksperimentele resultate bevestig wel die numeriese resultate as gevolg van die goeie korrelasie wat vir die buitewand verkry is. Dit het gelei tot die gevolgtrekking dat die vloeistrukture wat numeries voorspel is, wel 'n akkurate voorstelling van die fisiese vloeiverskynsels is. Daar is bevind dat die dwarrelende vloei 'n onbeduidende invloed op die massavloei-verspreiding gehad het, maar dat dit wel 'n beduidend negatiewe invloed op die vloeistrukture gehad het. Die dwarrelende vloei se hersirkulasiesones is nie so goed gedefinieer soos in die geval van die aksiale vloei nie. Dit word aanbeveel dat die verbrandingswerkverrigting ontleed word, met dwarrelende inlaatvloei, om soedoende die effek van die dwarrelende inlaatvloei op die werkverrigting van die verbrandingskamer te evalueer.

ACKNOWLEDGEMENTS

I would like to thank my supervisor, Prof. C. J. Meyer, for his encouragement and advice during the course of this project. I would also like to thank Mr C. Zietsman and Mr F. Zietsman for their assistance and suggestions, as well as the entire workshop staff for their friendliness and helpfulness. I would also like to thank my family and friends for their unwavering support.

TABLE OF CONTENTS

	Page
LIST OF FIGURES	vii
LIST OF TABLES	x
NOMENCLATURE	xii
1. INTRODUCTION	1
1.1. Background.....	2
1.2. Objectives and Scope.....	6
2. LITERATURE REVIEW	6
2.1. Flow Through the Combustion Chamber	9
2.1.1. Sizing and overall pressure loss	9
2.1.2. Flow through the liner holes	10
2.1.3. Jet penetration and mixing	10
2.2. Previous Work	11
2.3. Inlet Guide Vane Aerodynamics	12
3. FLOW DISTRIBUTION EXPERIMENT	13
3.1. Experimental Procedure	14
3.2. Calculations	20
4. INLET GUIDE VANE DESIGN AND MANUFACTURE	22
4.1. Inlet Guide Vane Design	22
4.1.1. Blade design.....	22
4.1.2. Hub and shroud design.....	28
4.2. Inlet Guide Vane Manufacture	32
4.2.1. Blade manufacture	32
4.2.2. Hub and shroud manufacture	32
4.2.3. Miscellaneous parts.....	33
4.2.4. Assembly.....	33
5. FLOW SIMULATION.....	37
5.1. Material Properties	40
5.2. Computational Domain	41
5.3. Boundary Conditions.....	45

5.3.1.	Axial flow simulation.....	45
5.3.2.	Swirling flow simulation.....	47
5.4.	Solvers and Numerical Schemes	48
5.5.	Computational Mesh	51
5.5.1.	Axial flow simulation.....	52
5.5.2.	Swirling flow simulations	59
6.	DISCUSSION AND RESULTS	61
6.1.	Comparison of Numerical Results with Experimental Flow Distribution Results for the Axial Flow Cases.	65
6.2.	Comparison of the Swirling Flow Case to the Axial Flow Case.....	72
7.	CONCLUSIONS	76
7.1.	Findings and Implications	77
7.2.	Recommendations	78
	REFERENCES	79
	APPENDIX A: TECHNICAL DRAWINGS	A.1
A.1.	Inlet Guide Vane Technical Drawings	A.1
A.2.	Computational Domain Technical Drawings	A.4
	APPENDIX B: CASE FILES FOR FLOW SIMULATIONS.....	B.1
B.1.	Case Files for the Axial Flow Case	B.1
B.1.1.	0 directory	B.1
B.1.2.	constant directory.....	B.3
B.1.3.	system directory	B.6
B.2.	Case Files for the Swirling Flow Case	B.12
	APPENDIX C: DETAILED TUTORIAL ON HOW THE MESH WAS CREATED.....	C.1
	APPENDIX D: RESULTS	D.1
D.1.	Experimental Results.....	D.1
D.2.	Numerical Results	D.3
	APPENDIX E: CALIBRATION PROCEDURES	E.1
E.1.	Pressure Transducers	E.1
E.2.	Thermocouples.....	E.3
E.3.	Orifice Plate	E.4
	APPENDIX F: LEAKAGE INVESTIGATION.....	F.1

LIST OF FIGURES

	Page
Figure 1: Typical layout of a gas turbine engine modified from Çengel and Boles (2006: 532).....	1
Figure 2: T-s diagram of the brayton cycle modified from Çengel and Boles (2006: 518).....	2
Figure 3: BMT120-KS engine, taken from Baird Micro Turbines (2015).	3
Figure 4: CAD model of the BMT120-KS combustion chamber.....	4
Figure 5: Diagram of airflow through the combustion chamber.	5
Figure 6: Quarter section view of the primary-, secondary- and dilution zones in a combustion chamber.	7
Figure 7: Air distribution in a typical combustion chamber modified from Boyce (2002: 35).....	8
Figure 8: Diagram describing the three different types of combustion chambers...8	8
Figure 9: Cascade nomenclature modified from Sayers (1990: 301).	12
Figure 10: Schematic diagram of the combustion test rig.	14
Figure 11: Diagrammatic representation of the mass flow distribution through the combustion chamber.	15
Figure 12: Hole-set designations for combustion chamber.	16
Figure 13: Photo of the experimental configuration used to determine the mass flow through hole-set A4.	17
Figure 14: Diagram of the geometry of an orifice meter.	20
Figure 15: Blade profiles and radii of the inlet guide vanes.	23
Figure 16: Geometry used to calculate IGV-blade chord lengths.	24
Figure 17: Aerofoil R7 mm camber line.	25
Figure 18: Geometry used to calculate α_2'	26
Figure 19: Illustration of the hub relative to the diffuser.....	29
Figure 20: Assembly of the adapter nozzle and the combustor housing.	30
Figure 21: Shroud design.....	30
Figure 22: Inlet guide vane assembly.	31
Figure 23: Assembly of the inlet guide vane assembly and the diffuser.	31
Figure 24: Exploded view of the test section assembly with inlet guide vanes.....	32
Figure 25: Manufactured hub and shroud.....	33
Figure 26: Alignment of inlet guide vanes.	33

Figure 27: The manufactured R7 and R9 inlet guide vanes.	34
Figure 28: Photo of the inlet guide vane fastened to the diffuser.	35
Figure 29: Visualised swirl angle for the R7 swirler.	36
Figure 30: Computational domain for the axial case.	42
Figure 31: Computational domains of (a) R7 IGV and a close up view of the R7 IGV (b).	43
Figure 32: Computational domains of (a) R9 IGV and a close up view of the R9 IGV (b).	44
Figure 33: Graphical representation of the boundary conditions for the axial flow case.	45
Figure 34: Graphical representation of the boundary conditions for the swirling flow case.	47
Figure 35: Flow diagram depicting the PISO algorithm.	49
Figure 36: Initial blockMesh mesh for the axial case.	53
Figure 37: Cell orthogonality.	54
Figure 38: Cell skewness.	55
Figure 39: y^+ values on the casing walls.	56
Figure 40: y^+ values on the inner liner.	56
Figure 41: y^+ values on the outer liner.	57
Figure 42: y^+ values on the inside of the vaporizer tubes.	57
Figure 43: y^+ values turbine shaft.	58
Figure 44: Comparison of mass flow through the vaporizer tubes and cooling holes obtained for a coarse mesh, a medium mesh and a fine mesh.	59
Figure 45: Initial blockMesh mesh for the swirling simulation.	60
Figure 46: Mass flow percentage for hole-set A5 for forward cases (Ax1-Ax7). ..	62
Figure 47: Mass flow percentage for hole-set A5 for inverse cases (Ax1-Ax7). ..	62
Figure 48: Recirculation zone for the Ax7 case.	65
Figure 49: Mass flow fluctuations over time for hole-set B3 for the Ax4 case.	66
Figure 50: Pressure distribution through the combustor for the Ax7 case.	68
Figure 51: The constant relation between the pressure drop over the system and the pressure drop over the liner.	70
Figure 52: Recirculation zone produced under operating conditions.	72
Figure 53: Comparison of the mass flow over time through hole-set B3 of the Ax4 case, R7.4 case and the R9.4 case.	75

Figure 54: Recirculation zone produced in the R7.7 case.	76
Figure A. 1: Inlet guide vane and diffuser assembly.	A.1
Figure A. 2: Inlet guide vane assembly.	A.1
Figure A. 3: Flange acting as shroud	A.2
Figure A. 4: Sleeve acting as hub.	A.2
Figure A. 5: Modified diffuser.	A.3
Figure A. 6: Back plate.	A.3
Figure A. 7: Test section assembly.	A.4
Figure A. 8: Relevant adapted nozzle dimensions.	A.4
Figure A. 9: Relevant outer liner dimensions.	A.5
Figure A. 10: Relevant inner liner dimensions.	A.5
Figure A. 11: Relevant vaporizer tubes dimensions.	A.6
Figure A. 12: Relevant combustion chamber inlet section dimensions.	A.6
Figure A. 13: Relevant combustion chamber housing dimensions.	A.7
Figure A. 14: Relevant exhaust dimensions.	A.7
Figure B. 1: All necessary .stl files.	B.6
Figure C. 1: Shape required for circular hexahedral mesh.	C.1
Figure C. 2: Numbered vertices of blockMesh.	C.1
Figure C. 3: Boundary patches as defined in blockMeshDict.	C.2
Figure D. 1: Recirculation zone of the R9 case.	D.7
Figure E. 1: Calibration curve for Cerabar pressure transducer.	E.2
Figure E. 2: Calibration curve for Deltabar pressure transducer.	E.2
Figure E. 3: Comparison of thermocouple measurements to the platinum thermometer measurements.	E.3
Figure F. 1: Measures taken to reduce leakages (a) Epoxy seal inside combustor (b) Epoxy seal on the outside of the combustor (c) Window sealant used to seal flanges (d) Gaskets used where frequent disassembly is necessary.	F.1

LIST OF TABLES

	Page
Table 1: Specifications and performance data of the BMT120-KS micro turbine engine.....	4
Table 2: General values for pressure losses in combustion chambers modified from Lefebvre and Ballal (2010: 116).	9
Table 3: Variables that were measured during the flow distribution procedure....	15
Table 4: Full Scale Uncertainty of the Pressure Transducers.	18
Table 5: Test matrix.....	19
Table 6: Blade outlet flow angles for varying radii.	28
Table 7: Comparison of the calculated and measured outlet flow angles.	36
Table 8: Equations necessary for the calculation of μt	39
Table 9: Constants for modified eddy dissipation rate equation.	39
Table 10: Fluid properties.....	41
Table 11: Boundary conditions for the axial flow case.	46
Table 12: Summary of the inlet velocities and outlet pressures for all axial flow simulations.....	47
Table 13: Summary of the inlet velocities and outlet pressures for all swirling flow simulations.....	48
Table 14: fvSchemes dictionary settings.	51
Table 15: y^+ values of interest for axial flow.....	58
Table 16: y^+ values of interest for swirling flow.....	61
Table 17: Axial flow mass flow percentage through each set of holes along with their area percentages.....	63
Table 18: Comparison of area percentage and mass flow percentage of hole-sets open to outer annulus.	64
Table 19: Comparison of area percentage and mass flow percentage of hole-sets open to inner annulus.	64
Table 20: Mass flow distribution as predicted by the numerical simulation compared to the experimental results.	67
Table 21: Pressure difference through the hole-sets for the Ax7 case.....	69
Table 22: Pressure drop over the combustion chamber compared to the pressure drop over the entire system for the axial cases.....	70

Table 23: Mass flow distribution through the combustion chamber at operating conditions.....	71
Table 24: Experimental average mass flow distribution of the swirling cases compared to the axial case.	73
Table 25: Comparison of the numerical results and experimental results for swirling flow R7 cases.	74
Table D. 1: Experimental mass flow distribution for each of the axial cases.....	D.1
Table D. 2: Experimental mass flow distribution for each of the R9 cases.....	D.2
Table D. 3: Experimental mass flow distribution for each of the R7 cases.....	D.3
Table D. 4: Numerical mass flow distribution for each of the axial cases.	D.4
Table D. 5: Numerical mass flow distribution for each of the R9 cases.	D.5
Table D. 6: Numerical mass flow distribution for each of the R7 cases.	D.6
Table E. 1: Uncertainty of the Pressure Transducers.....	E.1
Table E. 2: Uncertainties for the small orifice plate.	E.5
Table F. 1. Reduced leakages.	F.2
Table F. 2: Leakages repeatability.	F.2

NOMENCLATURE

A	Area
a	The distance along the chord to the point of maximum camber
C_d	Discharge coefficient
C	Blade tip velocity
$C_{1\varepsilon}$	Constant
c	Chord length
D	Pipe diameter
d	Orifice diameter
i	Used to indicate index
i_a	Incidence angle
k	Turbulent kinetic energy
L	Arc length
L_1	Quotient of the distance of the upstream tapping from the upstream face of the plate and the pipe diameter.
L'_2	Quotient of the distance of the downstream tapping from the downstream face of the plate and the pipe diameter.
l_1	Distance of the upstream pressure tapping to the orifice plate.
l_2	Distance of the downstream pressure tapping to the orifice plate.
\dot{m}	Mass flow
\dot{m}_k	Mass flow of hole set k
\dot{m}_{tot}	Mass flow through the combustion chamber with all holes open.
n	Number of sets of holes in the combustor.
P	Pressure
P_{amb}	Ambient pressure.
P_d	Pressure downstream of the orifice plate
P_k	Generation of turbulence kinetic energy due to the mean velocity gradients
P_u	Pressure upstream of the orifice plate.
R	Universal gas constant of air. Radius where specified.

Re_D	Reynolds number with respect to the pipe diameter.
S	Source terms
s	Blade pitch. Mesh skewness where specified.
T	Temperature.
T_{amb}	Ambient temperature.
T_u	Temperature upstream of the orifice plate.
t	Time
u	Velocity in the x-direction
v	Velocity in the y-direction
w	Velocity in the z-direction
x	Direction/variable in said direction
x_{end}	Last value of x in an in the x-array
x_l	X-component of the line running parallel to the trailing edge of the blade
y	Direction/variable in said direction
y_{end}	Last value of y in an the y-array
y_l	Y-component of the line running parallel to the trailing edge of the blade
z	Direction/variable in said direction

Greek symbols

α	Blade tip flow angle to the axial flow direction.
α'	Angle of the camber line to the axial flow direction.
β	Bleed ratio or diameter ratio
Δ	Used to indicate difference between two values.
δ	Deviation angle
E	Expansibility factor
ε	Turbulence dissipation rate
ζ	Blade stagger angle
θ	Blade camber angle

κ	Specific heat ratio of air.
μ	Dynamic viscosity
μ_a	Dynamic viscosity of air.
ν	Kinematic viscosity
ξ	Angle of circular section
ρ	Density
σ_k	Constant
σ_ε	Constant

Subscripts

o	Orifice
1	Inlet
2	Outlet
t	Turbulent

Abbreviations

<i>CAD</i>	Computer Aided Design
<i>CFD</i>	Computational Fluid Dynamics
<i>CSIR</i>	Council for Scientific and Industrial Research
<i>NREC</i>	Northern Research and Engineering Corporation
<i>PSP</i>	Pressure Sensitive Paint
<i>PZ</i>	Primary Zone
<i>SZ</i>	Secondary Zone
<i>TZ/DZ</i>	Tertiary Zone/Dilution Zone
<i>UAV</i>	Unmanned Aerial Vehicle

1. INTRODUCTION

A gas turbine engine is an internal combustion engine that converts gaseous or liquid fuels to mechanical energy. According to Boyce (2002: 3) the gas turbine can be perceived as a power plant with a large power to weight ratio. Therefore, gas turbine engines are used in many applications, such as power generation and aeroplane propulsion. General Electric for instance has a large range of industrial gas turbines for power generation (2015b).

Rolls Royce also has a large range of gas turbine engines for power generation as well as for civil aerospace applications. Some of their aerospace engines include models such as the Trent 7000, designed exclusively for the Airbus A330. The Trent 7000 engine delivers between 300 - 320 kN of thrust (2015c).

Gas turbine engines are popular, because they not only have a high power to weight ratio, when compared with the equivalent reciprocating engine, but they also have less moving parts and consequently less vibrations than their reciprocating engine equivalents. Therefore research on these engines is abundant.

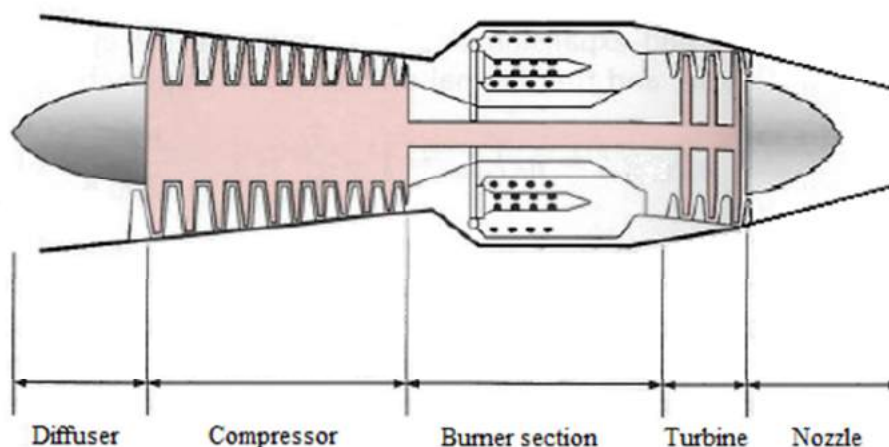


Figure 1: Typical layout of a gas turbine engine modified from Çengel and Boles (2006: 532)

Figure 1 shows the layout of a gas turbine engine. These engines typically consist of a compressor, a combustor and a turbine. The air enters the compressor and is compressed. Fuel is then added to the air and combustion occurs heating the air, rapid expansion forces the air over the turbine blades and causes them to turn, generating energy and rejecting heat. This sequence is called the Brayton cycle. (Çengel and Boles, 2006).

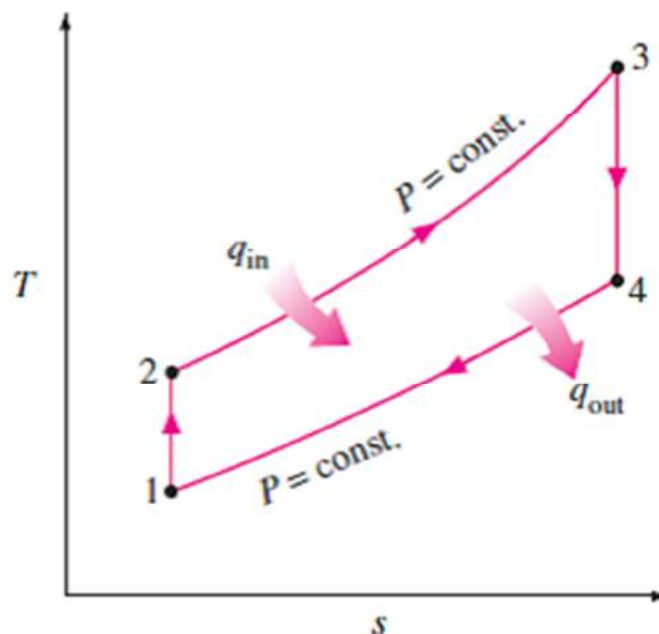


Figure 2: T-s diagram of the brayton cycle modified from Çengel and Boles (2006: 518)

Figure 2 illustrates the T-s diagram of the ideal Brayton cycle describing the governing reactions inside large and small scale gas turbines. Recently, however more interest has been shown in smaller scale gas turbine engines, also called micro-gas turbine engines.

Micro-gas turbine engines have an added requirement of being extremely compact. This requirement has led to many small, but significant differences. As can be seen in Figure 1, large scale engines typically have multiple stages of axial compressors and turbines, in the case of the micro-gas turbine engines however, a single compressor and a single turbine is generally used according to Boyce (2002: 25).

1.1. Background

Micro-gas turbine engines have recently become increasingly popular due to the advances in the distributed generation market. (Boyce, 2002).

Interest has not only piqued as a result of the use of the micro-gas turbines in the distributed generation market, but also due to the success of the use of these engines for propulsion of unmanned aerial vehicles (UAV's). UAV's are gaining interest for their uses in military applications, surveillance and even in agriculture.

According to Business-Insider (2015: 1) the growing global UAV industry has been very active producing hard- and software for a long list of clients. These clients range from small companies in agriculture, land management, energy and

construction, and recently large defence and industrial conglomerates have joined the list.

The Council for Scientific and Industrial Research (CSIR) has noticed the lack of such an industry in South Africa and have created an overarching project in order to develop a micro-gas turbine engine and the skills and knowledge needed to design these engines in South Africa. The overarching project involves all aspects of the design and development of such a micro-gas turbine engine.

Many smaller projects involving specific components were initiated at various universities in order to achieve this goal. These projects included the design of central compressor impellers by de Villiers (2014) and van der Merwe (2012) respectively, the evaluation of the performance of a centrifugal compressor diffuser by Krige (2013) and the investigation of the vaporizer tubes of the BMT120-KS engine by Olivier (2015).

One of the micro-gas turbine engines that the CSIR has been researching is the BMT120-KS engine. This engine was developed by Baird Micro Turbines for use in model aircrafts. Figure 3 shows the BMT120-KS engine.



Figure 3: BMT120-KS engine, taken from Baird Micro Turbines (2015).

A computer aided design (CAD) model of the combustion chamber is shown in Figure 4.



Figure 4: CAD model of the BMT120-KS combustion chamber

The BMT120-KS is a Single Fuel Autostart Micro Turbine. It consists of an annular combustion chamber, a single stage turbine and a centrifugal compressor at the inlet. The BMT120-KS has the following specifications and performance data as published by Baird Micro Turbines (2015) and shown in Table 1.

Table 1: Specifications and performance data of the BMT120-KS micro turbine engine.

Maximum Thrust	150 N
Thrust at 125 krpm	125 N
Thrust at 35 krpm	5 N
Rated rpm	120 000 rpm
Max rpm	135 000 rpm
Min rpm	30 000 rpm
Idle rpm	34 000 rpm
EGT	625 °C
Ambient operating limits	5 °C - 45 °C

The flow through the combustion chamber is highly complex consisting of various flow phenomenon including recirculation, flow separation and jets. It is useful to visualise the flow from the compressor outlet to the turbine inlet.

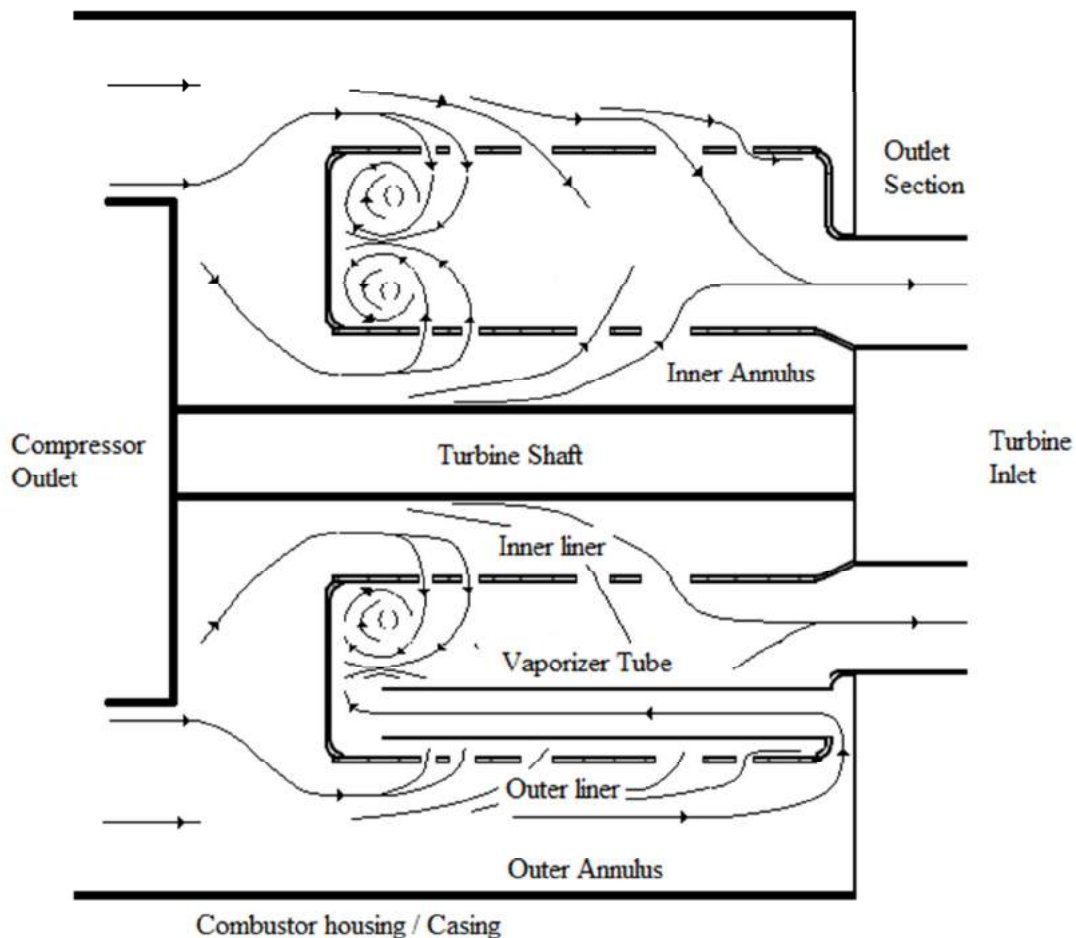


Figure 5: Diagram of airflow through the combustion chamber.

Figure 5 shows a cross section of the flow through the combustion chamber and casing from the compressor outlet to the turbine inlet. Only one vaporizer tube is shown in Figure 5 in order to visualise the flow behind the vaporizer tubes.

It has been discovered that there may be a component of swirl present at the inlet of the combustor originating from the centrifugal compressor. Giving rise to the question: “What effect does inlet swirl have on the flow through a micro-gas turbine combustion chamber?”

This project was initiated in order to research the effect of inlet swirl on the mass flow distribution and the flow structures within the combustor. An axial flow case was used as a control with which the swirling flow cases could be compared. Computational fluid dynamics (CFD) was used to investigate the mass flow distributions and internal flow structures of both the axial and swirling flow cases. The axial and swirling mass flow distributions were also determined experimentally. The CFD results were validated with the experimental results.

1.2. Objectives and Scope

The goal of this project was to develop a functioning numerical model of the non-reacting flow through the combustion chamber for the BMT120-KS micro-gas turbine engine in openFOAM in order to determine the effect of inlet swirl on the mass flow distribution and flow structures within the combustor. An axial flow or non-swirl model served as a control with which the swirling flow models could be compared. The following two models had two varying degrees of swirl in order to determine whether the degree of inlet swirl had an influence on the results. All three of the numerical models were validated with experiments. The following objectives were completed in order to achieve the goal of this project:

- Determine the mass flow distribution through the combustion chamber experimentally for both the axial and swirling flow cases.
- Determine the mass flow distribution through the combustion chamber numerically using openFOAM for both the axial and swirling flow cases.
- Determine what impact the swirling inlet flow has on the mass flow distribution and flow structures within the combustion chamber.

The scope of this project includes understanding and researching micro-gas turbine engine combustion chambers and the various aerodynamic aspects thereof. The scope does not include an investigation with regards to turbulence models etc. This project focuses on the non-reacting flow through the combustor, and does not consider combustion and the various aspects thereof.

2. LITERATURE REVIEW

There are many different types of combustion chambers, but the general layouts of most combustion chambers are similar. It consists of a casing that houses the combustion chamber and a liner through which air can enter the combustion zone. The combustion chamber has three main functions and can be divided into zones where these functions are performed. The three zones are called the primary zone (PZ), the secondary zone (SZ) and the tertiary or dilution zone (TZ/DZ). The primary, secondary and dilution zones can be seen in Figure 6.

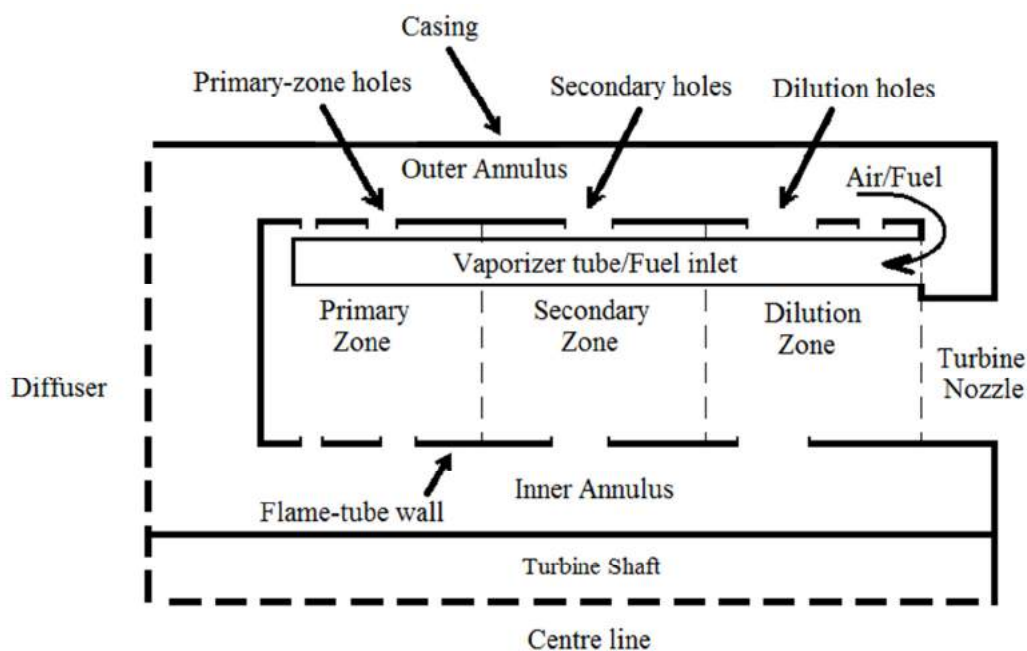


Figure 6: Quarter section view of the primary-, secondary- and dilution zones in a combustion chamber.

The main function of the primary zone is to facilitate complete combustion. Therefore the velocity of the airflow is drastically decreased before this region and a recirculation zone is created in order to anchor the flame. In the secondary zone additional air is introduced cooling down the combustion gasses slightly, encouraging burnout of soot and allowing the combustion of any unburned hydrocarbons. The dilution zone's main use is to introduce even more cold air, creating a temperature profile that is symmetric. This is necessary to reduce unwanted strain on the turbine blades caused by steep temperature gradients in the tangential direction. (Lefebvre and Ballal, 2010).

The primary, secondary and dilution zones need to satisfy the flow distribution requirements to meet burning, dilution and cooling demands (NREC, 1980). According to Boyce (2002: 35) a typical combustion chamber's primary zone requires 28 % of the flow, while the secondary and dilution zones require the further 72 % as can be seen in Figure 7

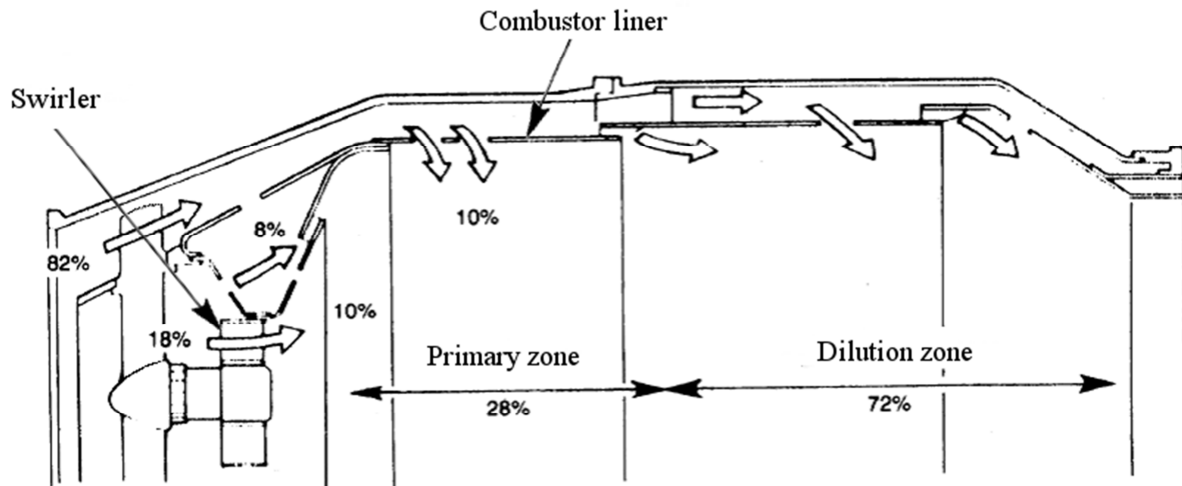


Figure 7: Air distribution in a typical combustion chamber modified from Boyce (2002: 35).

Figure 7 also shows that 18 % of the primary zone air enters the combustion chamber through the swirler and fuel nozzle. In the case of the combustion chamber studied for this project, however, vaporizer tubes are used for fuel delivery, instead of a swirler.

There are three different types of combustion chambers. These include annular, can and tuboannular types shown below in Figure 8.

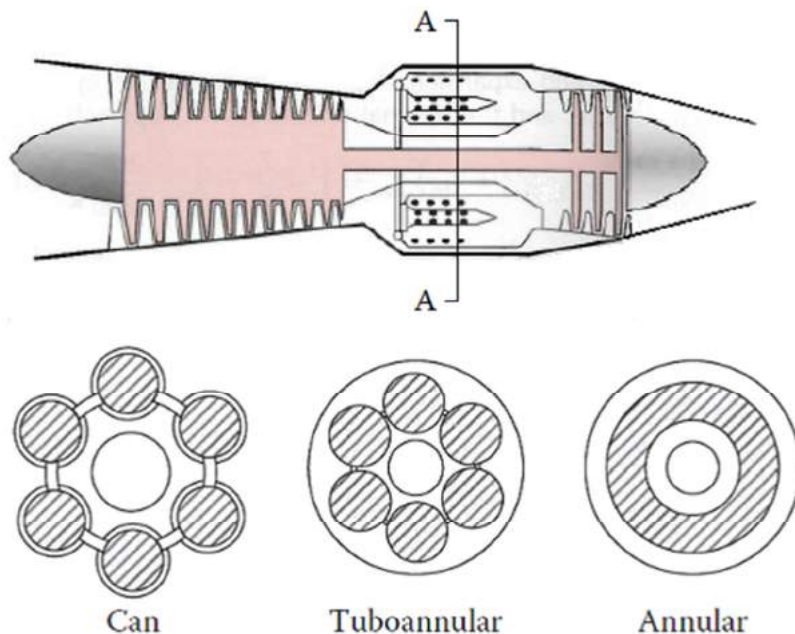


Figure 8: Diagram describing the three different types of combustion chambers

In Figure 8, the shaded area represents the combustion zone. The type of combustion chamber analysed in this project is annular, therefore only annular combustion chambers will be discussed further. An annular liner is mounted concentrically in an annular casing creating both an inner and outer annulus from which the air enters the combustion chamber.

Annular combustion chambers have many advantages above the other types of combustion chambers according to Lefebvre and Ballal (2010: 116).

Table 2: General values for pressure losses in combustion chambers modified from Lefebvre and Ballal (2010: 116).

Type of Chamber	Overall pressure loss	Pressure loss-factor (Equivalent to drag coefficient)
Can	0.07	37
Tuboannular	0.06	28
Annular	0.06	20

As can be seen from Table 2, annular combustion chambers generally exhibit lower overall pressure losses and resistance to flow and can therefore be designed more compactly than other types of combustion chambers which makes it ideal for the micro-gas turbine industry.

One of the biggest drawbacks of annular combustion chambers according to Lefebvre and Ballal (2010: 12) is that a large buckling load is applied to the combustion chamber, calling for stronger materials. In the micro-gas turbine industry however, not as much thrust is needed as for large scale turbine engines and therefore the applied load is not as high.

2.1. Flow Through the Combustion Chamber

The flow through the combustion chamber is highly complex consisting of various flow phenomenon including recirculation, flow separation and jets. In order to analyse the air flow, different aspects must be considered individually. The aspects considered in this document include, the sizing and overall pressure loss and the flow distribution through the liner holes and jets.

2.1.1. Sizing and overall pressure loss

There are two important dimensionless quantities to consider, when designing combustion chambers. The first is termed the overall pressure loss, normally quoted as a percentage, and the second is called the pressure-loss factor. (Lefebvre and Ballal, 2010).

A higher pressure loss over the liner contributes to the combustion and dilution requirements by creating high injection velocities, steep penetration angles and a high level of turbulence. These factors contribute to mixing which can have a shorter liner as an outcome. On the other hand, the pressure loss over the diffuser does not contribute to combustion and should be kept as small as possible using diffuser design principles according to Lefebvre and Ballal (2010: 117).

2.1.2. Flow through the liner holes

The flow distribution through the liner holes governs the combustion chamber's performance. If the velocity through the PZ holes is too high, flame stabilisation will not be established and blow out will occur. If the jet penetration through the PZ holes is too low a recirculation zone will not be created and performance will be negatively affected. SZ cooling requirements will not be met if the mass flow through those holes is too low and if the dilution zone does not receive enough mass flow an undesirable temperature profile will result and the turbine will be exposed to unnecessarily high stresses due to high temperature gradients in the tangential direction. Clearly it is of utmost importance to be able to determine the mass flow distribution through the liner holes in order to evaluate preliminary combustion chamber designs.

According to Lefebvre and Ballal (2010: 120) the mass flow through a liner hole depends on many factors which influence the effective flow area. These factors include the size of the hole and the pressure drop across it as well as the duct geometry and flow conditions around the hole. Lefebvre and Ballal (2010: 120) go on to develop a method for calculating the mass flow through the liner holes. The method requires knowledge of the total pressure upstream of the hole, the static pressure downstream of the hole and the discharge coefficient of the hole.

A similar, but more accurate method for the determination of the mass flow through combustion chamber liner holes was developed by Adkins and Gueroui (1986: 491-497). This method stems from the method developed by Lefebvre and Ballal (2010: 120).

2.1.3. Jet penetration and mixing

Jet flow through the combustion chamber holes is highly influential to the performance of the combustion chamber. As previously mentioned the outlet temperature distribution must be symmetrical in order to be acceptable to the turbine. Therefore the jet penetration and mixing that occurs in the dilution zone is of prime importance.

Downstream of the dilution holes, vortex systems dominate the flow and cause entrainment and mixing of dilution air and main stream gas. When multiple round jets penetrate a tubular liner, the penetration is much lower than it would be for a single jet. This is due to the blockage effect caused by a local increase in mainstream velocity. (Lefebvre and Ballal, 2010).

Mixing rates in general are influenced by a few key factors including momentum flux ratio, length of mixing path, the number and size of the jets as well as the initial jet angle (Lefebvre and Ballal, 2010).

2.2. Previous Work

In a study done by Gieras and Stankowski (2012: 68-79) a computational model of the non-reacting flow through a GMT-120 turbojet engine using a gas dynamic calculation of the theoretical engine cycle as the boundary conditions was created. First only the non-reacting flow through the GTM-120 engine was modelled, and then a heat source was added to give an indication of the combustion and mixing results.

Gieras and Stankowski (2012: 68-79) used a Realizable $k-\epsilon$ turbulence model to simulate the flow, since it had a reasonable computational time and reached convergence. First the operating conditions as given by the manufacturer were used and later on adapted boundary conditions, using a gas dynamic calculation of the theoretical engine cycle, were used which delivered more realistic results. The results concluded that the total pressure loss in this combustion chamber was roughly 10 %. This is large and is due to the scale of the combustion chamber. They suggested that the pressure loss can be improved by optimizing the geometry of the combustion chamber. The pressure loss over the combustion chamber increased drastically with an increase of mass flow rate.

It was concluded that the addition of a heat source in the model did not disturb the flow, but gave a good indication of what would happen during combustion. Gieras and Stankowski (2012: 68-79) also concluded that the Realizable $k-\epsilon$ model delivered good results.

In a study done by Zhu et al. (1995: 252-260) to investigate penetration and mixing of radial jets in neck-down cylindrical crossflow, one of the conclusions they made is that swirling flow does increase the pressure drop over the combustion chamber liner, but does not facilitate mixing. They state that the penetration impedance and diversion that the jets suffer from the swirling flow is most likely the cause.

During a numerical investigation using CFD, the turbulence model used has a large effect on the results. A paper discussing the most accurate turbulence models for simulating flow through micro turbine combustion chambers was authored by Gonzalez Toro et al. (2008: 407-422). They determined that of the RANS models investigated, only the Realizable $k-\epsilon$ model converged for their mesh, but incorrect results were obtained for the temperature distribution. They concluded that micro-gas turbine combustion chambers are most accurately modelled using the LES-WALES turbulence model.

Karthik (2011: 45) agreed with Gonzalez Toro et al. (2008: 407-422) with regards to the capabilities of the Realizable $k-\epsilon$ turbulence model. Karthik (2011: 45) elaborated by saying the Realizable $k-\epsilon$ turbulence model is preferential for

modelling jet impingement, separating flows, swirling flows, secondary flows and that it also resolves the round-jet anomaly.

2.3. Inlet Guide Vane Aerodynamics

In order to induce swirl experimentally, it was decided to design and manufacture inlet guide vanes. The cascade theory of axial flow compressors was consulted to understand the inlet guide vane aerodynamics. The cascades in both the axial flow compressor and inlet guide vanes have the same behaviour. Figure 9 shows the applicable cascade nomenclature.

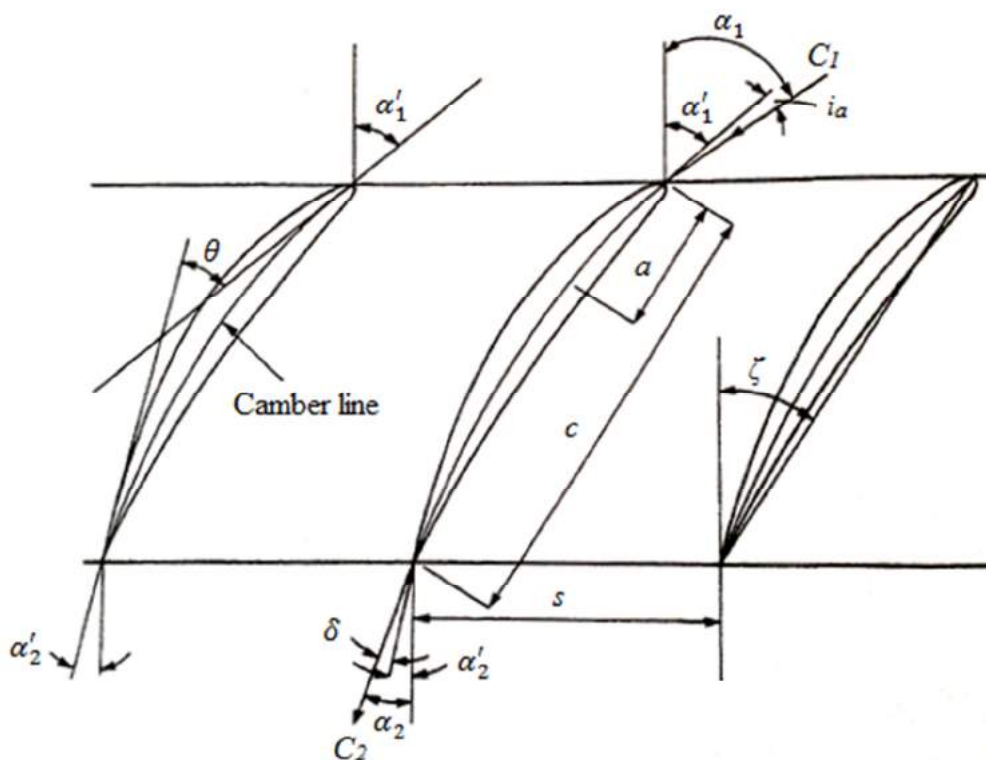


Figure 9: Cascade nomenclature modified from Sayers (1990: 301).

From Figure 9 the camber line, the angle of the camber line relative to the axial direction of the flow at the inlet and outlet (inlet α'_1 and outlet α'_2 camber angles), the blade camber angle θ , the chord length c , the stagger angle ζ , the pitch s , the incident angle i_a , the deviation angle δ , the distance along the chord to the point of maximum camber a and the inlet and outlet velocities C_1 and C_2 and their inlet and outlet angles with respect to the axial direction α_1 and α_2 can be visualised.

The chord length can be defined as the distance between the inlet and the trailing edges of the blade. The stagger angle is the angle between the axial direction and the chord, as shown in Figure 9.

According to Sayers (1990: 301) the following equations describe the blade attributes mentioned. The blade camber angle can be described as follows:

$$\theta = \alpha'_1 - \alpha'_2 \quad (2.1)$$

In Equation 2.1 θ represents the blade camber angle and α'_1 and α'_2 represent the inlet and outlet camber angles respectively. The angle of incidence is defined as the difference between the angle of the inlet velocity and the inlet angle tangent to the camber line:

$$i_a = \alpha_1 - \alpha'_1 \quad (2.2)$$

In Equation 2.2 α_1 represents the angle of the inlet velocity with respect to the axial direction of the flow.

The deviation angle is described as the difference between the angle that the outlet velocity leaves the blade and the tangent to the outlet camber angle:

$$\delta = \alpha_2 - \alpha'_2 \quad (2.3)$$

In Equation 2.3 α_2 represents the angle of the outlet velocity with respect to the axial direction of the flow. The deviation angle is caused by the air not remaining attached to the trailing edge of the blade and can also be calculated as follows:

$$\delta = m\theta \left(\frac{s}{c}\right)^{\frac{1}{2}} \quad (2.4)$$

Where m is represented by the following equation:

$$m = 0.23 \left(\frac{2a}{c}\right)^2 + 0.1 \left(\frac{\alpha_2}{50}\right) \quad (2.5)$$

The previous equations describe the aerodynamics of the blade in a cascade and were used to determine the air outlet angles for two inlet guide vane blade designs.

3. FLOW DISTRIBUTION EXPERIMENT

The flow distribution experiment entails using a test rig to induce flow at different mass flow rates through the combustion chamber while measuring certain

variables. This procedure is used to calculate the percentage of mass flow through each set of holes of the combustion chamber in order to determine whether the primary, secondary and dilution zones have the required flow distribution to meet burning, dilution and cooling demands NREC (1980: 3.1).

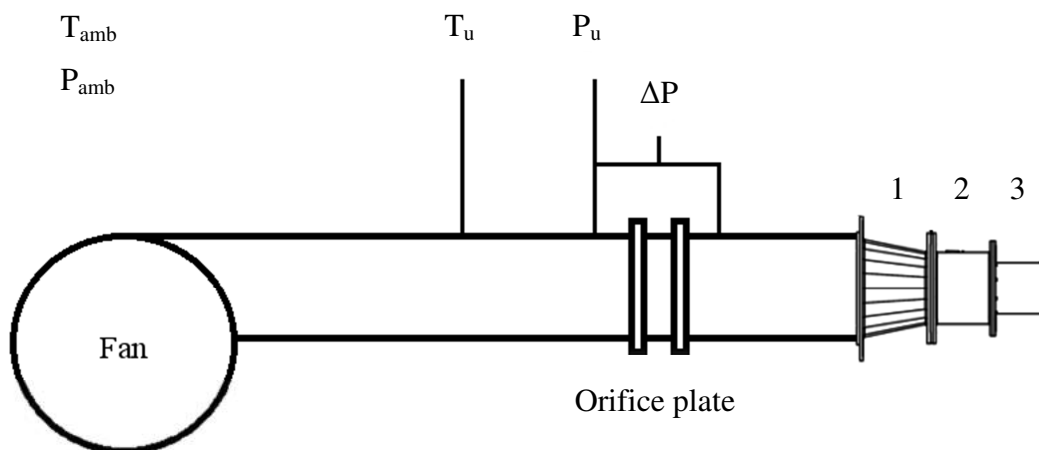


Figure 10: Schematic diagram of the combustion test rig.

Figure 10 shows a schematic diagram of the combustion test rig at Stellenbosch University. The numbers 1, 2 and 3 refer to the adapter nozzle, the combustor housing and the exhaust respectively. The test rig consists of a fan followed by an orifice plate, followed by the test section, consisting of the adapter nozzle, the combustor housing and the exhaust.

The mass flow through the combustion chamber with all of the sets of holes open is referred to from this point forward as the primary case.

The following cases involve measuring the mass flow through one set of holes at a time, by taping each of the other sets of holes shut. This measurement is done while keeping the pressure drop over the system constant. Thus the mass flow measured for the hole set under consideration is the percentage of total mass flow.

3.1. Experimental Procedure

The experimental procedure entails the measurement of the pressure and temperature upstream and downstream of the orifice plate, as shown in Figure 10. Before the experimental procedure was commenced, leakages in the system were minimised in order to ensure accurate measurements. The leakage investigation is shown in Appendix F. The following variables, shown in Table 3, were measured.

Table 3: Variables that were measured during the flow distribution procedure.

Variable	Symbol
Ambient Pressure	P_{amb}
Ambient Temperature	T_{amb}
Upstream Orifice Plate Pressure	P_u
Upstream Orifice Plate Temperature	T_u
Pressure Difference Across The Orifice Plate	ΔP

As mentioned earlier, the pressure drop over the combustion chamber, for the primary case was determined first at various mass flow rates.

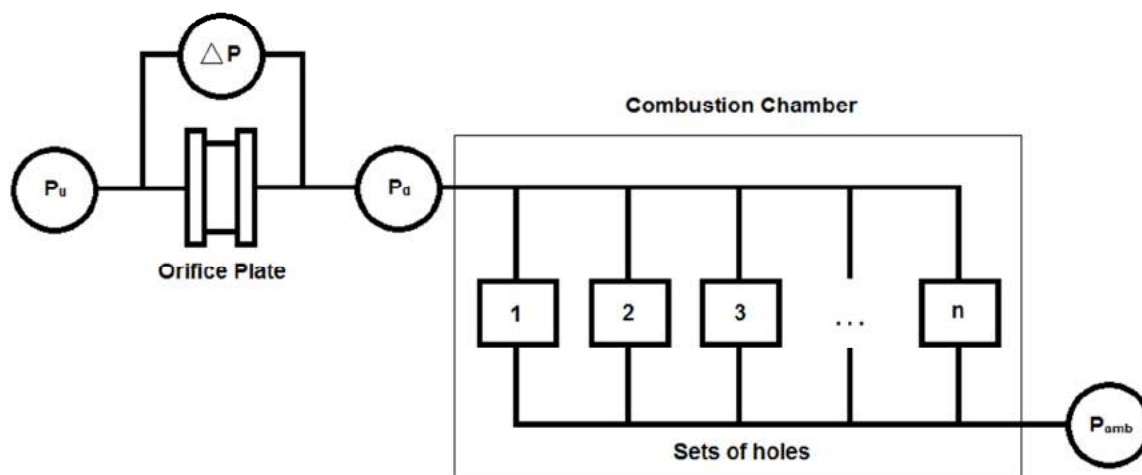


Figure 11: Diagrammatic representation of the mass flow distribution through the combustion chamber.

Figure 11 shows a diagrammatic representation of the test rig where the various sets of combustor liner holes are numbered from *set 1* to *set n*. The primary case is the case where all the sets of holes (from *set 1* to *set n*), are kept open. The combustor's different sets of holes were numbered as follows in Figure 12 for simplicity.

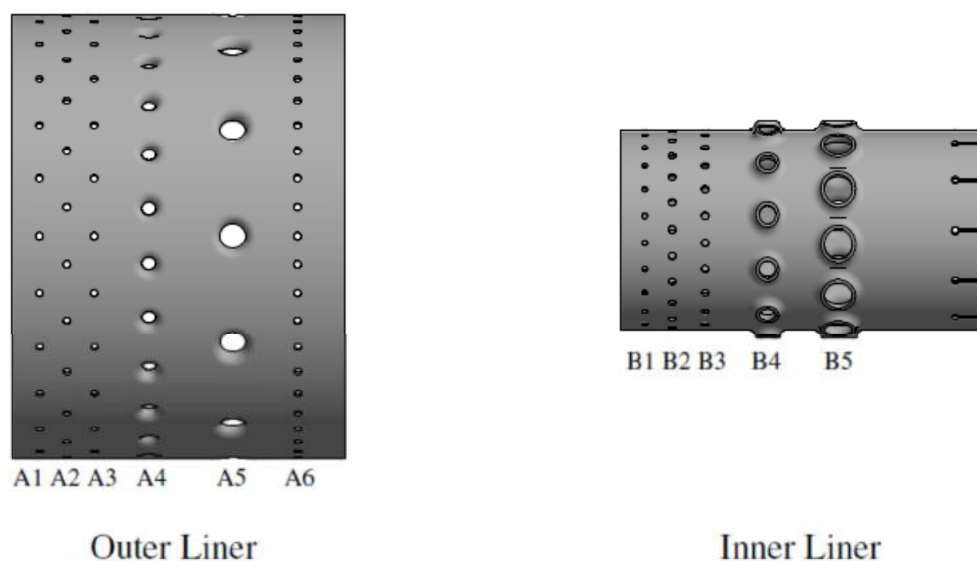


Figure 12: Hole-set designs for combustion chamber.

In the case of the BMT120-KS the pressure loss over the liner cannot be determined analytically or experimentally using the methods developed by Lefebvre and Ballal (2010: 120-122) and Adkins and Gueroui (1986: 491-497). This is due to the fact that the total pressure upstream of the hole, the static pressure downstream of the hole and the discharge coefficient of the hole are unknown and cannot be determined using the available test rig.

In order to determine the mass flow percentage through a certain set of holes with the available test rig, assumptions were made. The assumptions are as follow:

1. There are no frictional losses due to the combustor liner.
2. The flow is incompressible.
3. The pressure drop across the liner is equal in some proportion to the pressure drop over the system (therefore keeping the pressure drop over the entire system constant is equivalent to keeping the pressure drop over the liner constant.)
4. The pressure drop across the liner is constant at any point along the liner.

The next step was to tape all the sets of holes except the set under consideration shut by means of insulation tape. In other words, hole set A4 (the set under consideration) was kept open while hole sets A1, A2, A3, A5, A6, B1, B2, B3, B4, B5 and the vaporizer tubes and cooling holes were taped shut, as can be seen in Figure 13.



Figure 13: Photo of the experimental configuration used to determine the mass flow through hole-set A4.

With the assumptions in mind, the pressure drop over the system was kept as close as possible to the pressure drop measured over the system for the primary case. This was accomplished by keeping the pressure downstream of the orifice plate constant between the primary case and the following cases, as the outlet was open to ambient conditions.

This process was followed for each of the sets of holes. The mass flow percentage through the set of holes under consideration was then calculated using the following equation:

$$\dot{m}_k \% = \frac{\dot{m}_k}{\dot{m}_{tot}} \times 100 \quad (3.1)$$

In Equation 3.1 the mass flow through the combustion chamber for the primary case is represented by \dot{m}_{tot} . The pressure just upstream of the combustion chamber indicated in Figure 11 as P_d , was calculated by the following equation:

$$P_d = P_u - \Delta P \quad (3.2)$$

According to Lefebvre and Ballal (2010: 124) when multiple round jets penetrate a tubular liner, the penetration is much lower than it would be for a single jet, indicating how the flow is effected by a change in geometry. Thus taping certain

sets of holes shut will have an effect on the mass flow percentage through those holes. Therefore, the inverse of the experimental procedure must take place in order to minimise the error caused by this effect. The inverse of the experiment is defined as follows in this document; the set of holes under consideration was taped shut and all the other sets of holes were kept open. Once the mass flow percentages for both the experimental procedure and its inverse were calculated, an accurate mass flow percentage was calculated by determining the average of the two cases.

The pressure transducers used during the procedure were the Endress&Hauser Deltabar M PMD55 (2014c) and the Endress&Hauser Cerabar M PMC51 (2014b) to measure ΔP and P_u respectively. Type K thermocouples were used to measure the upstream and ambient temperatures.

Measurements inherently contain uncertainty. According to the manufacturer, the uncertainty associated with these pressure transducers are as shown in Table 4.

Table 4: Full Scale Uncertainty of the Pressure Transducers.

Pressure Transducer	Uncertainty [%]	Uncertainty [Pa]
Deltabar M PMD55	0.16 %	± 5 Pa
Cerabar M PMC51	0.033 %	± 10 Pa

From Table 4 it can be seen that the uncertainty of Deltabar (Measuring ΔP) is ± 5 Pa. This was verified during calibration using a Betz manometer. Measuring lower pressures contributes to inaccurate results. Inaccuracies were minimised by using a smaller orifice plate when lower mass flow rates were measured.

The smaller orifice plate was designed to operate between $0.001 \text{ kg/s} < \dot{m} < 0.045 \text{ kg/s}$. The minimum value in the range was determined by the minimum flow estimated through the leakages at the lowest pressure drop over the entire system. The maximum was determined by the flow through the combustion chamber. The orifice plate was also designed with the minimum and maximum ranges of the pressure transducers in mind.

The type K thermocouples were calibrated using a platinum resistance thermometer and a FLUKE Metrology Well. Lastly, an Agilent 34970A Data Acquisition Unit was used to capture the data from the pressure transducers and thermocouples. The uncertainty of the orifice plate was determined using ISO (2003: 13-14) and is shown in Appendix E. Further calibration data and details of the apparatus used can also be found in Appendix E.

A test matrix was constructed in order to concisely summarize the experiments and the associated experimental conditions. The test matrix is show in Table 5.

Table 5: Test matrix.

Case	Mass Flow [kg/s]	Inlet Velocity [m/s]	Ambient Pressure [kPa]	Upstream Temperature [°C]	Density [kg/m³]
Axial					
Ax1	0.0285	1.0830	102.2	17.4129	1.2255
Ax2	0.0306	1.1657	102.2	17.4499	1.2254
Ax3	0.0328	1.2492	102.2	17.4832	1.2252
Ax4	0.0350	1.3316	102.2	17.5112	1.2251
Ax5	0.0361	1.4590	102.2	17.5325	1.2250
Ax6	0.0382	1.5441	102.2	17.5644	1.2249
Ax7	0.0403	1.6284	102.2	17.5984	1.2248
AxOp (Conditions for CFD only)	0.2870	11.9	101.325	25	1.1841
Swirling flow case with the R7 inlet guide vane assembly					
R7.1	0.0284	1.0854	101.9	17.8054	1.2239
R7.2	0.0307	1.1718	101.9	17.8411	1.2237
R7.3	0.0328	1.2543	101.9	17.8741	1.2236
R7.4	0.0350	1.3372	101.9	17.8880	1.2235
R7.5	0.0360	1.4651	101.9	17.9131	1.2234
R7.6	0.0381	1.5497	101.9	17.9659	1.2232
R7.7	0.0402	1.6342	101.9	17.9951	1.2231
Swirling flow case with the R9 inlet guide vane assembly					
R9.1	0.0284	1.0833	102.1	18.5285	1.2209
R9.2	0.0305	1.1667	102.1	18.6032	1.2205
R9.3	0.0327	1.2503	102.1	18.6346	1.2204
R9.4	0.0349	1.3330	102.1	18.6627	1.2203
R9.5	0.0359	1.4604	102.1	18.6888	1.2202
R9.6	0.0380	1.5452	102.1	18.7346	1.2200
R9.7	0.0401	1.6295	102.1	18.7664	1.2199

3.2. Calculations

The calculations to determine the mass flow percentage through each set of holes involved fluid mechanics for obstruction flow meters. The method followed for the calculation of the mass flow can be found in ISO (2003: 1-47), unless otherwise stated.

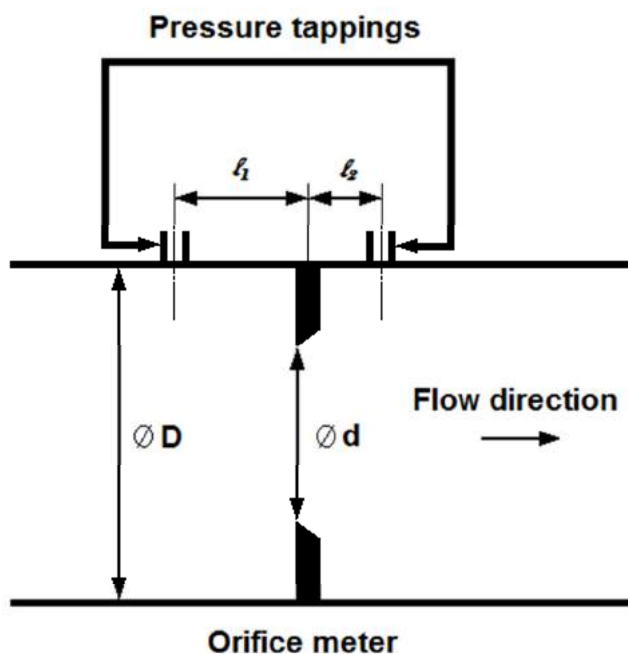


Figure 14: Diagram of the geometry of an orifice meter.

Figure 14 shows a diagram of an orifice plate and its geometry as well as the distances of the pressure tapplings from the orifice plate. The equation for the mass flow rate through an orifice plate is:

$$\dot{m} = A_o C_d E \sqrt{\frac{2\rho(\Delta P)}{(1-\beta^4)}} \quad (3.3)$$

In Equation 3.3, A_o represents the orifice area, C_d represents the discharge coefficient, E is the expansibility factor, ρ represents the density, ΔP is the pressure drop over the orifice plate and β is the diameter ratio.

The discharge coefficient is calculated by the following equation:

$$\begin{aligned}
C_d = & 0.562 + 0.261\beta^8 + 0.000521 \left(\frac{10^6 \beta}{Re_D} \right)^{0.7} + \\
& (0.0188 + 0.0063A)\beta^{3.5} \left(\frac{10^6}{Re_D} \right)^{0.3} + (0.043 + \\
& 0.080e^{-10L_1} - 0.123e^{-7L_1})(1 - 0.11A) \frac{\beta^4}{1-\beta^4} - \\
& 0.031(M'_2 - 0.8M'_2{}^{1.1})\beta^{1.3}
\end{aligned} \tag{3.4}$$

In Equation 3.4 Re_D is the Reynolds number calculated with respect to the diameter of the pipe (D), L_1 is the quotient of the distance of the upstream tapping from the upstream face of the plate and the pipe diameter and L_2' is the quotient of the distance of the downstream tapping from the downstream face of the plate and the pipe diameter.

The unknown variables in Equation 3.4 can be calculated by the following equations:

$$\beta = \frac{d}{D} \tag{3.5}$$

$$L_1 = \frac{l_1}{D} \tag{3.6}$$

$$L_2' = \frac{l_2}{D} \tag{3.7}$$

$$M'_2 = \frac{2L_2'}{1-\beta} \tag{3.8}$$

$$A = \left(\frac{19000\beta}{Re_D} \right)^{0.8} \tag{3.9}$$

The expansibility factor, in Equation 3.3, takes the expansion of the fluid into account and is defined as:

$$E = 1 - (0.351 + 0.256\beta^4 + 0.93\beta^8) \left[1 - \left(\frac{P_u - \Delta P}{P_u} \right)^{1/\kappa} \right] \tag{3.10}$$

In Equation 3.10, κ represents the specific heat ratio of air. The density, as used in Equation 3.4, can be calculated using the ideal gas law:

$$P = \rho RT \quad (3.11)$$

In Equation 3.11, R is the specific gas constant of dry air and P and T represent the upstream pressure and temperature respectively.

The viscosity used in determining the Reynolds number with respect to the pipe diameter is determined according to Kröger (1998: A.1.):

$$\mu_a = 2.287973 \times 10^{-6} + 6.259793 \times 10^{-8}T - 3.131956 \times 10^{-11}T^2 + 8.15038 \times 10^{-15}T^3 \quad (3.12)$$

In Equation 3.12, T represents the upstream temperature in Kelvin. The discharge coefficient is dependent on the Reynolds number with respect to the pipe diameter, which can only be calculated once the mass flow rate is known. Therefore the mass flow is determined iteratively.

4. INLET GUIDE VANE DESIGN AND MANUFACTURE

In the physical micro-gas turbine engine, a component of swirl may exist in the air at the outlet of the compressor. In order to determine whether the component of swirl has an effect on the mass flow distribution of the combustion chamber, it was decided to add a component of swirl to the inlet velocity experimentally and numerically. In order to induce swirl experimentally it was necessary to design and manufacture inlet guide vanes.

4.1. Inlet Guide Vane Design

The inlet guide vane design was driven by the desire to induce swirl in the annulus of the combustion chamber. Since the compressor outlet information was not available at the time that this project was undertaken, the goal was not to replicate engine operating conditions, but to investigate whether swirl in the annulus flow has an effect on the mass flow distribution through the combustion chamber holes. Therefore, two arbitrary degrees of swirl were tested.

4.1.1. Blade design

It was decided to use constant-thickness circular-arc blades. These blades were chosen, due to their simplicity and ease of manufacture. Two different radii were chosen in order to induce two degrees of swirl, while still being able to mount the blades with their leading edge parallel to the axial flow direction (incidence angle of 0°). The radii were chosen, as opposed to choosing an outlet flow angle, as

choosing an outlet flow angle might result in strange radii that are possibly not manufacturable.

The radii were chosen arbitrarily, as the goal of this experiment is to determine whether an element of swirl has any influence on the mass flow distribution of the flow through the combustion chamber and not to replicate engine conditions.

The profile of the constant thickness blades and their varying radii are shown in Figure 15.

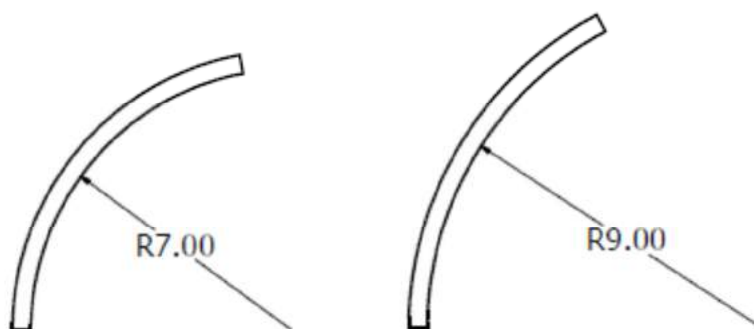


Figure 15: Blade profiles and radii of the inlet guide vanes.

The blades were designed to be manufactured from aluminium sheet metal with a thickness of 0.5 mm. Aluminium was chosen, as the material has a low Young's modulus (only 73 GPa) compared to the other available materials. This characteristic allowed the material to more easily be curved into the desired shape. As well as the consideration that there would be no combustion tests, therefore the material did not have to be heat resistant.

The outlet angles of the flow were determined using the equations in Section 2.3. The calculation for the R7 mm blade follows for clarity.

First the chord length was determined. The blades were curved by pressing a 10 mm by 17 mm rectangular section of aluminium sheet metal into a circular section with the chosen radii. The sections were chosen to be 17 mm by 10 mm, due to the space limitations. Therefore the arc length of the blade would be 10 mm.

In order to determine the chord length of the blade, the angle of the circular section that would be the profile of the blade, was calculated:

$$L = R\xi \quad (4.1)$$

$$0.01 = 0.007 \times \xi$$

$$\xi = 1.4286 \text{ rad}$$

In Equation 4.1, L represents the arc length which is 10 mm and R represents the radius in this section, which is known and ξ represents the angle of the section.

Then from Equation 4.1 the angle of the section of the circle that comprises the blade can be calculated as shown. Once the angle of the section is known, trigonometry can be used to calculate the chord length.

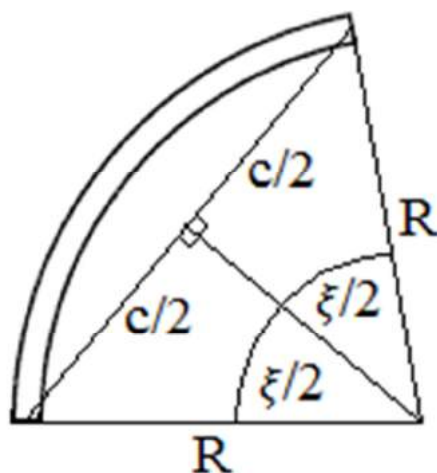


Figure 16: Geometry used to calculate IGV-blade chord lengths.

Figure 16 shows the geometry used to calculate the chord length. The chord length was then calculated using the following equations based on Figure 16.

$$\frac{c}{2} = R \sin \frac{\xi}{2} \quad (4.2)$$

$$\frac{c}{2} = 0.007 \sin \frac{1.4286}{2}$$

$$\frac{c}{2} = 0.00458 \text{ m}$$

$$c = 9.17 \text{ mm}$$

Once the chord length is known, the inlet and outlet angles of the camber line with respect to the axial direction of the flow can be calculated. In order to calculate these angles, the circular arc length was plotted using MATLAB. A line parallel to the angle of the camber line at both the leading and trailing edge of the line was also plotted.

The lines were created by taking the derivative of the equation of the circle as shown below.

$$\frac{dy}{dx} = -x(R^2 - x^2)^{-\frac{1}{2}} \quad (4.3)$$

Once the derivative of the circle was calculated along every point of the section of the circle that comprises the blade, the gradient of the camber line was known along every point of the blade. Therefore the gradient of the lines parallel to the leading and trailing edges were also known. Using the gradients these lines were plotted along with the camber line.

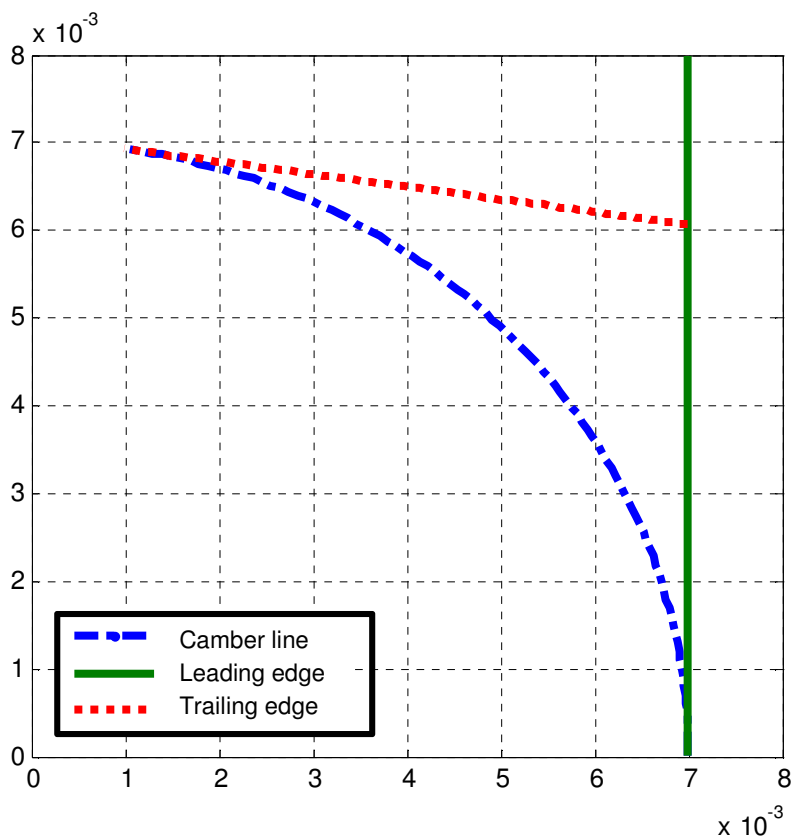


Figure 17: Aerofoil R7 mm camber line.

From Figure 17 the camber line along with the lines parallel to the leading and trailing edges of the blade can be seen.

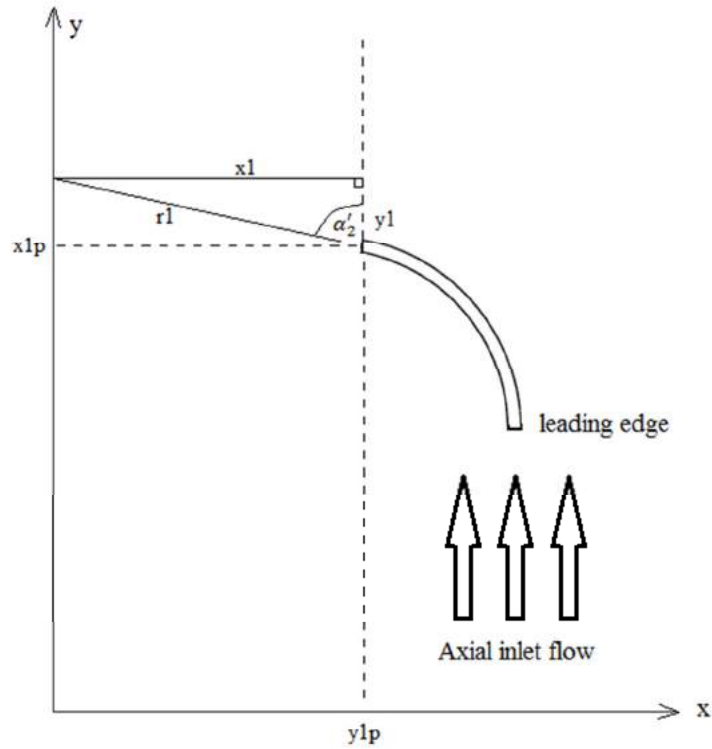


Figure 18: Geometry used to calculate α'_2 .

Figure 18 shows the geometry that was used to calculate α'_2 . Since both lengths x_1 and y_1 were known trigonometry was used to determine angle α'_2 . In the case for the R7 mm blade α'_2 was calculated as follows:

$$c_1 = y_{1p} - \frac{dy}{dx_{1p}} \times x_{1p} \quad (4.4)$$

$$c_1 = 7e^{-9} + (-9.9987e^5 \times 0.007)$$

$$c_1 = 6.9991e^3$$

Equation 4.4 shows how the y intercept for the line parallel to the trailing edge was calculated. Once this was known the length of r_1 was calculated.

$$r_1 = \sqrt{y_{end}^2 + x_{end}^2} \quad (4.5)$$

$$r_1 = \sqrt{8.6026e-004^2 + 0.0060^2}$$

$$r_1 = 0.0061$$

Once the lengths $r1$ and $y1$ are known, α'_2 can be calculated by using the following equation:

$$\alpha'_2 = \cos^{-1} \frac{y1}{r1} \quad (4.6)$$

$$\alpha'_2 = \cos^{-1} \frac{8.6026e-004}{0.0061}$$

$$\alpha'_2 = 1.4286 \text{ rad}$$

The camber line at the inlet is parallel to the flow. Therefore the angle of the leading edge with respect to the axial direction of the flow is 0° , as can be seen from Figure 17 and the angle was only calculated as a means by which to verify the calculation. Once both α'_1 and α'_2 are known the Equations described in Section 2.4 can be used.

$$\theta = 0 - 1.4286 \quad (2.1)$$

$$\theta = -1.4286 \text{ rad}$$

The incidence angle can now be determined.

$$i_a = \alpha_1 - \alpha'_1 \quad (2.2)$$

$$i_a = 0 \text{ rad}$$

It can be seen that the incidence angle is zero, this is due to the fact that all the blades were mounted with their leading edge directly into the axial direction of the flow.

The outlet angle of the flow should now be determined using Equations 2.3-2.5 from Section 2.3. As can be seen, there are too many unknowns and the outlet angle must be solved iteratively.

$$\delta = \alpha_2 - \alpha'_2 \quad (2.3)$$

$$\delta = m\theta \left(\frac{s}{c}\right)^{\frac{1}{2}} \quad (2.4)$$

$$m = 0.23 \left(\frac{2a}{c}\right)^2 + 0.1 \left(\frac{\alpha_2}{50}\right) \quad (2.5)$$

An initial flow outlet angle was guessed.

$$\alpha_2 = 0.05 \text{ rad}$$

Then Equation 2.5 was substituted into Equation 2.4 and Equation 2.4 and 2.3 were set equal to each other yielding Equation 4.7:

$$\alpha_2 - \alpha'_2 = \left(0.23 \left(\frac{2a}{c} \right)^2 + 0.1 \left(\frac{\alpha_2}{50} \right) \right) \theta \left(\frac{s}{c} \right)^{\frac{1}{2}} \quad (4.7)$$

Equation 4.7 was then rewritten to set it equal to zero, in order to use the fsolve function in MATLAB.

$$0 = \left(0.23 \left(\frac{2a}{c} \right)^2 + 0.1 \left(\frac{\alpha_2}{50} \right) \right) \theta \left(\frac{s}{c} \right)^{\frac{1}{2}} - (\alpha_2 - \alpha'_2) \quad (4.8)$$

The flow outlet angle for the R7 mm blade was calculated as 0.8129 rad. The summarized outlet angles are shown below in Table 6 for the various radii and mass flows.

Table 6: Blade outlet flow angles for varying radii.

Radii [mm]	7	9
Flow outlet angle [rad]	0.8129	0.6393
Flow outlet angle [deg]	46.5752	36.6275

4.1.2. Hub and shroud design

The inlet guide vane assemblies were designed to be assembled into the test section, between the adapter nozzle and the combustor housing. It was also designed to hold the diffuser. This was determined to be the optimal placement for the inlet guide vane assemblies, without redesigning the entire test section.

The hub of the inlet guide vane assemblies was therefore designed to fit over the diffuser in the test section and to be flush with the surface of the diffuser, in order not to create any disturbances in the flow as shown in Figure 19.

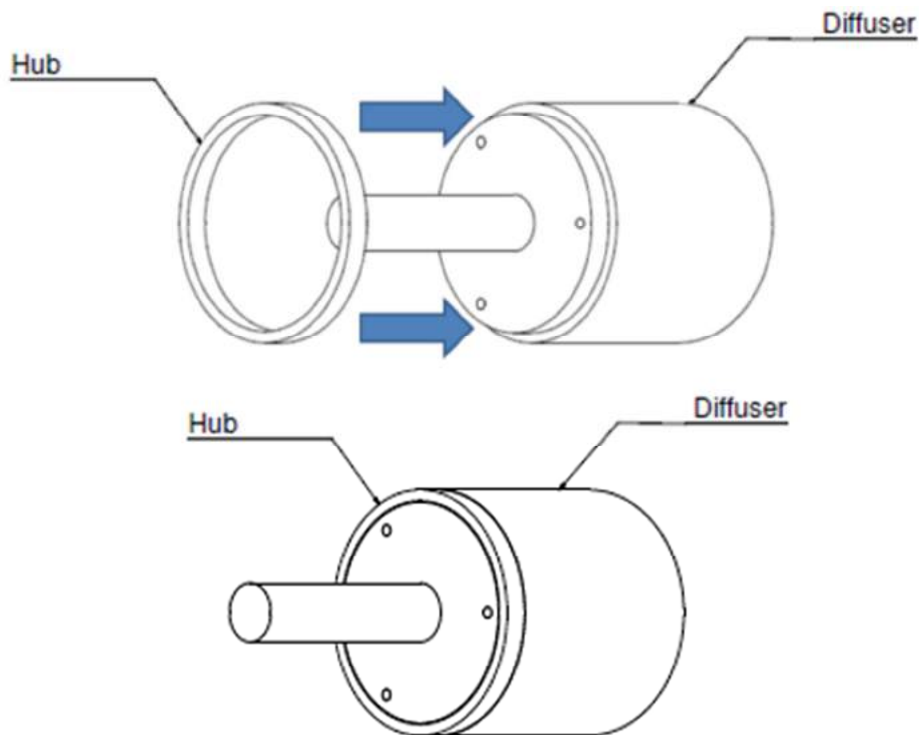


Figure 19: Illustration of the hub relative to the diffuser.

The outer diameter of the diffuser allowed a standard pipe with an outer diameter of 89 mm and a thickness of 4 mm section to be chosen

The shroud was designed to be the means by which the inlet guide vane assembly is assembled into the test section. The inlet guide vane assembly was designed to fit between the adapter nozzle and the combustor housing. These parts are assembled by bolting them together as shown in Figure 20.

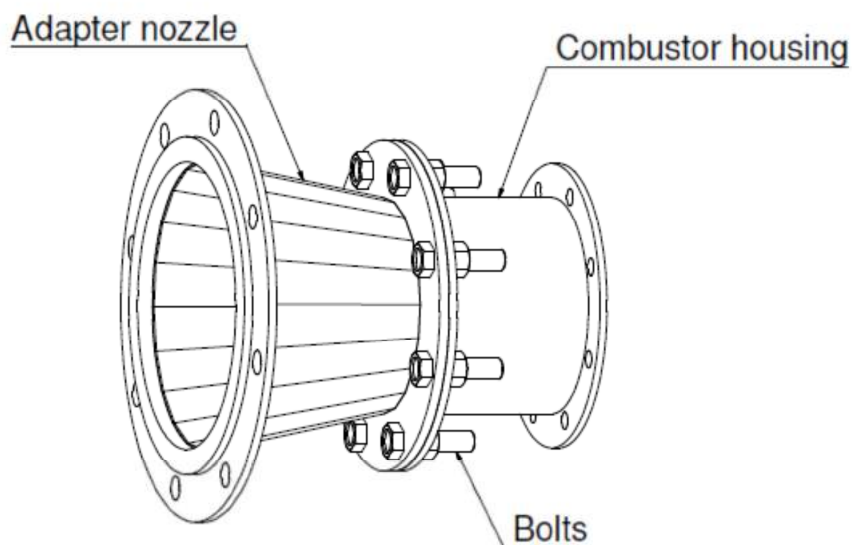


Figure 20: Assembly of the adapter nozzle and the combustor housing.

In order to be able to assemble the inlet guide vane assembly between the adapter nozzle and the combustor housing, the shroud was designed as a flange with holes corresponding to the holes in the flanges of the adapter nozzle and combustor housing.

In order to simplify the assembly, the shroud would be bolted to the combustor housing first using four smaller chamfered holes. The assembly of the inlet guide vane assembly and combustor housing can then easily be bolted onto the adapter nozzle.

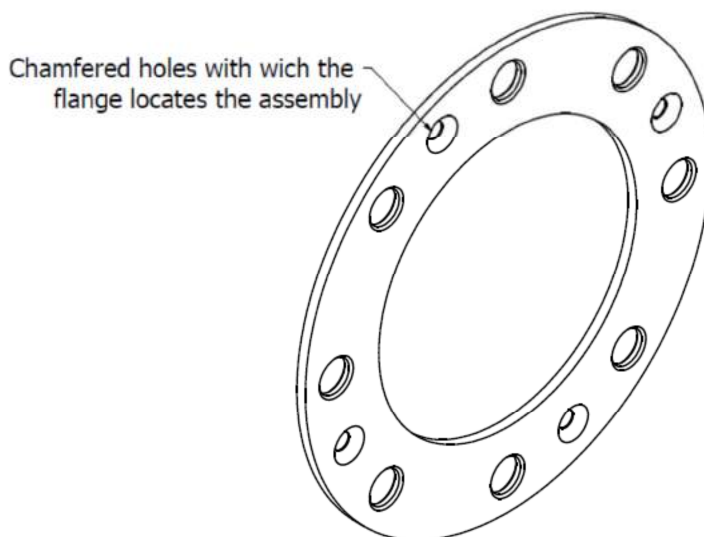


Figure 21: Shroud design

Figure 21 shows the shroud design, with the chamfered holes that will locate the inlet guide vane assembly when it is being mounted onto the test section. The parts were designed to be glued together as shown in Figure 22.

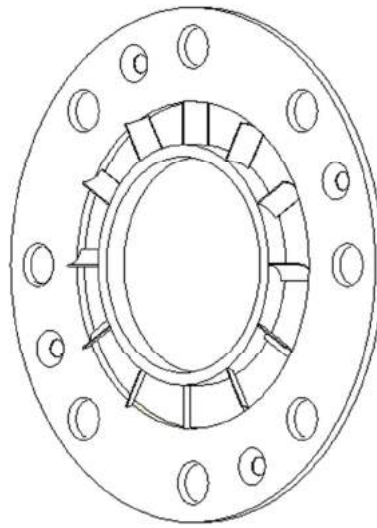


Figure 22: Inlet guide vane assembly.

The inlet guide vane assembly would then be fixed to the diffuser by screwing pins with M4 thread into the diffuser, then placing the inlet guide vane onto the diffuser as shown in Figure 19. A back plate would then be placed over the pins on the back of the diffuser and fastened with nuts as shown in Figure 23.

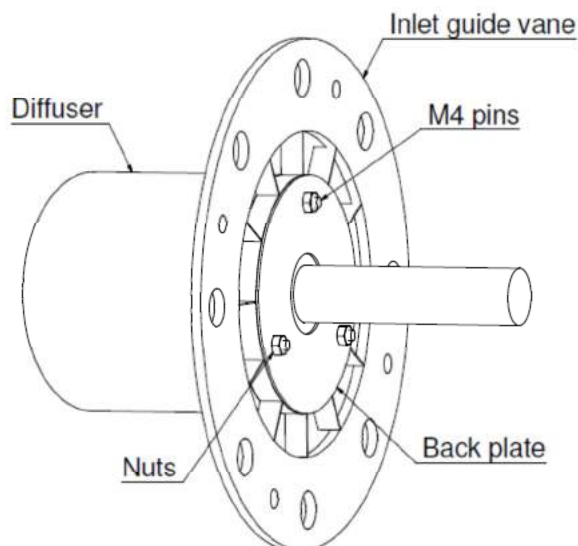


Figure 23: Assembly of the inlet guide vane assembly and the diffuser.

The assembly shown in Figure 23 is then mounted into the test section between the adapter nozzle and combustor housing as shown in Figure 24.

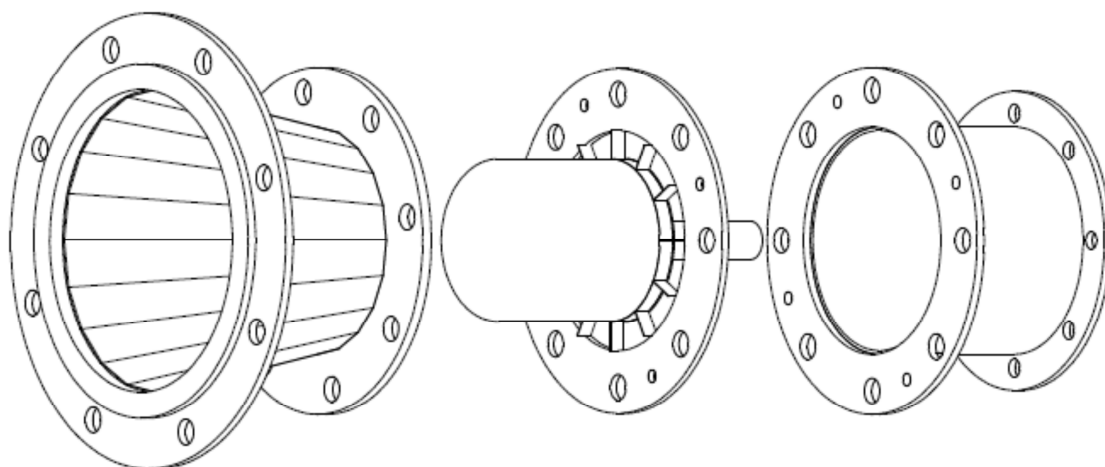


Figure 24: Exploded view of the test section assembly with inlet guide vanes.

The inlet guide vanes in this position will provide swirl in order to efficiently test whether inlet swirl will have any influence on the mass flow distribution.

4.2. Inlet Guide Vane Manufacture

The components of the inlet guide vanes were mostly manufactured and machined in the Central Mechanical Workshop of the Engineering Faculty of Stellenbosch. The technical drawings for all manufactured parts can be found in Appendix A.1.

4.2.1. Blade manufacture

The blades were manufactured from Aluminium due to the material characteristics mentioned in Section 4.1.1.

The shape was obtained by first cutting the sheet metal into 17 mm by 10 mm rectangles and then using a hollow bar with an inner radius 0.5 mm larger than the desired radius for the blade and a solid round bar with an outer radius 0.5 mm smaller than desired. The rectangular sheet was then placed inside the hollow bar and the round solid bar was placed on top. A press was used to press the blades into the desired shape.

4.2.2. Hub and shroud manufacture

The hub was manufactured from a standard aluminium round pipe section and the shroud was laser cut. The finished product is shown in Figure 25.



Figure 25: Manufactured hub and shroud.

4.2.3. Miscellaneous parts

Other parts necessary for the inlet guide vane to fit in the test section include the diffuser, a back plate to keep the inlet guide van assembly on the diffuser and pins to assist keeping the back plate in place.

The back plate was laser cut while the pins were machined and the diffuser was machined as well. Further information and technical drawings can be found in Appendix A.1.

4.2.4. Assembly

The inlet guide vane assembly required that the blades were held at the correct angle while they were being epoxied to the hub. The epoxy used was Pratley Steel®. A dividing head was used to make small marks on the hub to ensure that the blades were mounted at the correct angles as shown in Figure 26.

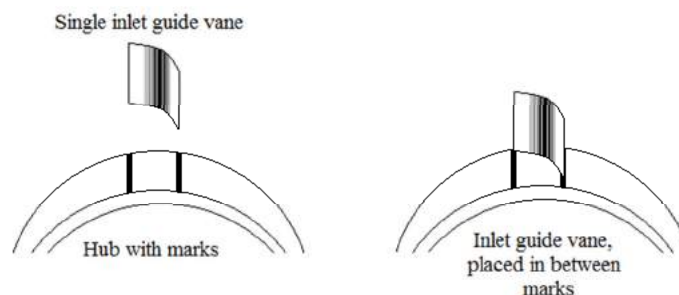


Figure 26: Alignment of inlet guide vanes.

The blades were mounted by securing the hub and shroud concentrically to a steady flat surface and holding the blades in position with Prestik®. The blades were then glued and left to dry for at least 24 hours. Once the blades were securely fastened, excess epoxy was filed away. The inlet guide vane assemblies can be seen Figure 27.

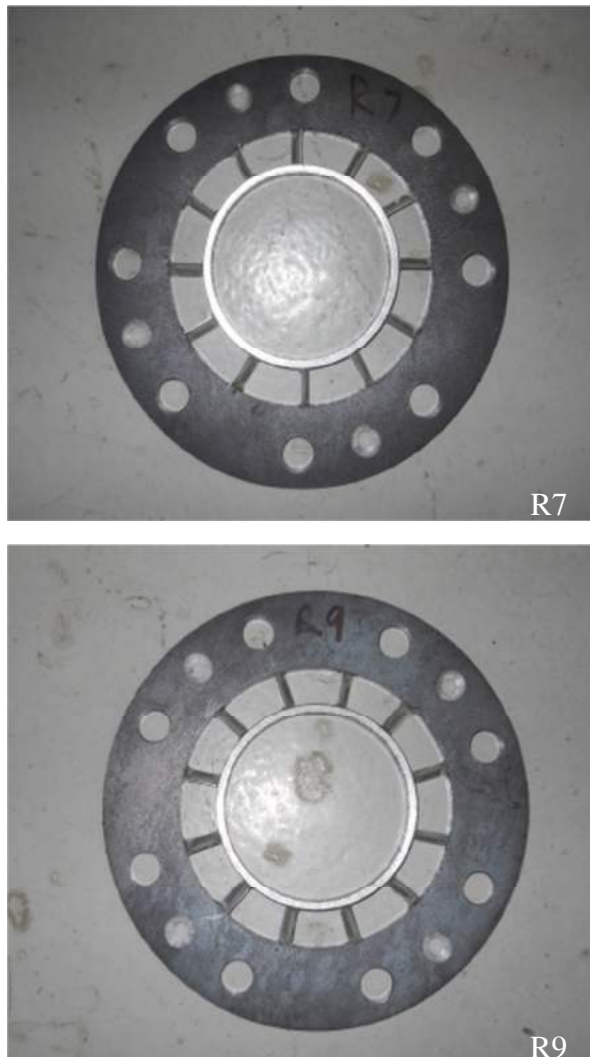


Figure 27: The manufactured R7 and R9 inlet guide vanes.

In order to mount the inlet guide vane assemblies in the test rig, the inlet guide vane assembly was slid onto the diffuser. The back plate was then slid onto the three pins as shown and tightened with M4 nuts as shown in Figure 28.

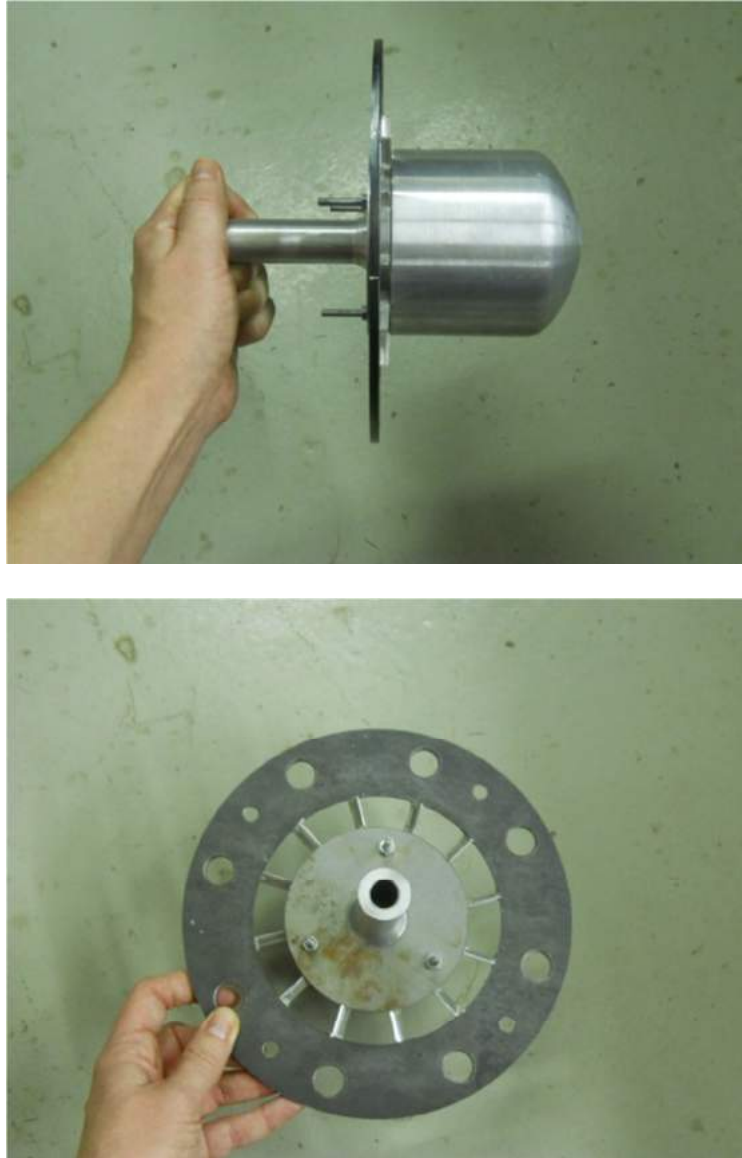


Figure 28: Photo of the inlet guide vane fastened to the diffuser.

The inlet guide vane assemblies were tested to determine what outlet flow angle was delivered in reality. The inlet guide vane assemblies fastened to the diffuser was bolted onto the adapter nozzle and streamers were used to visualise the flow angle. The flow angle was measured at three different speeds. Only one speed is shown, since the flow angle did not change with the increase in speed, as the theory suggests.

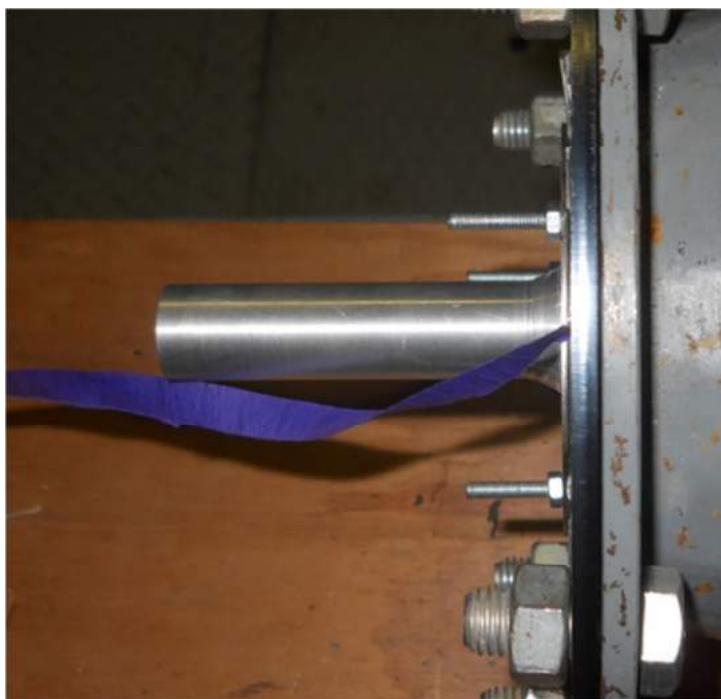


Figure 29: Visualised swirl angle for the R7 swirler.

Figure 29 shows the visualised outlet flow angle for the R7 swirler. The same procedure was followed to determine the outlet flow angle for the R9 swirler.

Table 7: Comparison of the calculated and measured outlet flow angles.

Swirler	Calculated [deg]	Measured [deg]
R7	46.57	20.55
R9	36.62	14.49

Table 7 shows that the measured outlet flow angles are much smaller than the calculated outlet flow angles. This is due to the large outlet camber angles chosen leading to large scale separation. Further research revealed that there were specific equations developed for constant-thickness circular arc blades, but these are only valid for outlet camber angles between 10° and 41° according to Lieblein (1950: 7). It was decided that the discrepancy was acceptable, because two distinct outlet flow angles were obtained and would be sufficient for determining the influence of inlet swirl on the mass flow distribution and flow structures.

5. FLOW SIMULATION

The goal of this project is to determine whether inlet swirl has an impact on the mass flow distribution and flow structures within the BMT120-KS micro-gas turbine engine combustion chamber.

Since the test rig at Stellenbosch University does not replicate the engine or the engine operating conditions, this project entails modelling the test rig in order to compare experimental and numerical results. The model should easily be modified afterwards if the engine is to be modelled.

The flow through the micro-gas turbine engine combustion chamber is complex containing high shear stresses in the form of jets, recirculation and separation as well as boundary layers forming on the walls of the casing, inside the vaporizer tubes, and on the inner- and outer liners between sets of holes. One of the goals of this project is to successfully simulate those flow phenomena in order to predict the mass flow distribution through the holes. This project does not investigate combustion in the combustion chamber.

All the case files for one of the axial and swirling simulations can be found in Appendix B. Only one case is presented, since the other cases are mostly the same and differ only in inlet velocity, outlet pressure and kinematic viscosity.

Computational fluid dynamics is based upon solving the governing equations of an incompressible Newtonian fluid in this case. These equations are the continuity equation and the momentum equations (x, y and z) according to Versteeg and Malalasekera (2007: 24). These equations are shown below.

$$\text{div}(\mathbf{U}) = 0 \quad (5.1)$$

$$\frac{\partial(u)}{\partial t} + \text{div}(u\mathbf{U}) = -\frac{\partial p}{\partial x} \frac{1}{\rho} + \text{div}(v \text{ grad } u) + S_{M_x} \quad (5.2)$$

$$\frac{\partial(v)}{\partial t} + \text{div}(v\mathbf{U}) = -\frac{\partial p}{\partial y} \frac{1}{\rho} + \text{div}(v \text{ grad } v) + S_{M_y} \quad (5.3)$$

$$\frac{\partial(w)}{\partial t} + \text{div}(w\mathbf{U}) = -\frac{\partial p}{\partial z} \frac{1}{\rho} + \text{div}(v \text{ grad } w) + S_{M_z} \quad (5.4)$$

When the flow is turbulent, additional equations need to be solved depending on the turbulence model chosen. The Realizable k- ϵ turbulence model was chosen due to the findings of Gonzalez Toro et al. (2008: 407-422) and Gieras and Stankowski (2012: 68-79), and considering the presentation by Karthik (2011: 45). Their findings led to the conclusion that the Realizable k- ϵ turbulence model would be suited to this problem, since it is superior at modelling swirling and separating flow and can resolve round jets.

The Realizable k- ε turbulence model is based on the standard k- ε model. It differs in the model dissipation rate equation and in the eddy viscosity formulation. New formulations were desired, because it was found that the standard k- ε model was lacking when modelling flows with a high mean shear rate or substantial separation. It was found that the Realizable k- ε model performs well with rotating homogeneous shear flows, boundary-free shear flows including a mixing layer, planar and round jets and backward facing step separated flows. (Shih et al., 1995: 227-238)

The formulations for all the equations that describe the Realizable k- ε model are shown below. All equations are as published by Shih et al. (1995: 227-238). The turbulent kinetic energy equation is the same as for the standard k- ε model:

$$\frac{\partial k}{\partial t} + \text{div} (k\mathbf{U}) = \text{div} \left[\frac{\nu_t}{\sigma_k} \text{grad} k \right] + P_k - \varepsilon \quad (5.5)$$

The modified eddy dissipation rate formulation is shown below:

$$\frac{\partial \varepsilon}{\partial t} + \text{div} (\varepsilon\mathbf{U}) = \text{div} \left[\frac{\nu_t}{\sigma_\varepsilon} \text{grad} \varepsilon \right] + C_1 S \varepsilon - C_2 \frac{\varepsilon^2}{k + \sqrt{\nu \varepsilon}} \quad (5.6)$$

The turbulent viscosity is determined by:

$$\mu_t = \rho C_\mu \frac{k^2}{\varepsilon} \quad (5.7)$$

The equations necessary to calculate μ_t are summarized in Table 8. The constants seen in Equation 5.6 are summarized in Table 9.

Table 8: Equations necessary for the calculation of μ_t .

Constant	Formulation
C_1	$\max \left[0.43, \frac{\eta}{\eta+5} \right]$
η	$S \frac{k}{\varepsilon}$
S	$\sqrt{2S_{ij}S_{ij}}$
C_μ	$\frac{1}{A_0 + A_s \frac{kU^*}{\varepsilon}}$
U^*	$\sqrt{S_{ij}S_{ij} + \tilde{\Omega}_{ij}\tilde{\Omega}_{ij}}$
$\tilde{\Omega}_{ij}$	$\Omega_{ij} - 2\varepsilon_{ijk}\omega_k$
Ω_{ij}	$\overline{\Omega_{ij}} - \varepsilon_{ijk}\omega_k$
A_0	4.04
A_s	$\sqrt{6} \cos \phi$
ϕ	$\frac{1}{3} \arccos \sqrt{6} W$
W	$\frac{S_{ij}S_{jk}S_{ki}}{\tilde{S}^3}$
\tilde{S}	$\sqrt{S_{ij}S_{ij}}$
S_{ij}	$\frac{1}{2} \left(\frac{\partial u_j}{\partial x_i} + \frac{\partial u_i}{\partial x_j} \right)$

Table 9: Constants for modified eddy dissipation rate equation.

Constant	Value
$C_{1\varepsilon}$	1.44
C_2	1.9
σ_k	1.0
σ_ε	1.2

These equations describe the Realizable k- ε model and are applied exactly as proposed by Shih et al. (1995: 227-238) in openFOAM, excluding source terms as seen on cfd-online (2014a).

OpenFOAM version 2.3.0 was used and the simulations were run on a Dell Precision T5610 desk top computer with Intel® Xeon® CPU E5-2687W v2 3.40GHz x 17 processor.

5.1. Material Properties

The fluid used in this simulation is air and the assigned properties were those measured during the experiments and shown in Table 5. All walls were modelled as smooth surfaces, since in reality the metal surfaces would have a negligible surface roughness.

The fluid is incompressible, due to low velocities. The fluid property used in openFOAM is the kinematic viscosity which is a function of the density and the dynamic viscosity. Density is a function of temperature and pressure, and the dynamic viscosity is a function of temperature. Therefore, the kinematic viscosity represents the relationship between the temperature and pressure.

During the experiments, the ambient temperature and pressure would change slightly while measuring the mass flow through the different sets of holes. This was unavoidable, because the experiments are time consuming. However a sensitivity study was done to demonstrate that the ambient change in pressure could not cause more than 1.4 % error, while the change in temperature could not be responsible for more than 2.4 % error. It was therefore concluded that averaging the ambient pressure and temperature for each simulation would not have a large impact on the results. The fluid properties were set in the transportProperties file. The fluid property used for the numerical simulation is kinematic viscosity. The density and temperature shown in Table 5 were used to calculate the kinematic viscosity for each simulation and are shown in Table 10.

Table 10: Fluid properties.

Simulation	Kinematic viscosity [m²/s]
Axial	
Axial speed 1	1.390e-05
Axial speed 2	1.392e-05
Axial speed 3	1.394e-05
Axial speed 4	1.396e-05
Axial speed 5	1.489e-05
Axial speed 6	1.492e-05
Axial speed 7	1.496e-05
Axial engine operating conditions	1.390e-05
Swirling flow case with the R7 inlet guide vane assembly	
R7 IGV speed 1	1.393e-05
R7 IGV speed 2	1.394e-05
R7 IGV speed 3	1.397e-05
R7 IGV speed 4	1.398e-05
R7 IGV speed 5	1.491e-05
R7 IGV speed 6	1.494e-05
R7 IGV speed 7	1.498e-05
Swirling flow case with the R9 inlet guide vane assembly	
R9 IGV speed 1	1.390e-05
R9 IGV speed 2	1.391e-05
R9 IGV speed 3	1.393e-05
R9 IGV speed 4	1.394e-05
R9 IGV speed 5	1.486e-05
R9 IGV speed 6	1.489e-05
R9 IGV speed 7	1.494e-05

5.2. Computational Domain

The computational domain consists of the test section component of the test rig. It includes the adapter nozzle, the inlet guide vane assembly and diffuser, the

combustor housing, the combustion chamber and the exhaust section. The technical drawings of the computational domain can be seen in Appendix A.2. The geometry used in this simulation is three-dimensional, as complex fluid flow occurs in all three dimensions, due to high shear stresses in the form of jets, recirculation and separation as well as boundary layers forming on the walls of the casing, inside the vaporizer tubes, and on the inner- and outer liners between the sets of holes.

A symmetry plane can be identified in the computational domain, therefore only half of the domain was modelled with a symmetry boundary condition in order to save computational time. For the swirling flow simulation, this boundary condition was changed to a cyclic boundary condition to compensate for the circulation of the fluid. The various parts of the computational domain were created in Autodesk Inventor. Shown in Figure 30 is the CAD model of the combustion chamber and components within the test rig inside the computational domain.

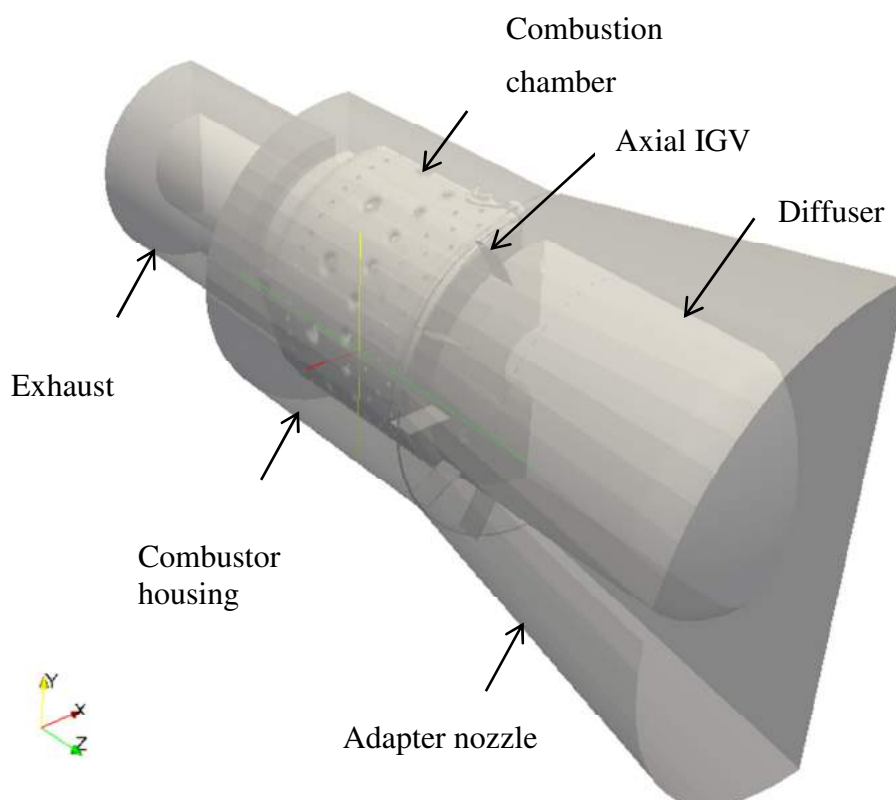


Figure 30: Computational domain for the axial case.

The geometry was modified for the swirling simulations, by adding the inlet guide vane assemblies to the test section. There are two inlet guide vane assemblies as shown in Figure 31 and 32.

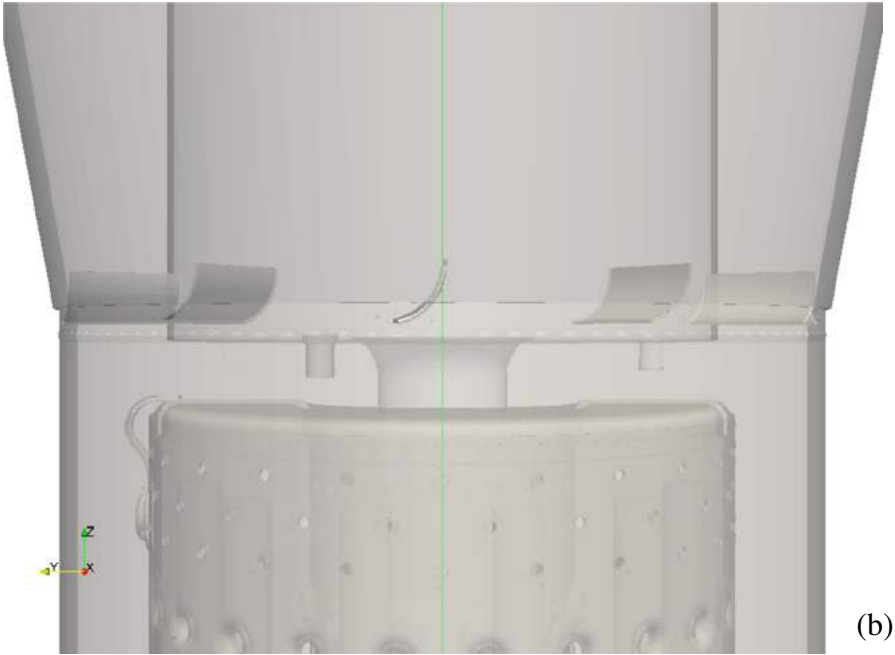
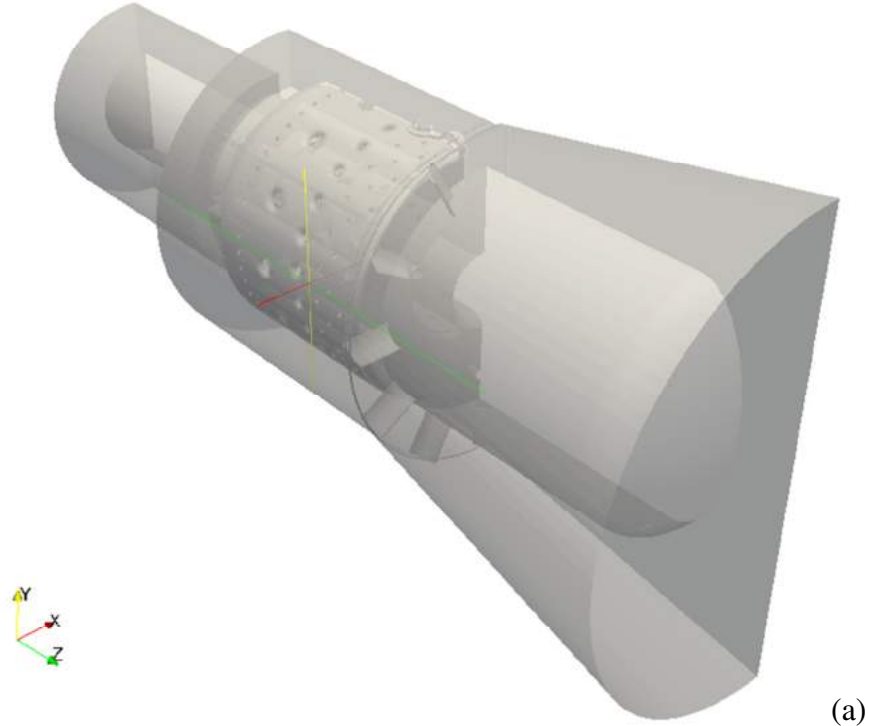


Figure 31: Computational domains of (a) R7 IGW and a close up view of the R7 IGW (b).

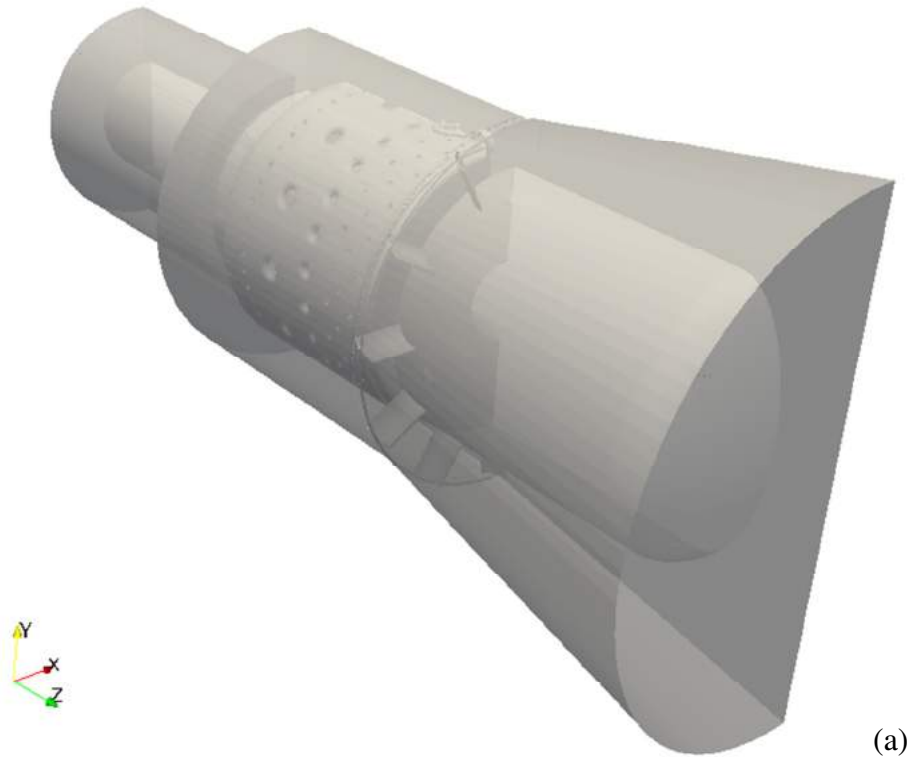


Figure 32: Computational domains of (a) R9 IGV and a close up view of the R9 IGV (b).

5.3. Boundary Conditions

The boundary conditions used for the setup of the simulation were also the conditions encountered during the experiment. The boundary conditions were mostly kept the same for the axial and swirling flow cases, but have a few key differences as discussed below.

5.3.1. Axial flow simulation

For the axial flow simulation, the inlet, outlet, symmetry plane and all the walls were assigned boundary conditions as shown in Figure 33.

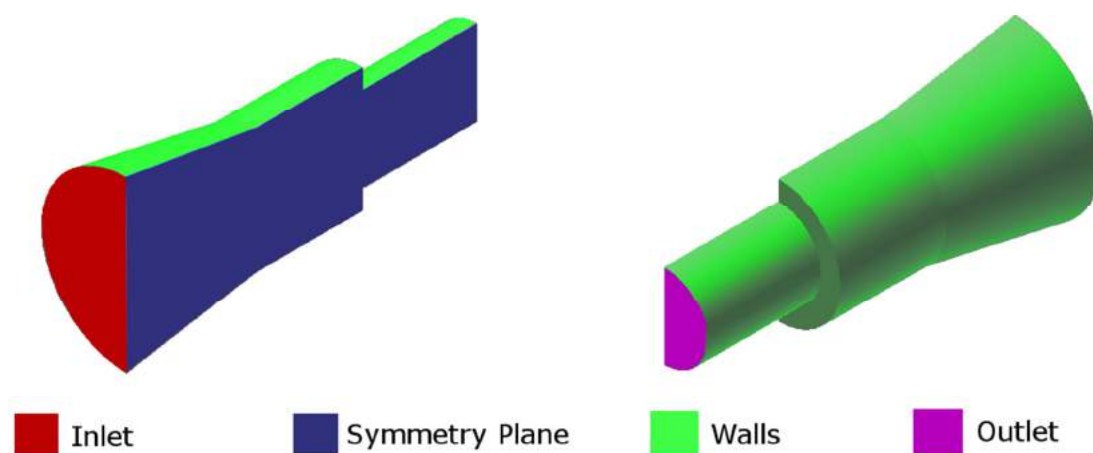


Figure 33: Graphical representation of the boundary conditions for the axial flow case.

The inlet boundary condition consisted of the inlet velocity and the outlet boundary condition consisted of a pressure outlet as the velocity was not known at the outlet. All the walls were assigned a no-slip boundary condition. This included the combustor, the inlet guide vanes and all other internal structures shown in Appendix A.2.

For both the axial and swirling inlet flows an axial velocity was assigned at the inlet. The boundary conditions are shown in Table 11.

Table 11: Boundary conditions for the axial flow case.

Property		Inlet	Outlet	Walls	Symmetry Plane
Turbulent kinetic energy (k)	Type	turbulentIntensityKineticEnergyInlet (intensity = 0.05)	inletOutlet	kqRWallFunction	symmetryPlane
	Value	15.198×10^{-6}	15.198×10^{-6}	0	-
Turbulent dissipation rate (ϵ)	Type	turbulentMixingLengthDissipationRateInlet (mixingLength = 0.00575 m)	inletOutlet	epsilonWallFunction	symmetryPlane
	Value	26.663×10^{-6}	26.663×10^{-6}	26.663×10^{-6}	-
Turbulent dynamic viscosity (ν_t)	Type	calculated	calculated	nutkWallFunction	symmetryPlane
	Value	0	0	0.7797×10^{-6}	-
Pressure(P)	Type	zeroGradient	fixedValue	zeroGradient	symmetryPlane
	Value	-	Variable*	-	-
Velocity(U)	Type	fixedValue	zeroGradient	fixedValue	symmetryPlane
	Value	Variable*	-	0	-

*Variable indicates that the value of this boundary condition is modified for each simulation and is shown in Table 5.

The inlet velocity and outlet pressure for each of the simulations was modified to reflect the conditions experienced during the experiments and summarized in the test matrix in Table 5. The Boundary conditions for the inlet velocity and outlet pressure used in the simulations are summarized in Table 12.

Table 12: Summary of the inlet velocities and outlet pressures for all axial flow simulations.

Simulation	Inlet Velocity [m/s]	Outlet Pressure [Pa]
Ax1	1.0830	102.2
Ax2	1.1657	102.2
Ax3	1.2492	102.2
Ax4	1.3316	102.2
Ax5	1.4590	102.2
Ax6	1.5441	102.2
Ax7	1.6284	102.2
AxOp	11.8952	101.325

5.3.2. Swirling flow simulation

For the swirling flow simulation the patches were defined as shown in Figure 34.

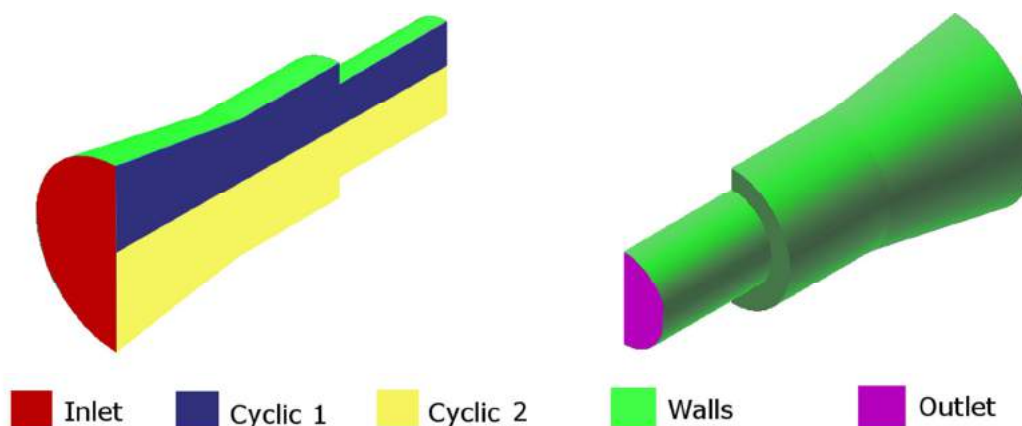


Figure 34: Graphical representation of the boundary conditions for the swirling flow case.

From Figure 34, it can be seen that the symmetry plane was divided into two cyclic patches. All boundary conditions, except the conditions on the symmetry plane were kept the same as for the axial flow simulation except that the symmetry plane boundary condition was replaced with cyclic boundary conditions on the cyclic patches.

The inlet velocity and outlet pressure for each of the simulations was modified to reflect the conditions experienced during the experiments as shown in the test matrix, as shown in Table 5. The Boundary conditions for the inlet velocity and outlet pressure for both of the swirling flow cases are summarized in Table 13.

Table 13: Summary of the inlet velocities and outlet pressures for all swirling flow simulations.

Simulation	Inlet Velocity [m/s]	Outlet Pressure [m^2/s^2]
Swirling flow case with the R7 inlet guide vane assembly		
R7.1	1.0854	101.9
R7.2	1.1718	101.9
R7.3	1.2543	101.9
R7.4	1.3372	101.9
R7.5	1.4651	101.9
R7.6	1.5497	101.9
R7.7	1.6342	101.9
Swirling flow case with the R9 inlet guide vane assembly		
R9.1	1.0833	102.1
R9.2	1.1667	102.1
R9.3	1.2503	102.1
R9.4	1.3330	102.1
R9.5	1.4604	102.1
R9.6	1.5452	102.1
R9.7	1.6295	102.1

5.4. Solvers and Numerical Schemes

The solver used for all simulations was the pisoFoam solver which employed the PISO algorithm. According to Versteeg and Malalasekera (2007: 193) the Pressure Implicit with Splitting of Operators (PISO) algorithm was originally developed for non-iterative computation of unsteady compressible flows. The algorithm can be described by the following flow diagram in Figure 35.

This solver was chosen due to its transient nature and the fact that it delivered the best convergence. A transient solver was necessary, because it was found that small fluctuations of the mass flow rate occurred through the sets of holes that could not be solved with a steady state approximation. The solver settings are set in the fvSolution dictionary and can be found in Appendix B.1.

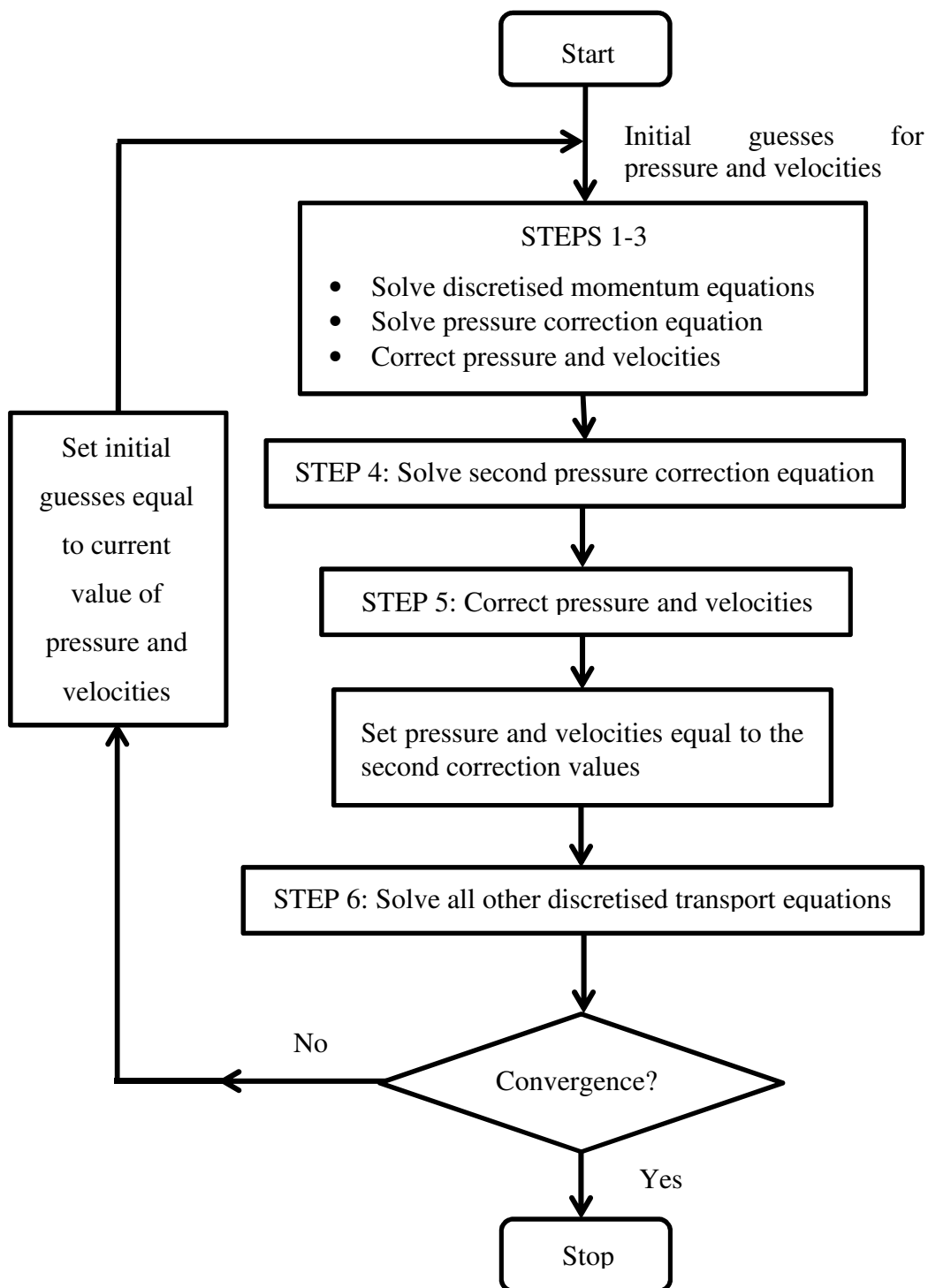


Figure 35: Flow diagram depicting the PISO algorithm.

The linear solver control chosen for the equation of state was the generalized geometric-algebraic multi-grid solver with the relative tolerance set to 0, in order to achieve convergence for each time step. For the momentum equation a preconditioned (bi) conjugate gradient linear solver control with diagonal incomplete-LU preconditioning was used and lastly the linear solver control chosen for the turbulence model equations was solver control using a smoother and the smoother used was Gauss Seidel.

The solution was under-relaxed using relaxation factors of 0.2 for pressure fields, 0.6 for velocity equations and 0.3 for turbulence equations.

Different discretisation schemes were used for the different terms in the governing equations. The numerical schemes for the terms in the governing equations are set in the fvSchemes dictionary according to OpenFOAM (2013: U-113). The following schemes were set in the fvSchemes dictionary as seen in Table 14.

Table 14: fvSchemes dictionary settings.

Sub dictionary	Term	Scheme	Description
ddtSchemes	default	Euler	First order, bounded, implicit
gradSchemes	default	Gauss linear	Second order Gaussian integration
divSchemes	div(phi,U)	Gauss limitedLinearV	Second order, limited linear differencing (Improved for vector fields)
	div(phi,k)	Gauss upwind	First order, bounded
	div(phi,epsilon)	Gauss upwind	First order, bounded
	div(phi,nuTilda)	Gauss upwind	First order, bounded
	div((nuEff*dev(T(grad(U)))))	Gauss linear	Second order, unbounded
laplacianSchemes	default	Gauss linear corrected	Unbounded, second order, conservative
interpolationSchemes	default	linear	Linear interpolation (central differencing)
snGradSchemes	default	corrected	Explicit non-orthogonal correction
fluxRequired	P	-	Only term for which flux is required

The descriptions of all the numerical schemes in Table 14 and of all the available numerical schemes can be found in the openFOAM user guide (OpenFOAM, 2013). The various terms in Table 14 refer to terms in the governing equations and the turbulence model.

5.5. Computational Mesh

The computational meshes were created using only the openFOAM meshing utilities and .stl files generated by Autodesk Inventor. The meshes for the swirling flow simulations only differ slightly from the mesh for the axial flow simulation. This is due to the small change in geometry and the fact that two separate patches

were necessary on the symmetry faces of the swirling flow simulations in order to use the cyclic boundary condition for the swirling flow.

Other meshing tools, such as Salome, were considered, but were not used; due to its inability to create a quality mesh for the geometry. In Salome it is also common practice to divide the geometry into groups of surfaces or faces, in order to create patches later on in openFOAM. Since the geometry of the BMT120-KS has a large number of faces and surfaces, this made the use of Salome impractical and unnecessarily time consuming. SnappyHexMesh was a much superior solution, because a structured background mesh could be created in blockMesh and snappyHexMesh then refined the surfaces of the background mesh around the geometry, leading to a good quality grid. Obtaining the solution was much less time consuming, because snappyHexMesh automatically creates the patches necessary for defining the boundary conditions.

A detailed tutorial on how the mesh was created using blockMesh and snappyHexMesh is presented in Appendix C. This tutorial details all settings and features used.

5.5.1. Axial flow simulation

The computational mesh for the axial flow was created by first generating a structured blockMesh mesh. The blockMesh consisted of the interior volume of the adapter nozzle, the combustor housing and exhaust sections, as shown below in Figure 36.

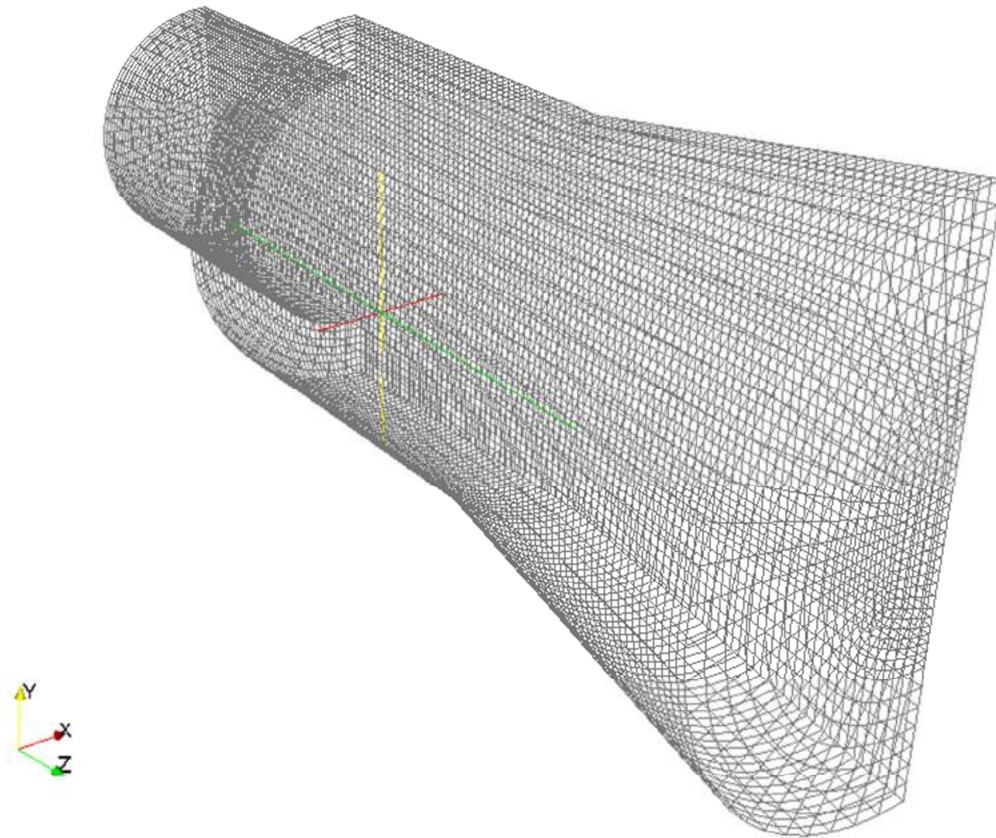


Figure 36: Initial blockMesh mesh for the axial case.

Once the blockMesh was complete, the edgeMesh containing the features of the geometry was extracted from the .stl files using the surfaceFeatureExtract utility. Afterwards snappyHexMesh with refinement levels of (3 3) was used to create the mesh.

The checkMesh utility was used to analyse the mesh quality and the mesh was only accepted if it passed the checkMesh requirements. The checkMesh utility determines various characteristics of the geometry and analyses whether these characteristics are aspects of a good quality mesh as defined in the meshQualityDict file.

The first characteristic analysed is the aspect ratio of the cells. The aspect ratio is the ratio of the longest and shortest cell sides, an aspect ratio of 1 is the optimum. An aspect ratio of 0.01 was defined as the minimum acceptable aspect ratio.

The next important characteristic analysed is the cell volumes. The difference between the cell volumes should be as small as possible (all cells the same size), or if the mesh has larger cells in the free stream and smaller cells closer to objects

in the flow, the transition should be as smooth as possible. The minimum acceptable cell volume was set as $1e-13$.

Furthermore, the mesh's non-orthogonality is analysed. The mesh's orthogonality refers to the angle of the line connecting two cell centres and the normal of their common face, as shown in Figure 37.

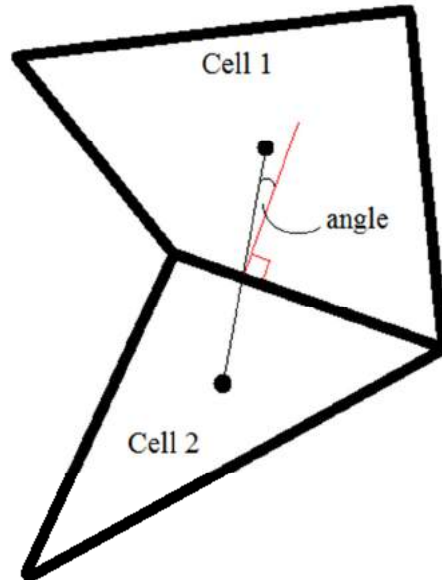


Figure 37: Cell orthogonality.

The maximum acceptable angle for non-orthogonality was set as 65° . The last characteristic analysed is the cell skewness. This refers to the percentage of the distance between the intersection of the cells' common face with the line between their cell centres, to the centre of the cells common face as shown in Figure 38.

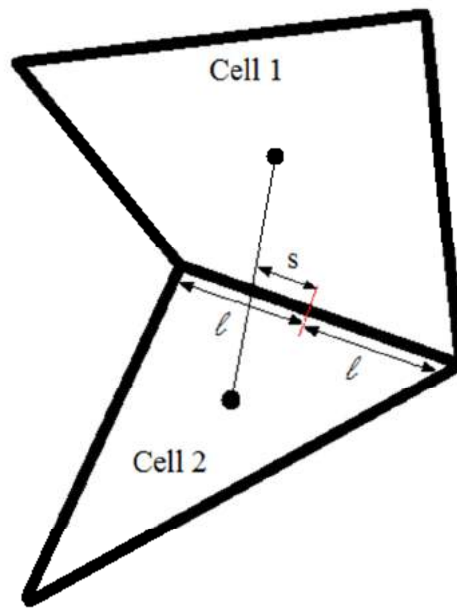


Figure 38: Cell skewness.

In Figure 38 s indicates the percentage of skewness of the cell and l is the distance to the centre of the common face between the cells. The maximum allowable skewness was set to 20 %.

The y^+ values were kept in the range of 30-300 in certain critical areas, in order to ensure that the law of the wall, as described by Kays et al. (2005: 190) and Versteeg and Malalasekera (2007: 59), was obeyed. The areas of interest included the inside of the casing walls, the sections of the outer combustion liner between sets of holes, the sections of the inner combustion liner between sets of holes, the inside of the vaporiser tubes and the turbine shaft. It was decided that only these areas influenced the accuracy of the solution, since boundary layers formed on these surfaces and were near the flow regions of interest. The y^+ values of each of these areas are shown in Figure 39 to 43.

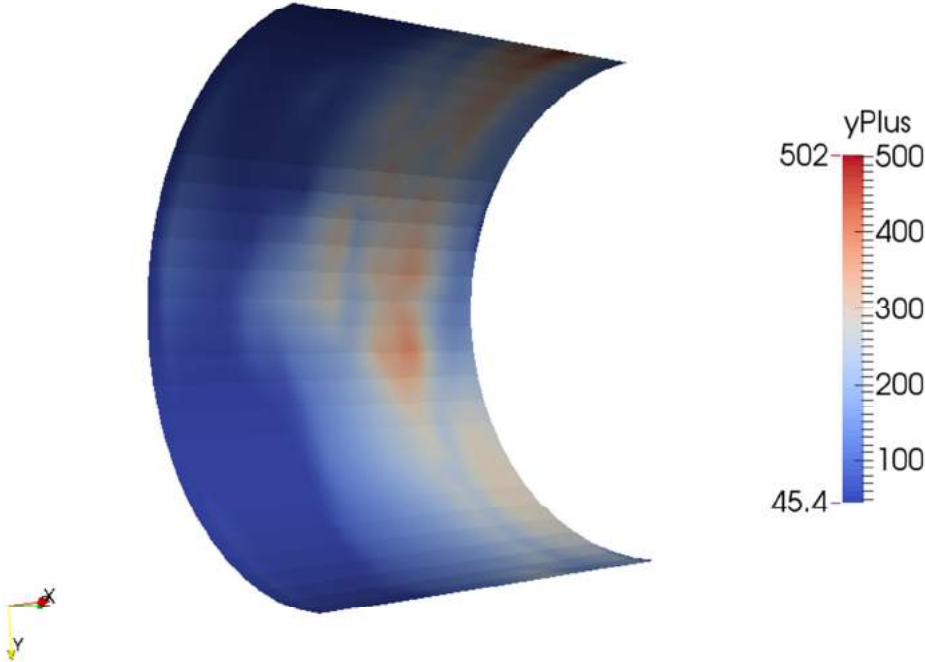


Figure 39: y^+ values on the casing walls

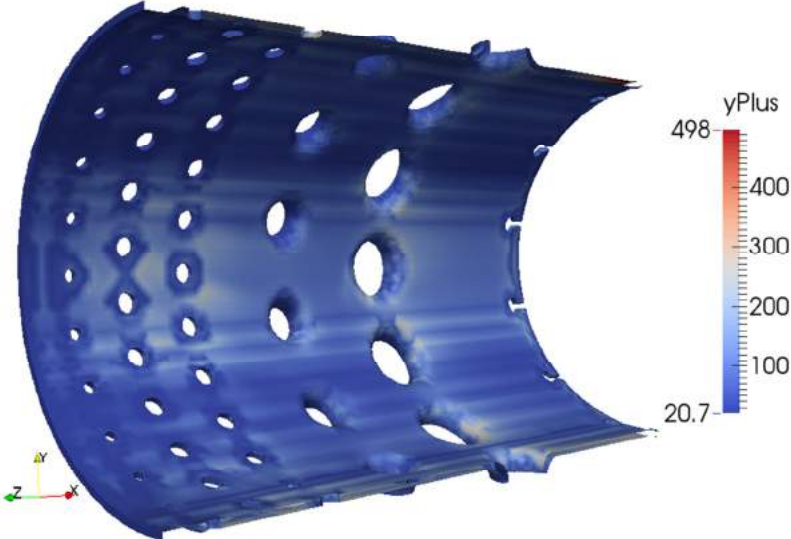


Figure 40: y^+ values on the inner liner.

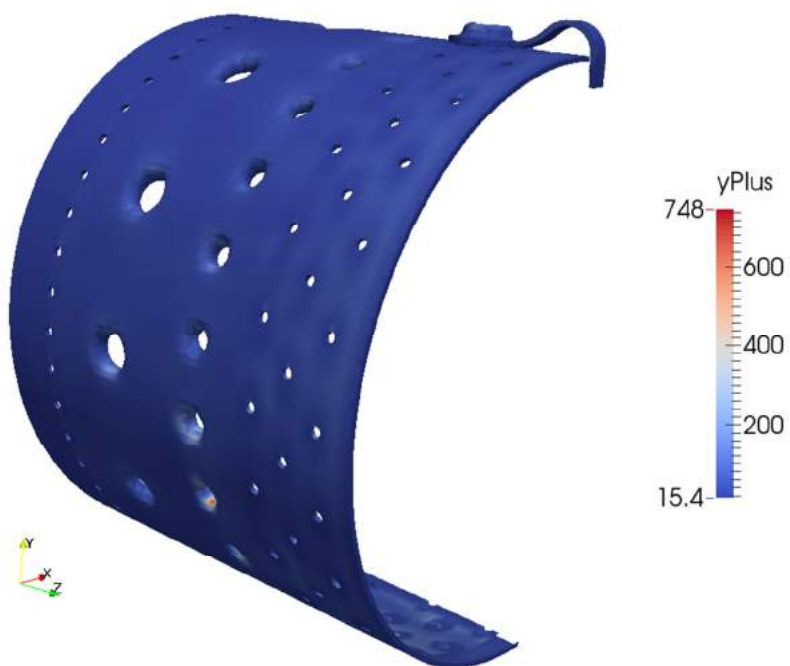


Figure 41: y^+ values on the outer liner.

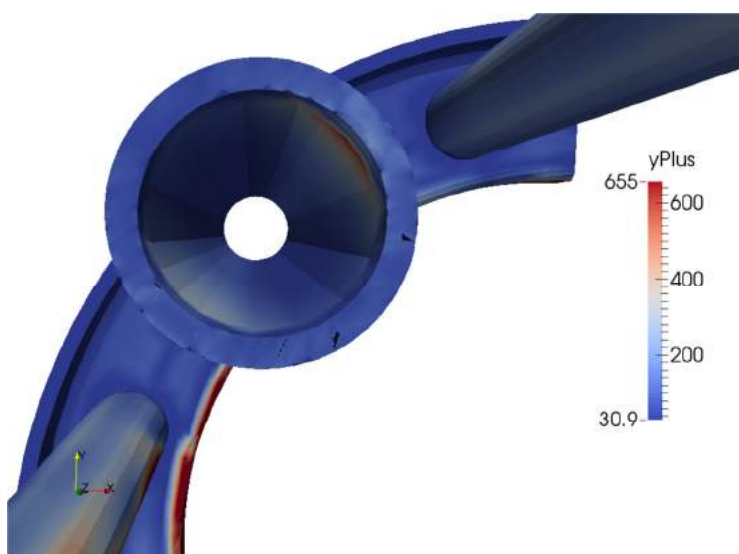


Figure 42: y^+ values on the inside of the vaporizer tubes.



Figure 43: y^+ values turbine shaft.

In Figure 39 to 43 it is important to concentrate on the surfaces shown, as these are the surfaces where boundary layers that influence the flow may form. The y^+ values of interest are summarized in Table 15 for clarity.

Table 15: y^+ values of interest for axial flow.

Area	Minimum y^+ value	Maximum y^+ value	Average y^+ value
Casing Wall	45.359	502.253	195.905
Outer Liner	15.422	748.152	53.628
Inner Liner	20.703	498.332	101.701
Vaporizer Tubes	30.879	655.324	135.027
Shaft	28.098	199.732	72.268

It was then deemed that the mesh had sufficient refinement areas to capture the flow.

Mesh independence was achieved by gradually increasing the number of cells in the mesh and comparing the solutions obtained. The coarseness of the coarsest mesh was limited by snappyHexMesh, if the background blockMesh was too

coarse, the smaller holes in the inner and outer liner would not appear in the final mesh. Therefore only three meshes were compared. A coarse mesh with 1 372 871 cells, a medium mesh with 1 806 104 cells and a fine mesh with 3 511 565 cells. The mass flow through the vaporizer tubes was compared over time as shown in Figure 44.

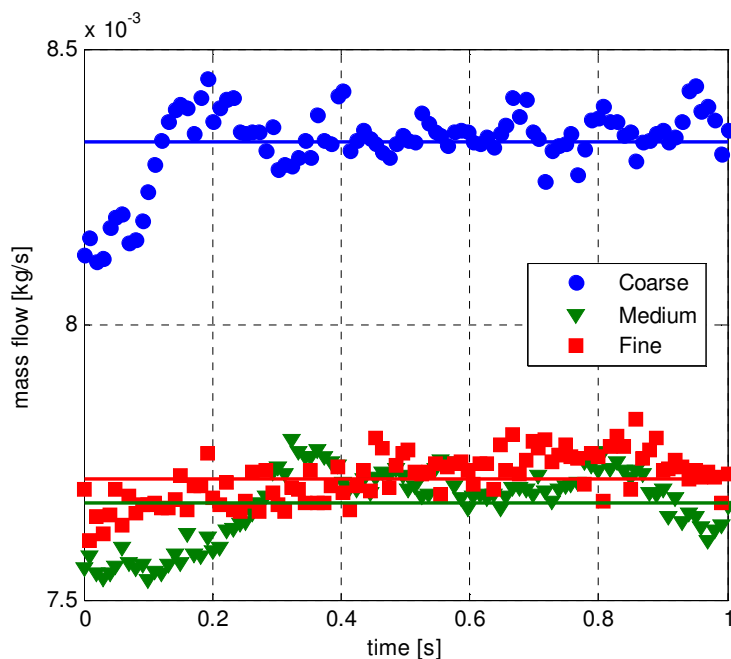


Figure 44: Comparison of mass flow through the vaporizer tubes and cooling holes obtained for a coarse mesh, a medium mesh and a fine mesh.

Figure 44 shows that the medium mesh and the fine mesh delivered similar results, while the coarse mesh over predicted the mass flow through the vaporizer tubes and cooling holes. It was then deemed that the medium mesh delivered sufficient results that were mesh independent. The medium mesh was chosen as the final mesh. The final mesh contained 1 806 104 cells of which 1 225 688 were hexahedral, 68 315 were prisms, 1 628 were tetrahedral wedges and 510 473 were polyhedral.

5.5.2. Swirling flow simulations

The swirling flow computational mesh was created exactly as the axial flow mesh; however the blockMesh file was modified in order to create two separate patches on the symmetry plane. Subsequently, the createPatch utility was used in order to create the cyclic patches on the symmetry plane as shown in Figure 45.

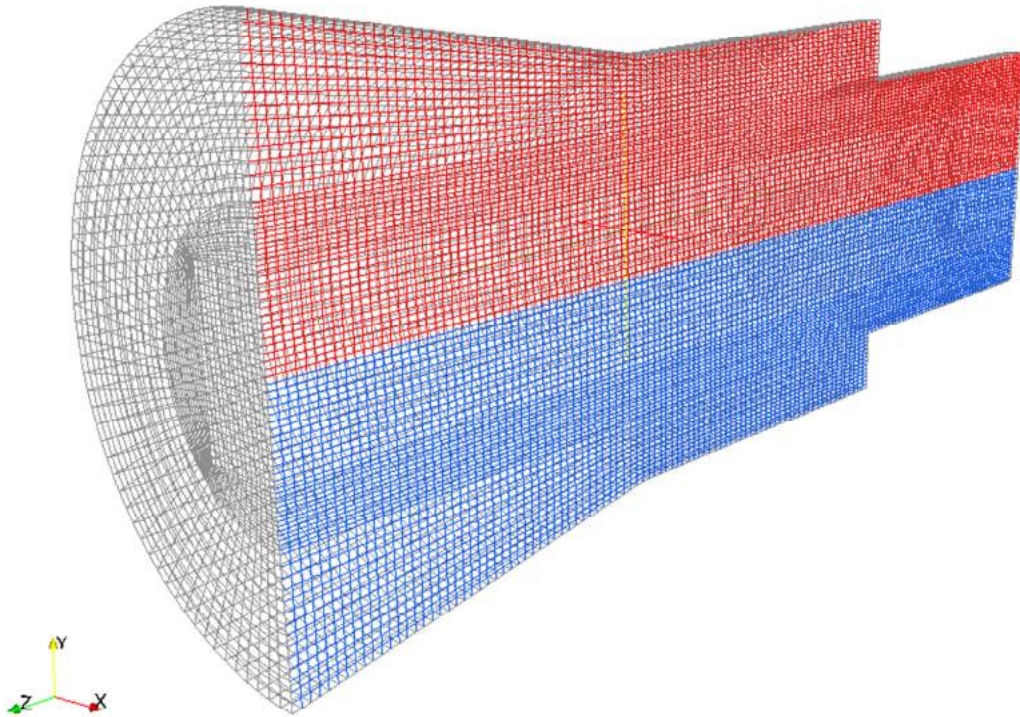


Figure 45: Initial blockMesh mesh for the swirling simulation.

Once the blockMesh was complete, the procedure followed for the axial mesh was repeated. The checkMesh utility was once again used to analyse the mesh quality and the mesh was only accepted if it passed the checkMesh requirements discussed in the previous section.

Mesh independence was not analysed for the swirling flow simulation, since the mesh only differs on the symmetry plane.

The y^+ values of interest are on the same regions as for the axial flow simulation, but include the surface of the inlet guide vane assemblies. Therefore all the y^+ values of interest including the surface of the inlet guide vane blades are summarized in Table 16 for clarity.

Table 16: y^+ values of interest for swirling flow.

Area	Minimum y^+ value	Maximum y^+ value	Average y^+ value
Casing Wall	41.102	489.563	177.294
Outer Liner	17.889	634.133	59.581
Inner Liner	35.003	549.789	112.989
Vaporizer Tubes	29.335	522.031	148.327
Shaft	23.771	163.906	64.708
IGV R7 blades	37.640	471.884	215.299
IGV R9 blades	29.974	449.375	202.573

It was then deemed that the meshes for the swirling flow had sufficient refinement areas to capture the flow. The final mesh contained 1 634 888 cells of which 1 146 220 were hexahedral, 83 735 were prisms, 2 899 were tetrahedral wedges and 402 043 were polyhedral.

6. DISCUSSION AND RESULTS

In order to determine the influence of inlet swirl on the mass flow distribution and internal flow structures of the BMT120-KS micro gas turbine engine, the axial flow through the combustor was considered. This was done to establish a base with which the swirling flow cases could be compared.

The mass flow distribution of the axial case was determined in order to validate the numerical model. The axial experimental results will be discussed first, followed by the comparison of the axial numerical results with the axial experimental results. The axial results, both experimental and numerical will then be compared to the swirling flow cases.

The flow distribution experiment was followed as detailed in Section 3. The upstream pressure was plotted against the calculated mass flow percentage for each set of holes.

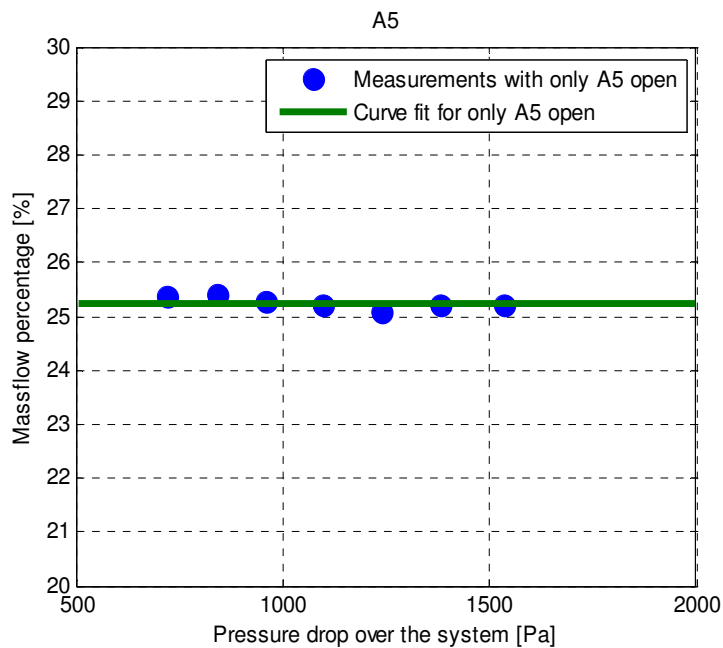


Figure 46: Mass flow percentage for hole-set A5 for forward cases (Ax1-Ax7).

Figure 46 shows the measured data for hole set A5 with the curve fit applied. As can be seen, the measured percentage of mass flow is relatively constant, with minimal scatter.

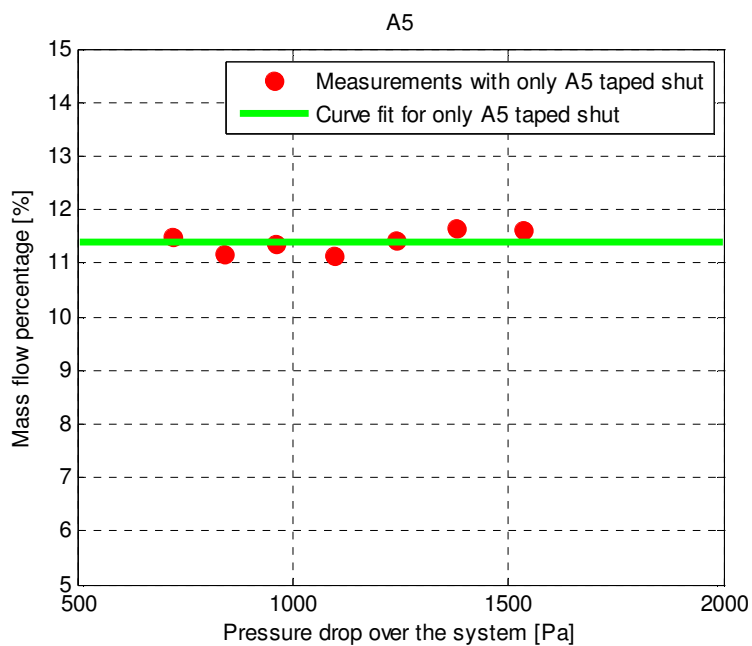


Figure 47: Mass flow percentage for hole-set A5 for inverse cases (Ax1-Ax7).

From Figure 47, it can be seen that the mass flow percentage measured in the inverse experiment is much lower than in Figure 46. Once again it can be seen that there is very little scatter present and the mass flow percentage stays constant. The average was taken between the results shown to determine the actual mass flow percentage through each set of holes. The average calculated for hole-set A5 was 18.02 %.

The average mass flow distribution for all the axial flow cases are shown in Table 17.

Table 17: Axial flow mass flow percentage through each set of holes along with their area percentages.

Hole set	Mass flow %	Area %
A1	2.87	2.84
A2	3.24	2.84
A3	3.00	2.84
A4	13.74	13.57
A5	18.02	16.76
A6	6.73	5.79
B1	1.75	1.60
B2	3.39	4.43
B3	3.69	4.43
B4	6.92	6.79
B5	18.73	19.94
Vaporizer Tubes and Cooling holes	19.44	18.18
Total	101.51	100

From Table 17 it was observed that the total added to 101.51 %, indicating accurate results. It was also noted that the sets of holes open to the outer annulus received more airflow (67.04 %) than the holes open to the inner annulus (34.48 %). Therefore two more tables are presented comparing the mass flow percentages with the area percentages for the two separate flow regions.

Table 18: Comparison of area percentage and mass flow percentage of hole-sets open to outer annulus.

Hole sets	Mass flow %	Area %
A1	4.28	4.52
A2	4.83	4.52
A3	4.47	4.52
A4	20.50	21.61
A5	26.88	26.68
A6	10.04	9.22
Vaporizer Tubes and Cooling holes	29.00	28.94

By comparing the mass flow distribution to the effective area of the hole-sets it can be seen, from Table 18, that the mass flow distribution through the outer liner of the combustion chamber is mainly a function of the hole geometry of the combustor. This is due to the assumptions made during the method implemented to determine the mass flow distribution experimentally.

Table 19: Comparison of area percentage and mass flow percentage of hole-sets open to inner annulus.

Hole sets	Mass flow %	Area %
B1	5.08	4.29
B2	9.83	11.91
B3	10.70	11.91
B4	20.07	18.25
B5	54.32	53.63

Table 19 shows the same trend as previously discussed for Table 18. From Table 17 to 19, it can be calculated that the primary zone receives 37,38 % of the total mass flow. This is much larger than the typical 28 % according to Boyce (2002: 35) indicating that the combustor might not be performing at an optimum.

6.1. Comparison of Numerical Results with Experimental Flow Distribution Results for the Axial Flow Cases.

As previously stated, the flow through the combustion chamber is highly complex consisting of various flow phenomenon including recirculation, flow separation and round jets. Some of the flow phenomena can be seen in the streamline plot for the Ax7 case in Figure 48 **Error! Reference source not found.**

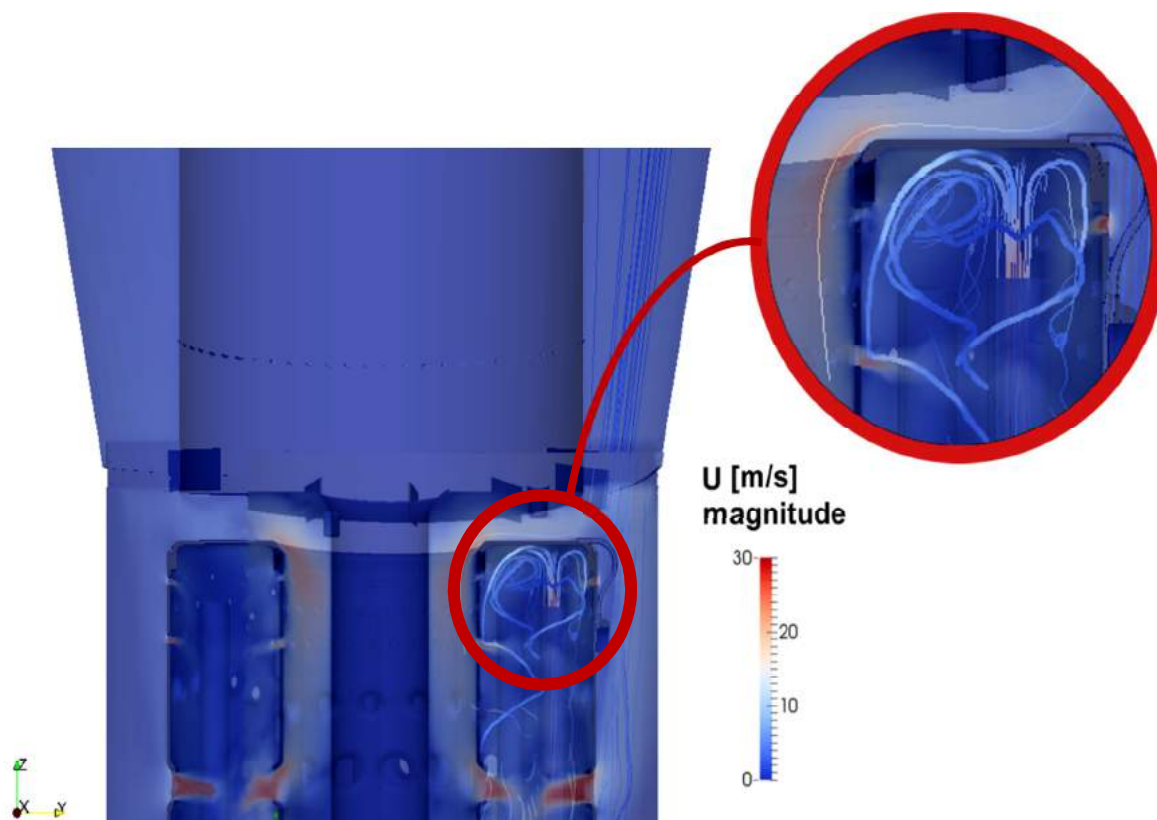


Figure 48: Recirculation zone for the Ax7 case.

In Figure 48, the recirculation zone in the primary zone of the combustion chamber is clearly visible.

It is important to keep in mind that the flow through the combustion chamber is not steady state. The flows through the holes are continually fluctuating. In order to demonstrate this fluctuation the mass flow through hole-set B3 for the Ax4 case was chosen and is shown over time in Figure 49.

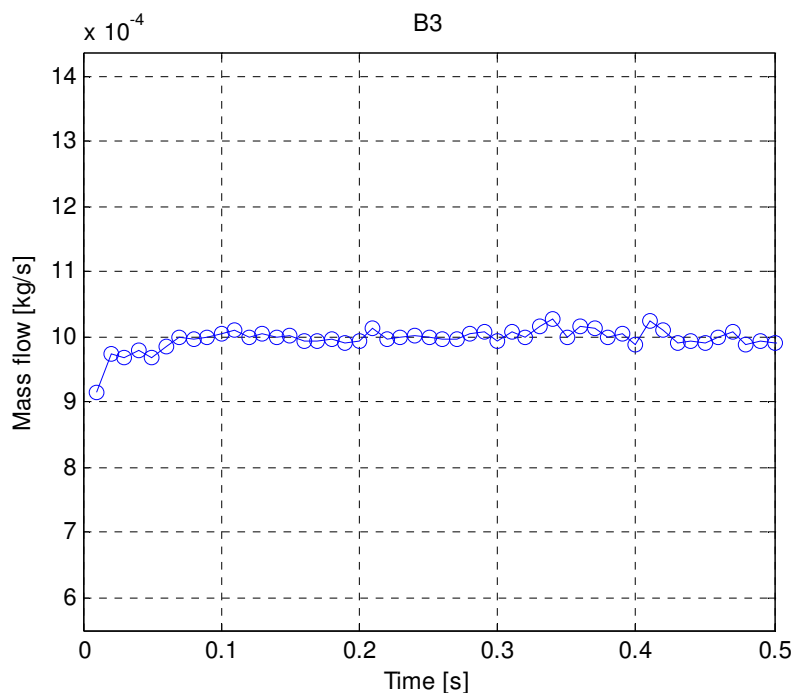


Figure 49: Mass flow fluctuations over time for hole-set B3 for the Ax4 case.

The mass flow distribution obtained experimentally is an approximation of the actual mass flow distribution. Therefore it was decided to average the mass flow rates obtained numerically over time in order to be able to compare the mass flow distribution obtained experimentally to the mass flow distribution obtained numerically.

The mass flow through the holes was determined by surface integrating the velocity through the holes and then averaging that value over time. The calculated mass flow percentages for each case (Ax1-Ax7) had negligible differences and therefore the average mass flow percentage through each set of holes was calculated and is presented below in Table 20.

Table 20: Mass flow distribution as predicted by the numerical simulation compared to the experimental results.

Hole set	Mass flow CFD%	Mass flow experiment %
A1	2.52	2.87
A2	2.49	3.24
A3	2.43	3.00
A4	11.55	13.74
A5	20.61	18.02
A6	5.30	6.73
B1	0.55	1.75
B2	2.79	3.39
B3	2.87	3.69
B4	8.00	6.92
B5	24.98	18.73
Vaporizer Tubes and Cooling holes	15.92	19.44

As can be seen from Table 20 the results from the numerical simulation correspond well to the experimental results overall. The mass flow distribution obtained numerically does not differ from the experimental results with more than 1.5 % in most cases.

The results obtained for the outer liner are more accurate overall, excluding the mass flow percentage obtained for the Vaporizer tubes and cooling holes. The results obtained for the inner liner however, have a larger difference in predicted mass flow distribution. It can also be seen from Table 20 that the numerical model predicted that 39.18 % of the mass flow, would flow through the inner liner as opposed to the 34.48 % determined experimentally. The extra predicted mass flow contributes to a larger discrepancy.

The numerical model therefore suggests that the mass flow distribution is not mainly a function of the effective hole area, but a much more complicated function involving the size of the hole and the pressure drop across it as well as the duct geometry and flow conditions around the hole as suggested by Lefebvre and Ballal (2010: 120).

The assumptions made in Section 3.1 need to be analysed. Assumption 4 states that the pressure drop across the liner is constant at any point along the liner. The numerical solution predicts that assumption 4 is valid for the outer liner, but not

for the inner liner. Figure 50 shows the pressure distribution in the combustion chamber and combustion chamber housing for the Ax7 case.

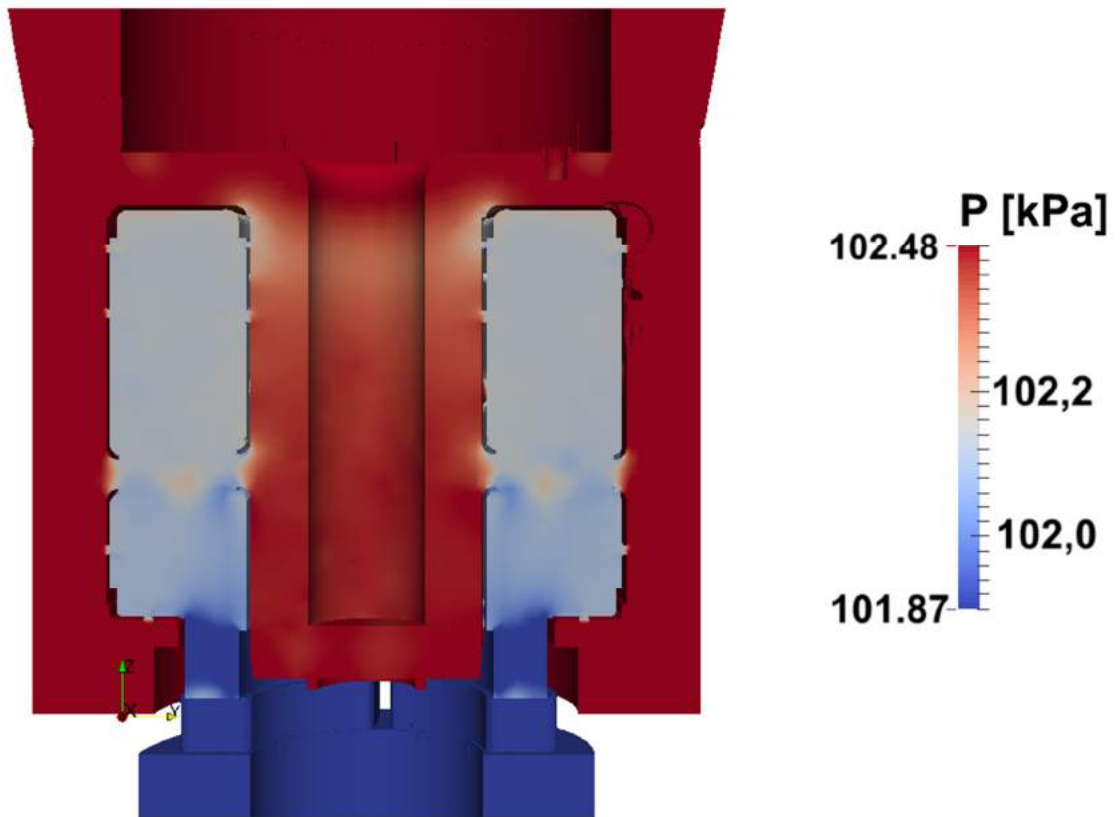


Figure 50: Pressure distribution through the combustor for the Ax7 case.

Table 21 shows the pressure difference across all the sets of holes.

Table 21: Pressure difference through the hole-sets for the Ax7 case.

Hole Set	ΔP [Pa]
A1	287.6832
A2	289.3246
A3	286.2486
A4	293.7506
A5	310.3712
A6	310.1145
B1	93.2704
B2	138.4413
B3	187.4169
B4	208.3319
B5	270.8267

From Table 21 it can be seen that Assumption 4 is fairly accurate for the outer liner, as the pressure differences differ minimally from one another, with no more than 25 Pa difference between any one of the sets of holes. However, the same cannot be said for the inner liner, as the pressures differ up to 178 Pa from one hole-set to another. Therefore Assumption 4 is not valid for the inner liner and this could explain the discrepancies between the experimental and numerical results.

The discovery of the incorrect assumption indicates that the experimental method used is not completely accurate for this combustion chamber. However, it is still concluded that the flow structures obtained numerically are a fairly accurate representation of the physical flow phenomena, due to the good correlation obtained for the outer liner and the fact that Assumption 4 does not have an influence on the numerical results.

Assumption 3 in Section 3.1 states that the pressure drop over the combustion chamber liner is directly equivalent to the pressure drop over the system. This assumption is valid, as can be seen from Table 22.

Table 22: Pressure drop over the combustion chamber compared to the pressure drop over the entire system for the axial cases.

Case	Inlet Velocity [m/s]	Pressure drop over the Combustion Chamber [Pa]	Pressure drop over the system [Pa]
Ax1	1.0830	60.0	456.92
Ax2	1.1657	72.14	530.75
Ax3	1.2492	79.95	618.09
Ax4	1.3316	87.99	692.94
Ax5	1.4590	102.17	727.14
Ax6	1.5441	118.32	812.88
Ax7	1.6284	130.90	895.41

From the data in Table 22, it can be calculated that the constant relation between the pressure drop over the liner and the pressure drop over the system is:

$$h = \Delta P_{system} - \Delta P_{liner} \quad (6.1)$$

$$b = h(i + 1) - h(i) = constant \quad (6.2)$$

The variable b was plotted in order to demonstrate Equation 6.2. and is shown in Figure 51.

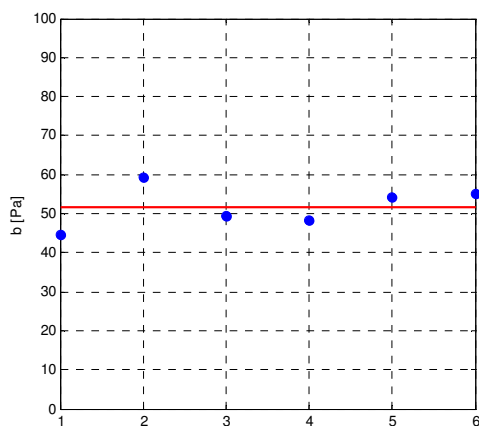


Figure 51: The constant relation between the pressure drop over the system and the pressure drop over the liner.

From Figure 51 it can be seen that the difference is no more than 15 Pa. This difference is negligible and validates Assumption 3. This leads to the conclusion that the numerical model is accurate and is a useful tool for modelling the combustion chamber of a micro-gas turbine engine.

Another simulation was run at an inlet mass flow closer to operating conditions. The operating conditions of the BMT120 KS micro-gas turbine engine range from idle 34 krpm and 0.071 kg/s to 120 krpm and 0.287 kg/s (Krige, 2015). Therefore another simulation was run at a mass flow of 0.287 kg/s and simulation inlet velocity of 11.9 m/s. This was done in order to determine how the mass flow distribution would change at operating conditions.

Table 23: Mass flow distribution through the combustion chamber at operating conditions.

Hole set	Mass flow %
A1	2.37
A2	2.33
A3	2.28
A4	11.55
A5	20.44
A6	4.95
B1	0.44
B2	2.44
B3	2.73
B4	7.86
B5	25.30
Vaporizer Tubes and Cooling holes	17.28

From Table 23 it can be seen that the mass flow distribution is not affected significantly. The only major difference is that the prediction for the mass flow percentage through the vaporizer tubes and cooling holes is closer to the value determined experimentally. It can therefore be concluded that the test section is an adequate means by which to measure the mass flow distribution for the BMT120-KS micro-gas turbine combustion chamber. Figure 52 shows the stream lines through the combustion chamber at operating conditions.

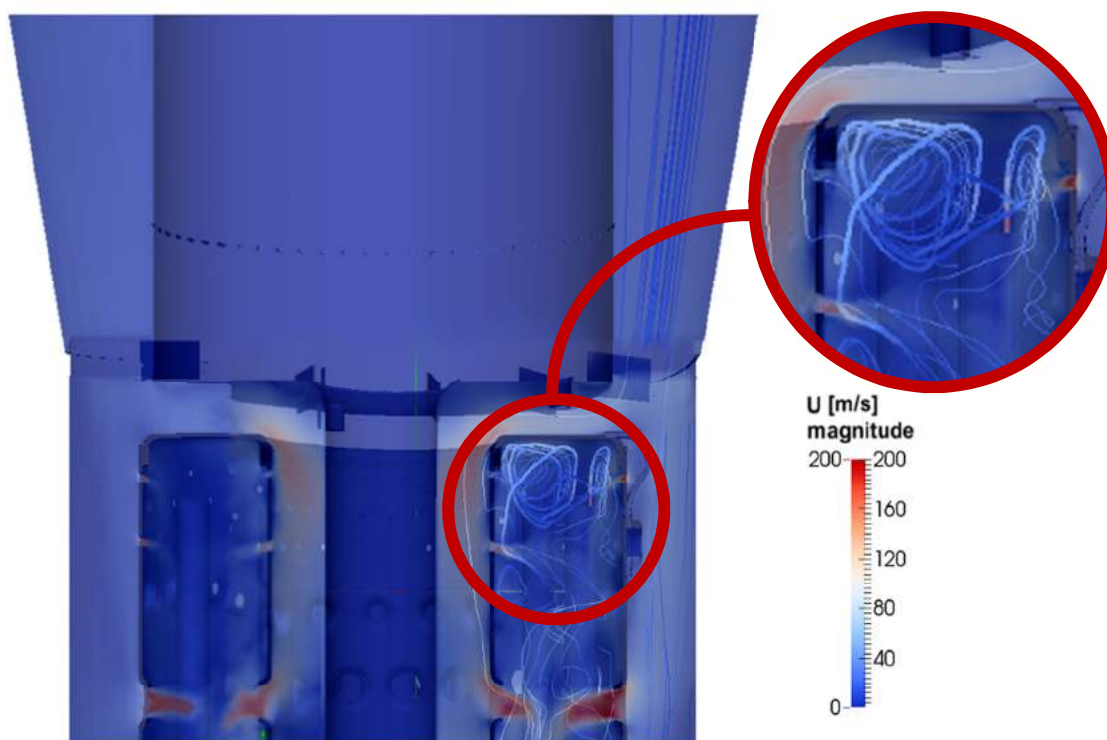


Figure 52: Recirculation zone produced under operating conditions.

From Figure 52 it can be seen that the recirculation zone is more well-defined than for lower inlet velocities and the impinging jets can more clearly be seen. Therefore, it can be concluded that if the model geometry is modified in order to simulate the micro-gas turbine engine, accurate results should be easily obtainable.

6.2. Comparison of the Swirling Flow Case to the Axial Flow Case

The primary objective of this project was to investigate whether an element of swirl in the inlet flow would affect the mass flow distribution through the combustion chamber. In order to achieve this objective, inlet guide vanes were designed to impart swirl into the flow. It was decided to investigate two degrees of swirl. The two inlet guide vane geometries were added to the numerical simulations respectively. They were also tested experimentally. The experimental results were compared to the experimental results obtained from the axial case. Table 24 shows the comparison of the average mass flow distributions obtained experimentally from the swirling cases to axial case.

Table 24: Experimental average mass flow distribution of the swirling cases compared to the axial case.

Case	Axial	R7 Swirler	R9 Swirler
Hole set	Mass flow distribution [%]		
A1	2.87	2.99	2.66
A2	3.24	3.20	2.96
A3	3.00	3.25	2.94
A4	13.74	13.66	13.49
A5	18.02	18.30	17.88
A6	6.73	6.71	6.57
B1	1.75	1.59	1.97
B2	3.39	3.46	3.86
B3	3.69	3.54	4.04
B4	6.92	7.07	6.92
B5	18.73	18.88	18.53
Cooling and Vaporizer Tubes	19.44	20.40	20.23
Total	101.51	103.05	102.03

As can be seen from Table 24, imparting swirl into flow has a negligible influence on the mass flow distribution. The scatter observed between the axial and swirling experiments is no larger than the scatter observed while doing repeatability tests for the axial flow. It can also be observed that the degree of swirl does not have a significant impact on the mass flow distribution.

The numerical results obtained for the swirling flow was also compared to the experimental results for the swirling cases. The case with the largest swirling angle is presented. The results are summarized in Table 25.

Table 25: Comparison of the numerical results and experimental results for swirling flow R7 cases.

Hole set	Mass flow CFD%	Mass flow experiment %
A1	2.61	2.99
A2	2.52	3.20
A3	2.44	3.25
A4	12.17	13.66
A5	21.47	18.30
A6	5.50	6.71
B1	0.47	1.59
B2	2.41	3.46
B3	2.83	3.54
B4	8.31	7.07
B5	24.51	18.88
Vaporizer Tubes and Cooling Holes	14.74	20.40

From Table 25 it can be seen that the numerical simulation models the physical problem reasonably accurately. The inaccuracies are due to the fact that the assumptions made for the experimental method are only valid for the outer liner.

It is once again important to recollect that the physical flow through the combustion chamber is not steady state. Therefore the above mentioned results were averaged as was done for the axial flow case. It is interesting to compare the fluctuations of mass flow over time obtained numerically through hole-set B3 for the R7.4 and R9.4 cases to the Ax4 case this is shown in Figure 53.

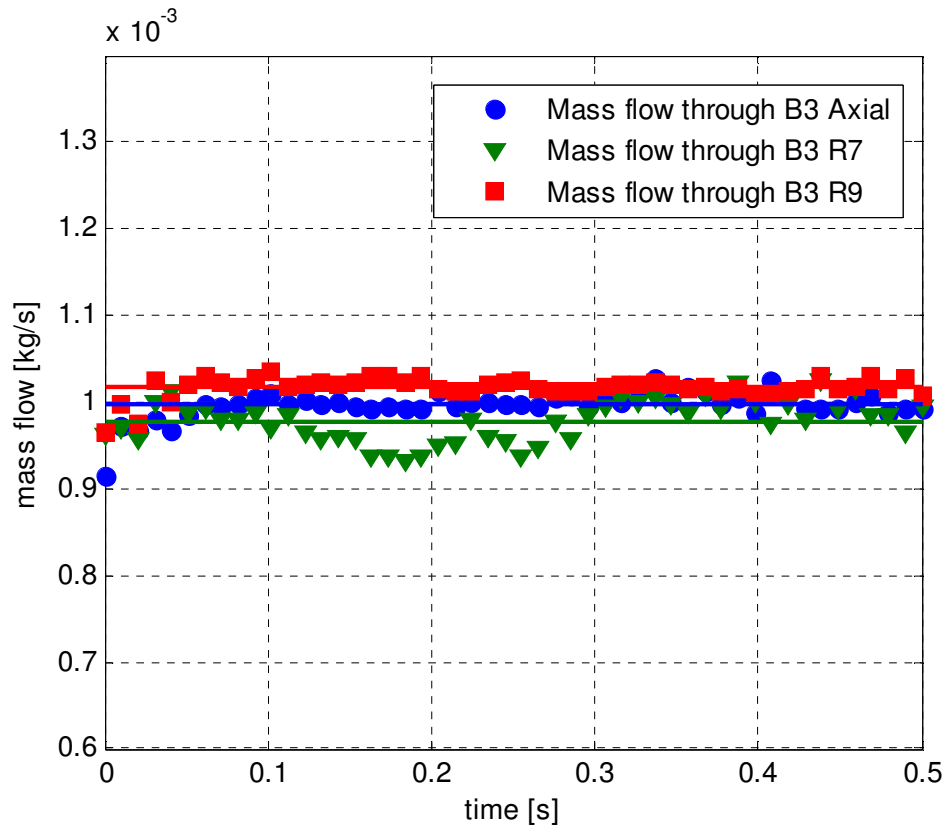


Figure 53: Comparison of the mass flow over time through hole-set B3 of the Ax4 case, R7.4 case and the R9.4 case.

As can be seen from Figure 53, the fluctuations over time are very similar for all the degrees of swirl. This corresponds to the findings that the mass flow distribution is unaffected by swirl. It can also be seen that case with the R7.4 swirling case experienced the largest fluctuations, but the fluctuations are negligibly small and it is therefore concluded that the influence of swirl on the mass flow distribution is negligibly small.

Figure 54 shows the velocity streamlines through the R7.7 swirling flow case.

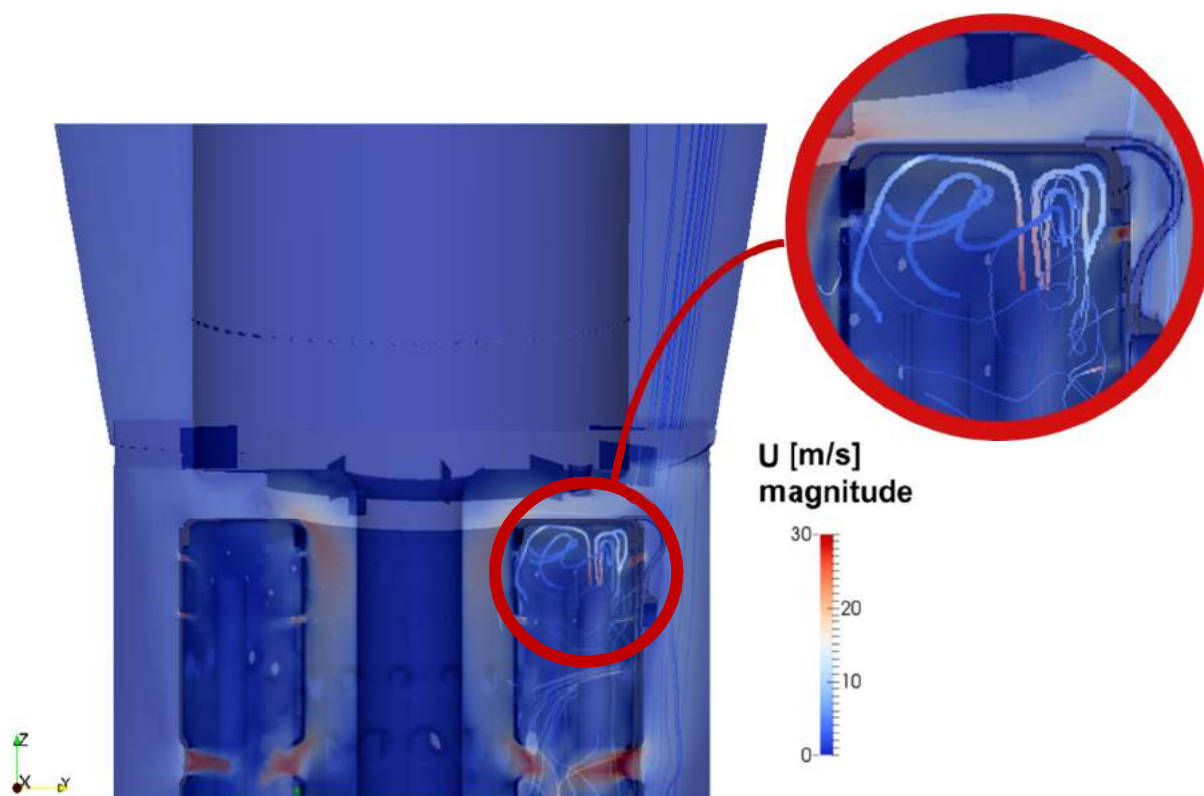


Figure 54: Recirculation zone produced in the R7.7 case.

From Figure 54 it can be seen that the recirculation zone is not nearly as well defined as in the axial flow case. This was also observed for the R9.7 case. The R9.7 case along with other additional results can be found in Appendix D.

The findings of this project indicate that the influence of inlet swirl on the mass flow distribution is negligible, and that the degree of swirl does not have an impact on the results. However, it was found that inlet swirl has a significant influence on the flow structures and therefore may have a negative impact the performance of the combustor.

7. CONCLUSIONS

This project aimed to determine the influence of inlet swirl on the mass flow distribution and flow structures through the BMT120-KS micro-gas turbine engine combustion chamber.

In order to determine the influence of inlet swirl, the axial flow through the combustion chamber was considered. This case served as the control with which the swirling flow cases would be compared. The mass flow distribution for the axial flow was determined experimentally and numerically.

The swirling flow cases were then considered. Two degrees of swirl were considered in order to determine whether the degree of swirl would have an impact on the results. The results for both the swirling flow cases were also determined experimentally and numerically.

The comparison of the axial flow cases with the swirling flow cases revealed the influence of inlet swirl on the mass flow distribution. The experimental results were used to validate the numerical results. Once the numerical models were validated, the flow structures within the combustor could be investigated and further influence of the inlet swirl could be determined.

7.1. Findings and Implications

The axial case served as the control with which the swirling flow cases could be compared. It was concluded that the numerical model of the axial flow case sufficiently predicted the mass flow distribution through the combustor when compared to the experimental results.

Assumption 4 was fairly accurate for the outer liner, as the pressures differences differ minimally from one another, with no more than 25 Pa difference between any one of the sets of holes. However, the same could not be said for the inner liner, as the pressures differed up to 178 Pa from one hole-set to another. Therefore Assumption 4 was concluded not to be valid for the inner liner and discrepancies were accredited to the inaccuracy of Assumption 4 in Section 3.

The discovery of the incorrect assumption indicated that the experimental method used is not completely accurate for this combustion chamber. However, it was still concluded that the flow structures obtained numerically were a fairly accurate representation of the physical flow phenomena, due to the good correlation obtained for the outer liner and the fact that Assumption 4 did not have an influence on the numerical results

The test rig at Stellenbosch University used during the experimental procedure was unable to produce a high enough inlet velocity to simulate engine operating conditions. A numerical model was used in order to determine whether increasing the inlet velocity significantly (to simulate operating conditions) would have an impact on the mass flow distribution. It was concluded that any changes observed in the mass flow distribution were negligible and that the mass flow distribution therefore remained constant. Inspecting the flow structures revealed a more well-defined recirculation zone than for the low inlet velocity axial cases.

The experimental results of the swirling flow cases were then compared to the axial cases. It was found that the influence of the inlet swirl on the mass flow distribution was negligible and that the degree of swirl had an insignificant impact on the results.

The swirling numerical cases were then validated by comparing the mass flow distributions obtained numerically with the mass flow distributions obtained experimentally. The same conclusions were drawn as for the axial flow case. The numerical model predicted the mass flow through the outer liner well, but

encountered some discrepancies in the mass flow distribution through the inner liner. This was once again attributed to the inaccurate assumption made during the experimental process.

When the flow structures within the combustor were inspected however, it was found that the recirculation zone was not nearly as well defined as for the axial flow case.

It was therefore concluded that inlet swirl has a negligible influence on the mass flow distribution through the BMT120-KS micro-gas turbine engine's combustor, but that it does have a significant impact on the flow structures and might negatively affect combustor performance.

7.2. Recommendations

During this project it was found that Assumption 4 in Section 3 was inaccurate. It is therefore recommended that the experimental procedure to be adapted to more closely represent the mathematical models presented by Lefebvre and Ballal (2010: 120-122) and by Adkins and Gueroui (1986: 491-497). In order to accomplish this, the total pressure upstream of the hole and the static pressure downstream of the hole should be measured. The scale of the micro-gas turbine combustor makes this problematic, since conventional methods for pressure measurements would disrupt the flow or block the flow path.

Therefore it is suggested that research be done regarding Pressure-sensitive Paints (PSP), as they are a potential method with which to measure the necessary pressures for determining the mass flow through the liner holes more accurately.

This thesis concluded that inlet swirl has a negligible influence on the mass flow distribution, but that it does indeed have a significant influence on the internal flow structures. The implications of this have not been investigated in this thesis. It is recommended that the combustor performance be analysed under combustion conditions for cases where there is an element of swirl present in the inlet flow.

REFERENCES

- 2014a. *Realisable k-epsilon model* [Online]. [www.cfd-online/Wiki/Realisable k-epsilon model](http://www.cfd-online/Wiki/Realisable_k-epsilon_model). [Accessed 13th of August 2015].
- 2014b. *Technical Information: Cerabar M PMC51, PMP51, PMP55* [Online]. https://portal.endress.com/wa001/dla/5000262/1149/000/09/TI00436PEN_2015.pdf: Endress and Hauser. [Accessed 25th of July 2014].
- 2014c. *Technical Information: Deltabar M PMD55* [Online]. https://portal.endress.com/wa001/dla/5000557/8051/000/10/TI00434PEN_1814.pdf: Endress and Hauser. [Accessed 25th of July 2014].
- 2015a. *BMT120-KS* [Online]. <http://www.bairdtech.com>: Baird MicroTurbines. [Accessed 6th July 2015].
- 2015b. *Heavy-Duty Gas Turbine Overview* [Online]. <https://powergen.gepower.com/plan-build/products/gas-turbines/index.html>: General Electric. Available: <https://powergen.gepower.com/plan-build/products/gas-turbines/index.html> [Accessed 23rd October 2015].
- 2015c. *Trent 7000 Making the best better* [Online]. <http://www.rolls-royce.com/customers/civil-aerospace/products/civil-large-engines/trent-7000.aspx#Overview>: Rolls-Royce. [Accessed 23rd October 2015].
- ADKINS, R. C. & GUEROUI, D. 1986. An Improved Method for Accurate Prediction of Mass Flows Through Combustor Liner Holes. *Journal of Engineering for Gas Turbines and Power*, 108, 491-497.
- BOYCE, M., 2002. *Gas Turbine Engineering Handbook, Second Edition (Incompressible Flow Turbomachines)*, Gulf Professional Publishing, United Kingdom.
- BUSINESS-INSIDER. 2015. The Drones Report: Market forecasts, regulatory barriers, top vendors, and leading commercial applications. *Tech* [Online].
- ÇENGEL, Y. A. & BOLES, M. A., 2006. *Thermodynamics : an engineering approach*, McGraw-Hill Higher Education, Boston.
- DE VILLIERS, L. C. B. 2014. *Design of a Centrifugal Compressor for Application in Micro Gas Turbines*. M.Eng Research (Mechanical), Stellenbosch University.
- GIERAS, M. & STANKOWSKI, T. 2012. Computational study of an aerodynamic flow through a micro-turbine engine combustor. *Journal of Power Technologies*, 92, 68-79.
- GONZALEZ TORO, C. A., WONG, K. C. & ARMFIELD, S. 2008. Computational study of a micro-turbine engine combustor using Large Eddy Simulation and Reynolds Averaged turbulence models. *ANZIAM Journal*, 49, 407-422.

- ISO, 2003. Measurement of fluid flow by means of pressure differential devices inserted in circular-cross section conduits running full - Part 2: Orifice plates. *ISO 5167-2*. Switzerland: International Standards Organization.
- KARTHIK, T. S. D., 2011. Turbulence Models and Their Applications. Indo German Winter Academy: Department of Mechanical Engineering IIT Madras.
- KAYS, W., CRAWFORD, M. & WEIGAND, B., 2005. *Convective heat and mass transfer*, McGraw-Hill, Singapore.
- KRIGE, D. S. 2013. *Performance Evaluation of a Micro Gas Turbine Centrifugal Compressor Diffuser*. M.Sc (Mechanical Engineering), Stellenbosch University.
- KRIGE, D. S. 2015. *RE: BMT120-KS Performance Data*.
- KRÖGER, D. G., 1998. *Air-cooled Heat Exchanges and Cooling Towers: Thermal-flow performance evaluation and design*, Department of Mechanical Engineering University of Stellenbosch, South Africa.
- LEFEBVRE, A. & BALLAL, D., 2010. *Gas Turbine Combustion: Alternative Fuels and Emissions*, Taylor & Francis, United States.
- LIEBLEIN, S., 1950. Turning-Angle Design Rules for Constant-Thickness Circular-Arc Inlet Guide Vanes in Axial Annular Flow. Lewis Flight Propulsion Laboratory, Cleveland, Ohio.
- NREC, 1980. *The design and development of gas turbine combustors*, Northern Research and Engineering Corp., Woburn, Mass.
- OLIVIER, A. J. 2015. *An Experimental and Numerical Investigation of Vaporizer Tubes Associated with Micro Gas Turbines*. M.Eng Research (Mechanical), Stellenbosch University.
- OPENFOAM. 2013. *OpenFOAM: The Open Source CFD Toolbox User Guide* [Online]. foam.sourceforge.net/docs/Guides-a4/UserGuide.pdf: OpenFOAM Foundation. [Accessed 5th November 2013].
- SAYERS, A. T., 1990. *Hydraulic and Compressible Flow Turbomachines*, McGraw-Hill, the University of Michigan.
- SHIH, T., LIOU, W. W., SHABBIR, A., YANG, Z. & ZHU, J. 1995. A new k- ϵ eddy viscosity model for high reynolds number turbulent flows. *Computers and Fluids*, 24, 227-238.
- VAN DER MERWE, B. B. 2012. *Design of a Centrifugal Compressor Impeller for Micro Gas Turbine Application*. M.Eng Research (Mechanical), Stellenbosch University.
- VERSTEEG, H. K. & MALALASEKERA, W., 2007. *An Introduction to Computational Fluid Dynamics: The Finite Volume Method*, Pearson Education Limited, United Kingdom.

ZHU, G., LAI, M. C. & LEE, T. 1995. Penetration and Mixing of Radial Jets in Neck-Down Cylindrical Crossflow. *Journal of Propulsion and Power*, 11, 252-260.

APPENDIX A: TECHNICAL DRAWINGS

A.1. Inlet Guide Vane Technical Drawings

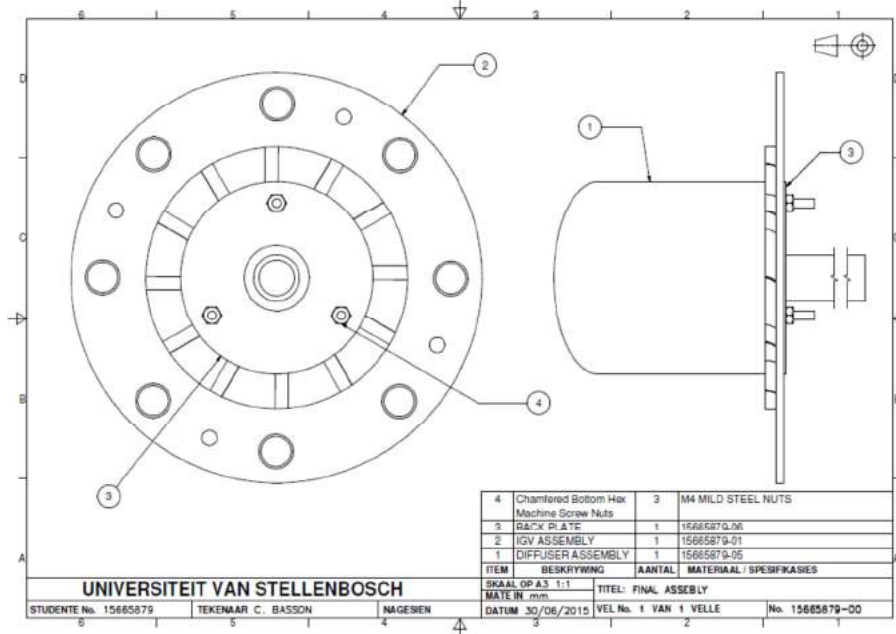


Figure A. 1: Inlet guide vane and diffuser assembly.

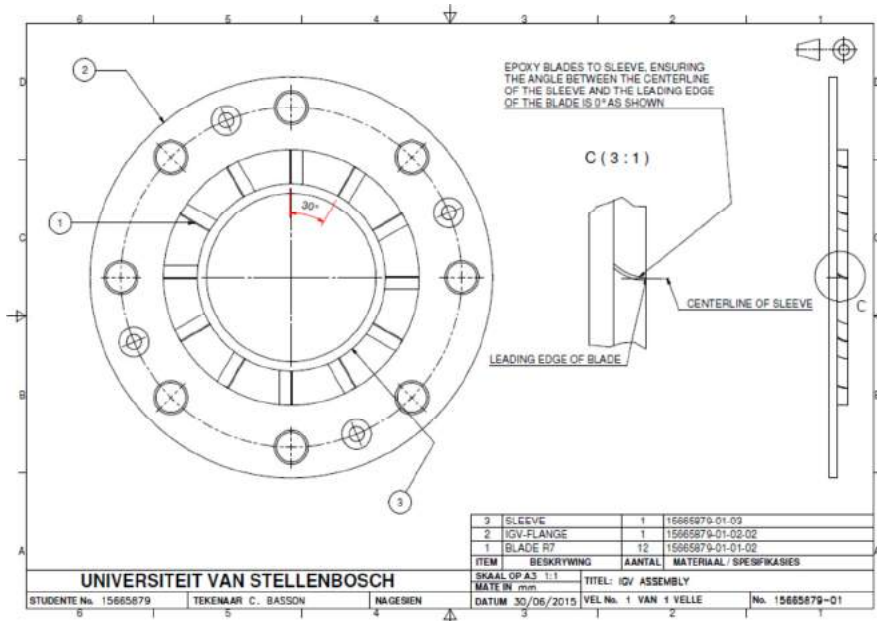


Figure A. 2: Inlet guide vane assembly.

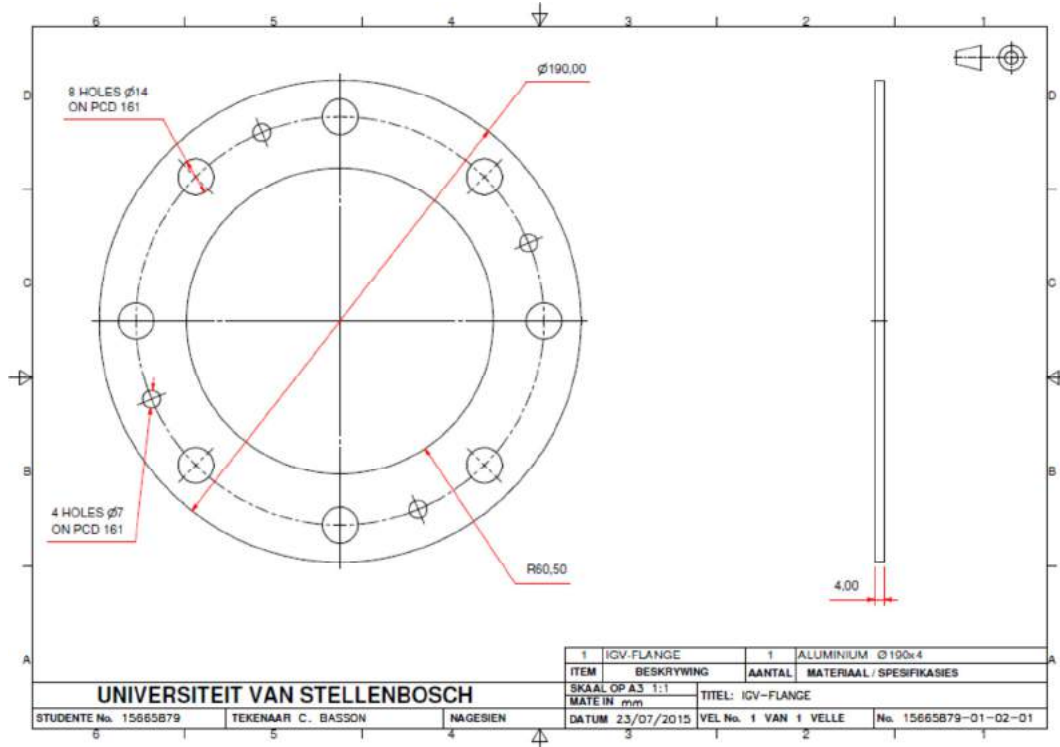


Figure A. 3: Flange acting as shroud

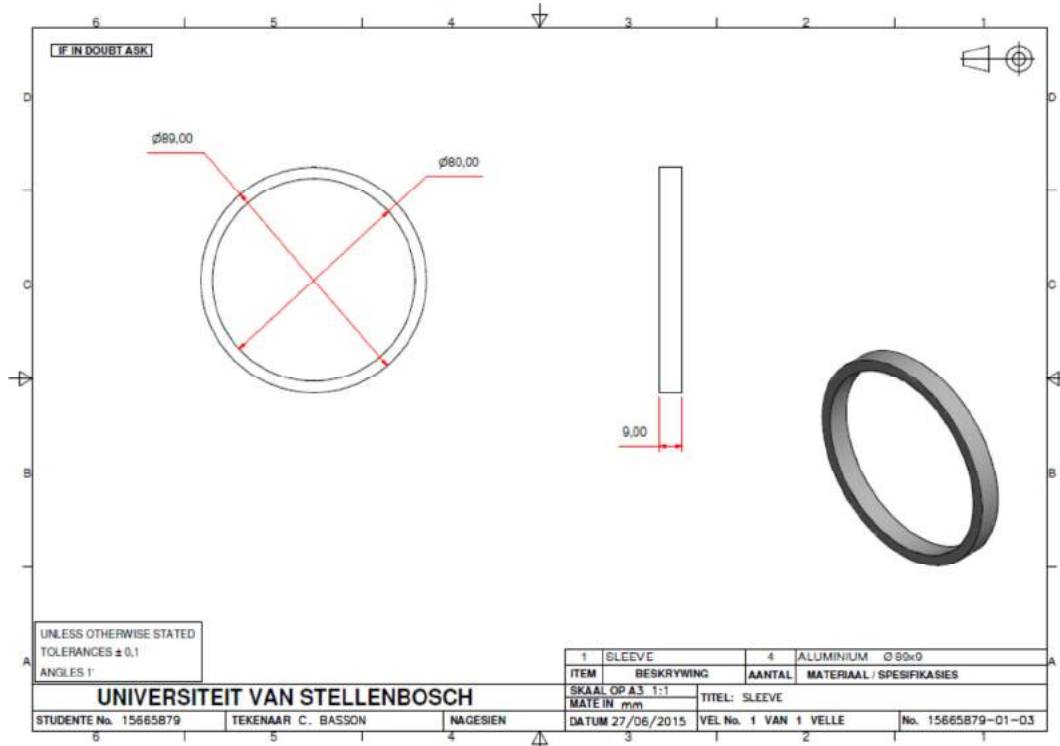


Figure A. 4: Sleeve acting as hub.

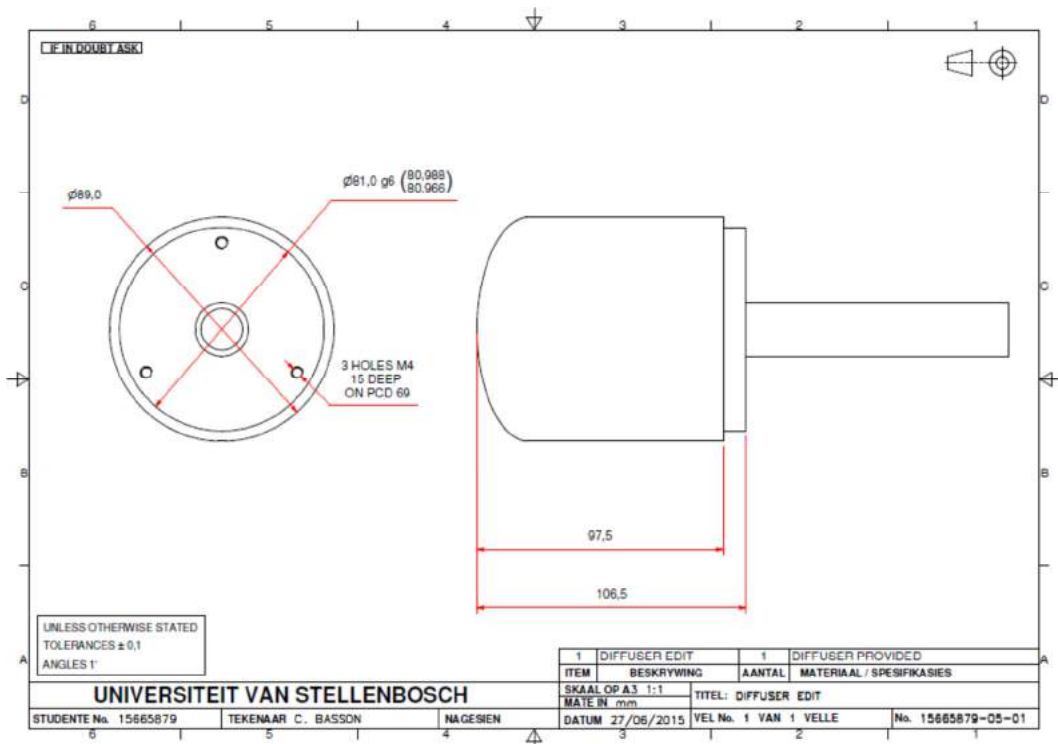


Figure A. 5: Modified diffuser.

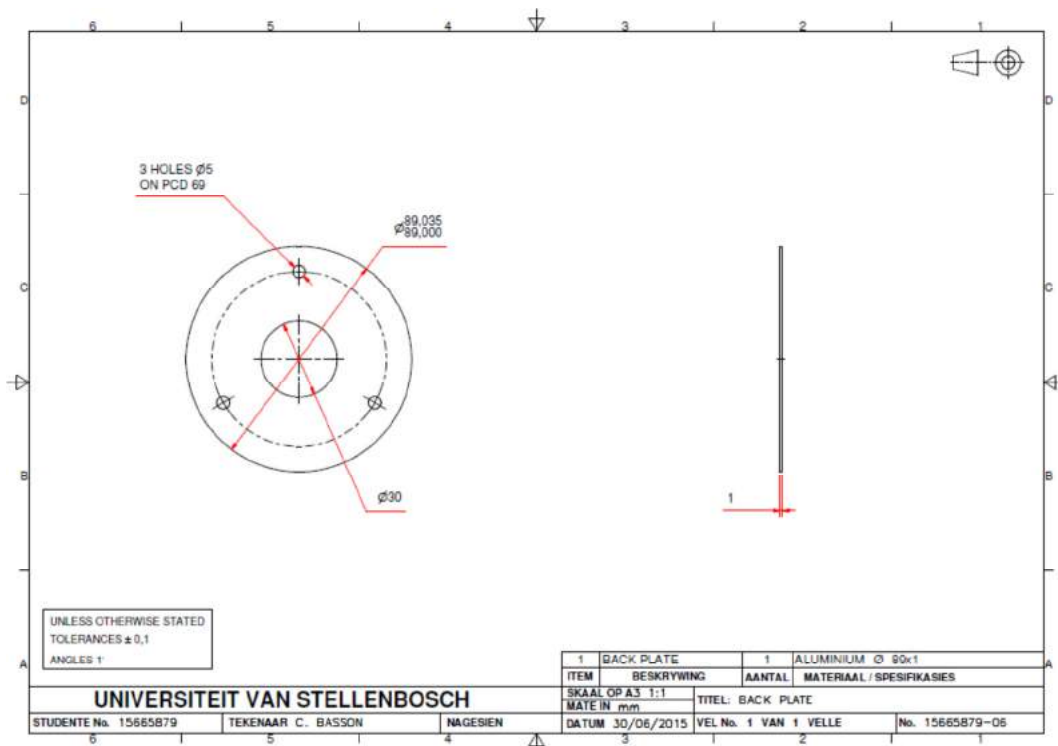


Figure A. 6: Back plate.

A.2. Computational Domain Technical Drawings

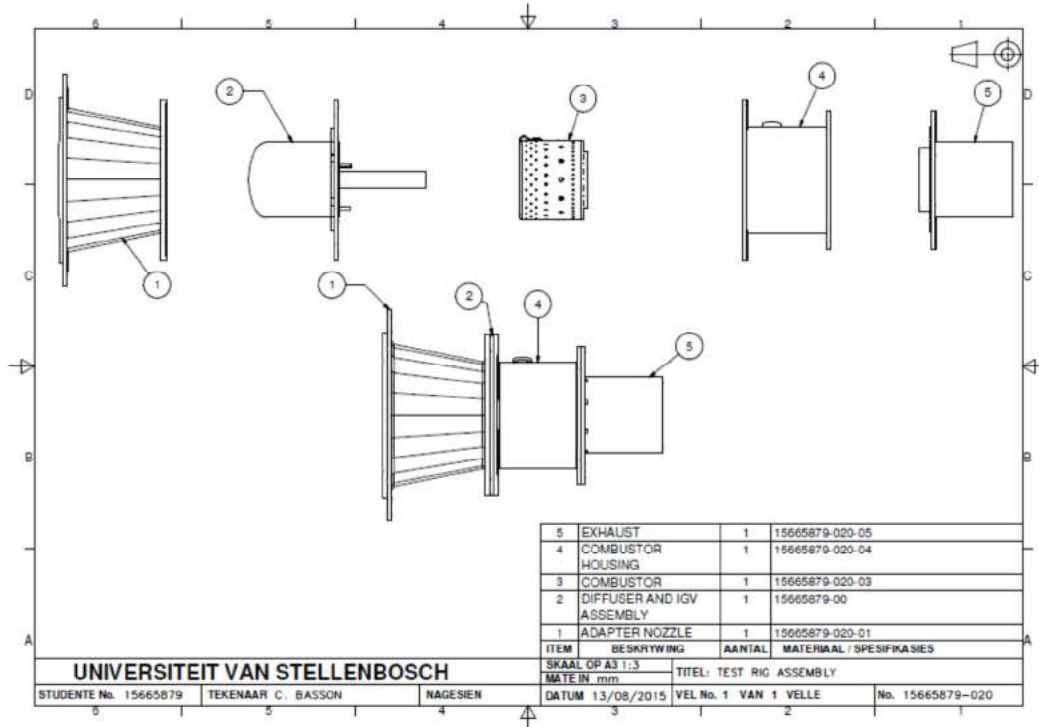


Figure A. 7: Test section assembly.

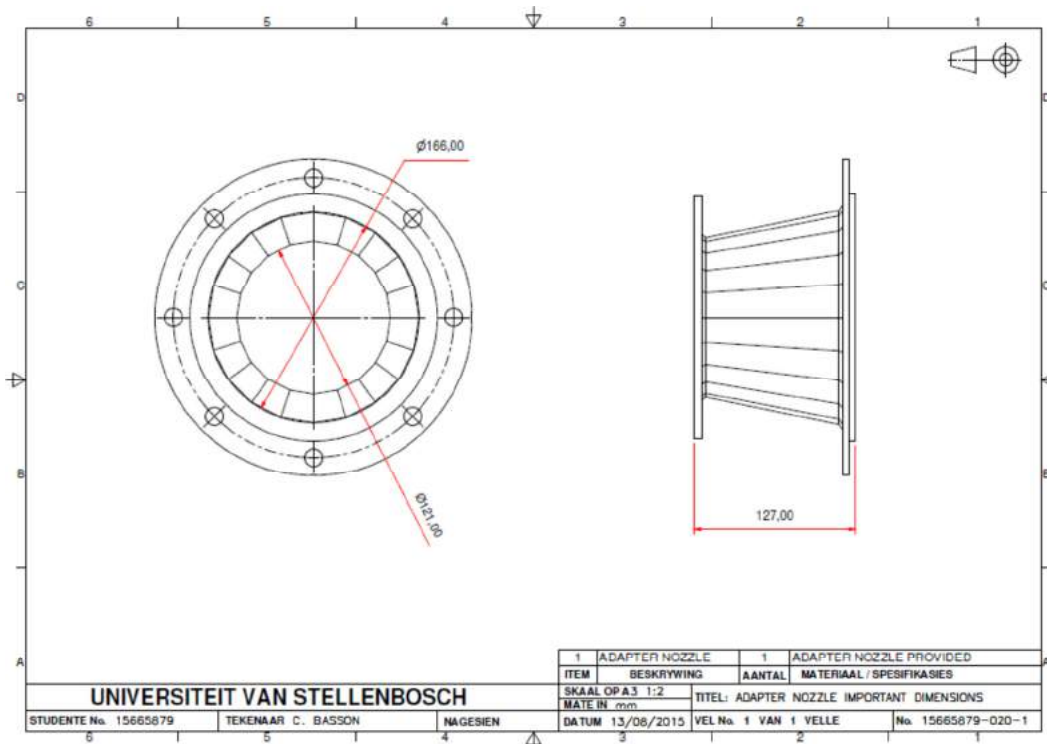


Figure A. 8: Relevant adapted nozzle dimensions.

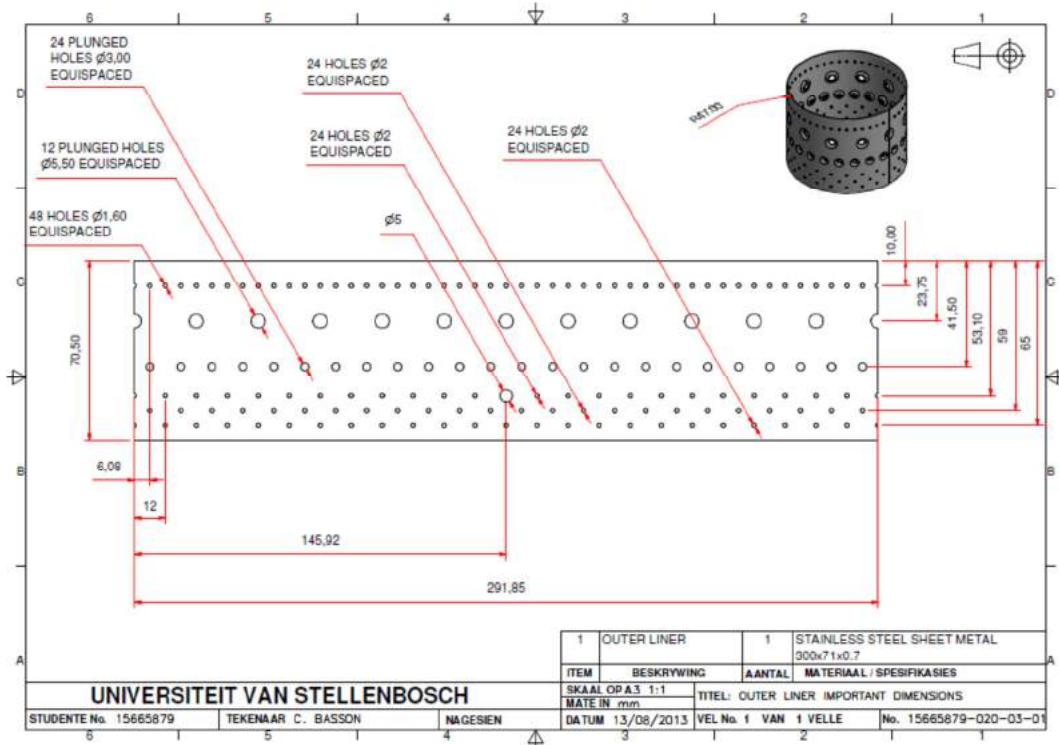


Figure A. 9: Relevant outer liner dimensions.

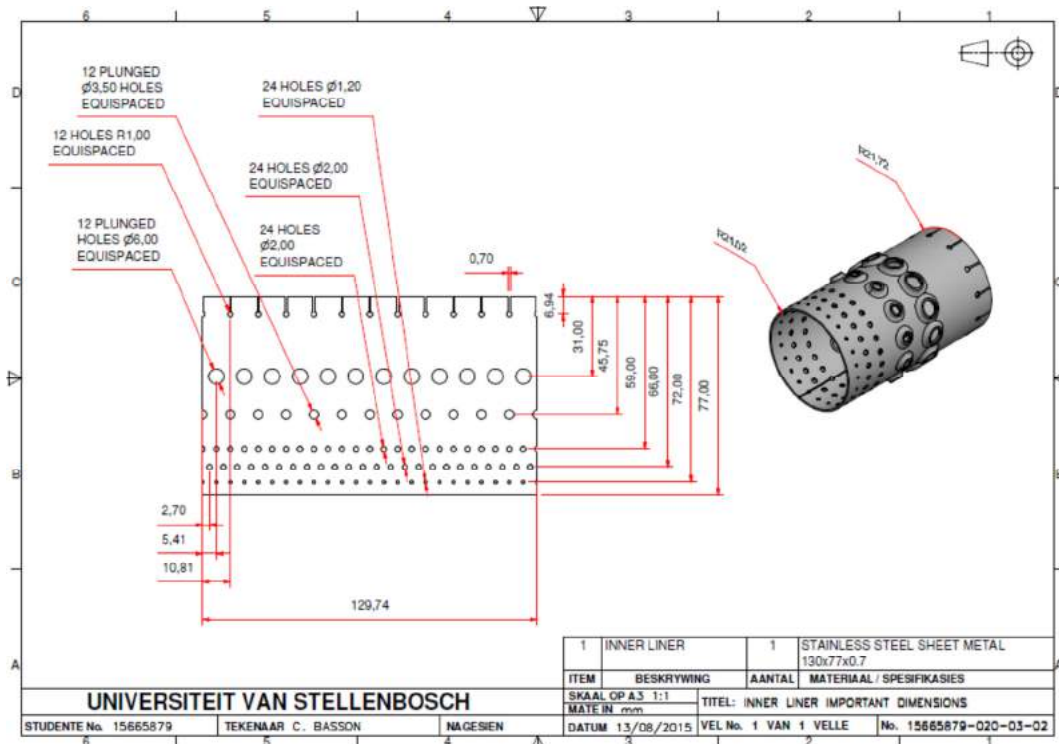


Figure A. 10: Relevant inner liner dimensions.

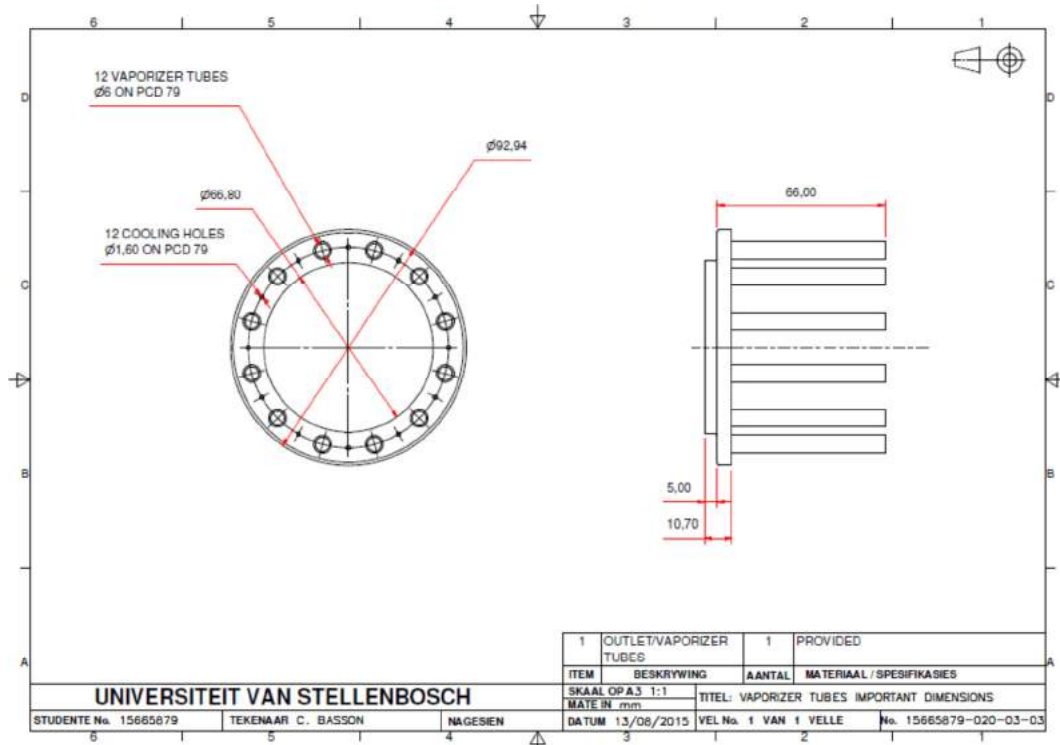


Figure A. 11: Relevant vaporizer tubes dimensions.

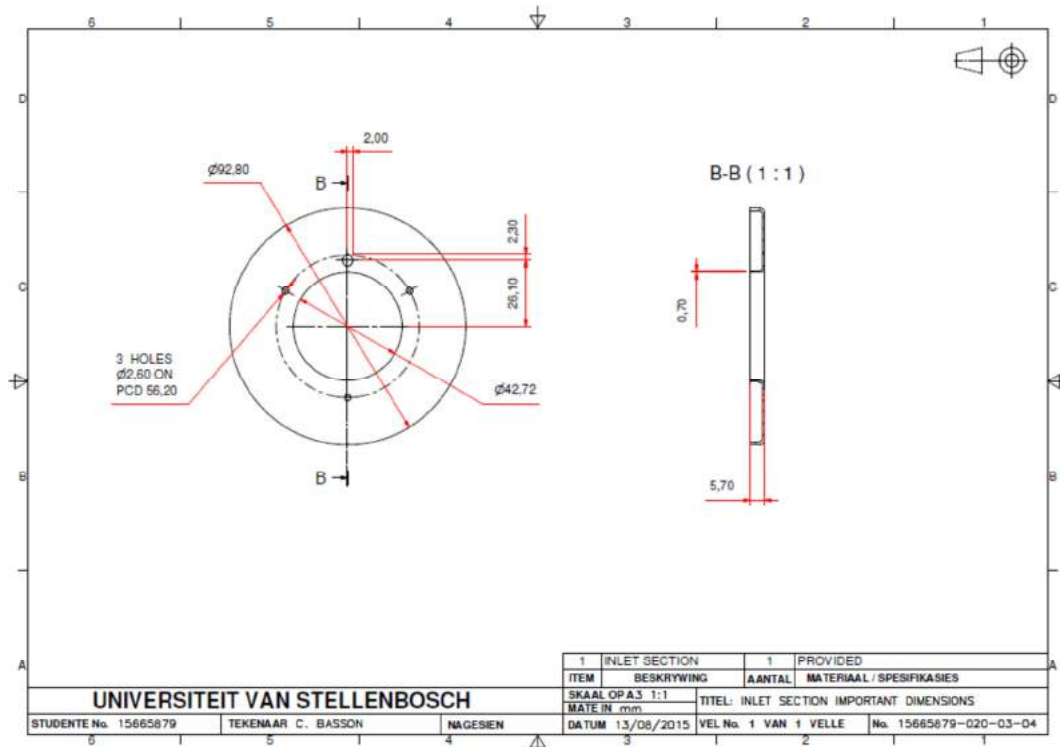


Figure A. 12: Relevant combustion chamber inlet section dimensions.

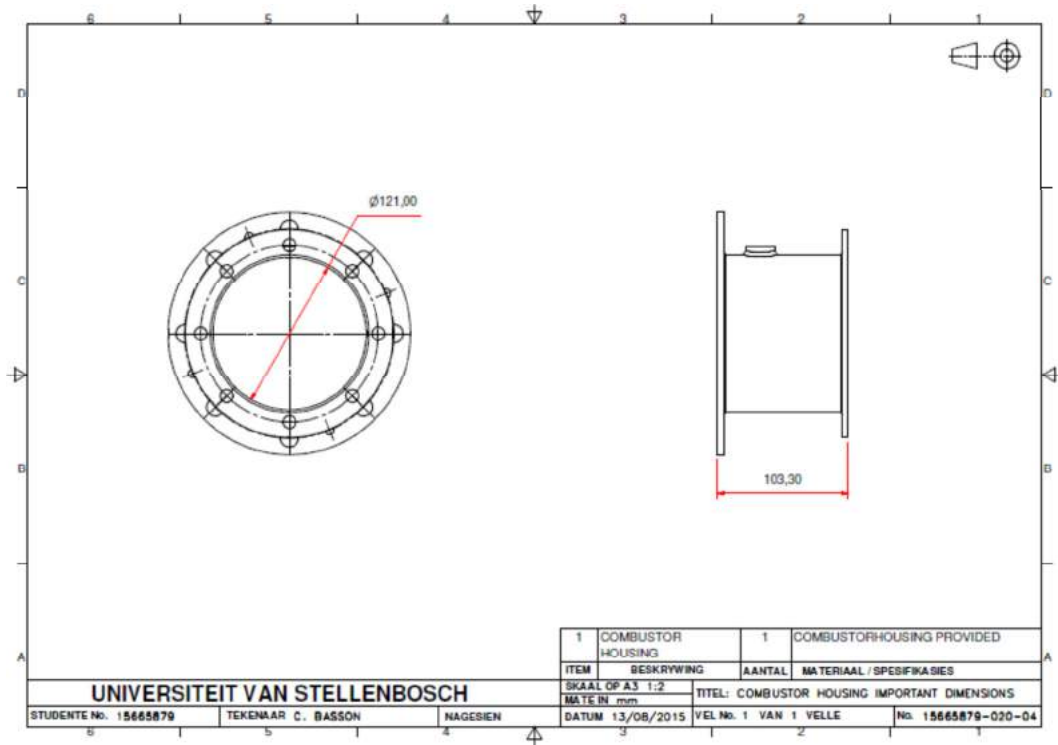


Figure A. 13: Relevant combustion chamber housing dimensions.

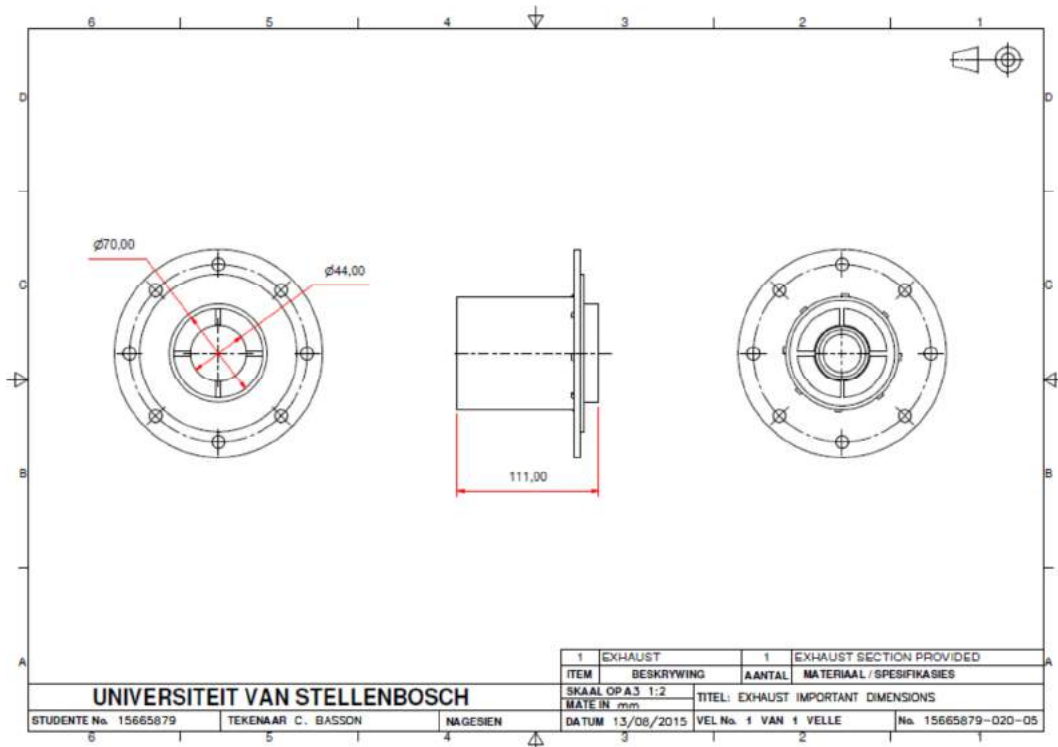


Figure A. 14: Relevant exhaust dimensions.

APPENDIX B: CASE FILES FOR FLOW SIMULATIONS

Various files were used to set up the numerical simulations. The swirling flow simulations only varied slightly from the axial flow simulations. Therefore only the files that were changes are shown in Section B.2.

B.1. Case Files for the Axial Flow Case

B.1.1. 0 directory

epsilon

```

dimensions      [ 0 2 -3 0 0 0 0 ];
internalField   uniform 26.663e-6;
boundaryField
{
    Inlet //Adapter nozzle inlet
    {
        type      turbulentMixingLengthDissipationRateInlet;
        mixingLength  0.00575
        value        $internalField;    }
    Outlet //Exhaust outlet
    {
        type      inletOutlet;
        inletValue  $internalField;    }
    Wall //All external domain walls
    {
        type      epsilonWallFunction;
        value      $internalField;    }
    Sym //Symmetry plane
    {
        type      symmetryPlane;    }
    Inlet1 //Inlet section of the combustion chamber
    {
        type      epsilonWallFunction;
        value      $internalField;    }
    OL_weld //Outer liner
    {
        type      epsilonWallFunction;
        value      $internalField;    }
    IL_weld //Inner liner
    {
        type      epsilonWallFunction;
        value      $internalField;    }
    Vap_tubes //Vaporizer tuber_Outlet section of the combustion chamber
    {
        type      epsilonWallFunction;
        value      $internalField;    }
    Complete //All other parts including diffuser, IGV's, shaft placeholder, etc.
    {
        type      epsilonWallFunction;
        value      $internalField;    }
}

```

k

```

dimensions      [ 0 2 -2 0 0 0 0 ];
internalField   uniform 15.198e-6;
boundaryField
{
    Inlet
    {
        type      turbulentIntensityKineticEnergyInlet;
        intensity  0.05; // 5% turbulent intensity
        value      $internalField;    }
    Outlet
    {
        type      inletOutlet;
        inletValue  $internalField;    }
    Wall
    {
        type      kqRWallFunction;
        value      uniform 0;    }
    Sym
    {
        type      symmetryPlane;    }
    Inlet1

```

```

    { type          kqRWallFunction;
      value         uniform 0;    }
  OL_weld
  { type          kqRWallFunction;
    value         uniform 0;    }
  IL_weld
  { type          kqRWallFunction;
    value         uniform 0;    }
  Vap_tubes
  { type          kqRWallFunction;
    value         uniform 0;    }
  Complete
  { type          kqRWallFunction;
    value         uniform 0;    }
}

```

nut

```

dimensions      [ 0 2 -1 0 0 0 0 ];
internalField   uniform 0.7797e-6;
boundaryField
{
  Inlet
  { type          calculated;
    value         uniform 0;    }
  Outlet
  { type          calculated;
    value         uniform 0;    }
  Wall
  { type          nutkWallFunction;
    value         $internalField; }
  Sym
  { type          symmetryPlane; }
  Inlet1
  { type          nutkWallFunction;
    value         $internalField; }
  OL_weld
  { type          nutkWallFunction;
    value         $internalField; }
  IL_weld
  { type          nutkWallFunction;
    value         $internalField; }
  Vap_tubes
  { type          nutkWallFunction;
    value         $internalField; }
  Complete
  { type          nutkWallFunction;
    value         $internalField; }
}

```

nuTilda

```

dimensions      [0 2 -1 0 0 0 0];
internalField   uniform 0;
boundaryField
{
  Inlet
  { type          zeroGradient; }
  Outlet
  { type          zeroGradient; }
  Wall
  { type          zeroGradient; }
  Sym
  { type          symmetryPlane; }
  Inlet1
  { type          zeroGradient; }
  OL_weld
  { type          zeroGradient; }
  IL_weld
  { type          zeroGradient; }
  Vap_tubes
  { type          zeroGradient; }
}

```

```

    Complete
    { type          zeroGradient; }
}

```

P

```

dimensions      [0 2 -2 0 0 0 0];
internalField   uniform 0;
boundaryField
{
    Inlet
    { type          zeroGradient; }
    Wall
    { type          zeroGradient; }
    Outlet
    { type          fixedValue;
      value        83932.049495; }
    Sym
    { type          symmetryPlane; }
    Inlet1
    { type          zeroGradient; }
    OL_weld
    { type          zeroGradient; }
    IL_weld
    { type          zeroGradient; }
    Vap_tubes
    { type          zeroGradient; }
    Complete
    { type          zeroGradient; }
}

```

U

```

dimensions      [0 1 -1 0 0 0 0];
internalField   uniform (0 0 0);
boundaryField
{
    Inlet
    { type          fixedValue;
      value        uniform (0 0 -2.7049); }
    Wall
    { type          fixedValue;
      value        uniform (0 0 0); }
    Outlet
    { type          zeroGradient; }
    Sym
    { type          symmetryPlane; }
    Inlet1
    { type          fixedValue;
      value        uniform (0 0 0); }
    OL_weld
    { type          fixedValue;
      value        uniform (0 0 0); }
    IL_weld
    { type          fixedValue;
      value        uniform (0 0 0); }
    Vap_tubes
    { type          fixedValue;
      value        uniform (0 0 0); }
    Complete
    { type          fixedValue;
      value        uniform (0 0 0); }
}

```

B.1.2. constant directory**RASProperties**

```

RASModel      realizableKE;
turbulence    on;
printCoeffs   on;

```

turbulenceProperties

```
simulationType RASModel;
```

transportProperties

```
transportModel Newtonian;
nu          nu [ 0 2 -1 0 0 0 0 ] 1.5042e-05;
CrossPowerLawCoeffs
{
  nu0          nu0 [ 0 2 -1 0 0 0 0 ] 1e-06;
  nuInf        nuInf [ 0 2 -1 0 0 0 0 ] 1e-06;
  m            m [ 0 0 1 0 0 0 0 ] 1;
  n            n [ 0 0 0 0 0 0 0 ] 1;}
BirdCarreauCoeffs
{
  nu0          nu0 [ 0 2 -1 0 0 0 0 ] 1e-06;
  nuInf        nuInf [ 0 2 -1 0 0 0 0 ] 1e-06;
  k            k [ 0 0 1 0 0 0 0 ] 0;
  n            n [ 0 0 0 0 0 0 0 ] 1;}

```

1. polyMesh directory**blockMeshDict**

```
convertToMeters 0.001;
vertices
(
  ( 0 25.0000 0)// 0
  ( -17.6777 -17.6777 0)// 1.0000
  ( -17.6777 17.6777 0)// 2.0000
  ( 0 -25.0000 0)// 3.0000
  ( 0 41.5000 0)// 4.0000
  ( -29.3449 -29.3449 0)// 5.0000
  ( -29.3449 29.3449 0)// 6.0000
  ( 0 -41.5000 0)// 7.0000
  ( 0 83.0000 0)// 8.0000
  ( -58.6899 -58.6899 0)// 9.0000
  ( -58.6899 58.6899 0)// 10.0000
  ( 0 -83.0000 0)// 11.0000
  ( 0 25.0000 -127.0000)// 12.0000
  ( -17.6777 -17.6777 -127.0000)// 13.0000
  ( -17.6777 17.6777 -127.0000)// 14.0000
  ( 0 -25.0000 -127.0000)// 15.0000
  ( 0 41.5000 -127.0000)// 16.0000
  ( -29.3449 -29.3449 -127.0000)// 17.0000
  ( -29.3449 29.3449 -127.0000)// 18.0000
  ( 0 -41.5000 -127.0000)// 19.0000
  ( 0 60.5000 -127.0000)// 20.0000
  ( -42.7800 -42.7800 -127.0000)// 21.0000
  ( -42.7800 42.7800 -127.0000)// 22.0000
  ( 0 -60.5000 -127.0000)// 23.0000
  ( 0 25.0000 -239.3000)// 24.0000
  ( -17.6777 -17.6777 -239.3000)// 25.0000
  ( -17.6777 17.6777 -239.3000)// 26.0000
  ( 0 -25.0000 -239.3000)// 27.0000
  ( 0 41.5000 -239.3000)// 28.0000
  ( -29.3449 -29.3449 -239.3000)// 29.0000
  ( -29.3449 29.3449 -239.3000)// 30.0000
  ( 0 -41.5000 -239.3000)// 31.0000
  ( 0 60.5000 -239.3000)// 32.0000
  ( -42.7800 -42.7800 -239.3000)// 33.0000
  ( -42.7800 42.7800 -239.3000)// 34.0000
  ( 0 -60.5000 -239.3000)// 35.0000
  ( 0 25.0000 -331.3000)// 36.0000
  ( -17.6777 -17.6777 -331.3000)// 37.0000
  ( -17.6777 17.6777 -331.3000)// 38.0000
  ( 0 -25.0000 -331.3000)// 39.0000
  ( 0 41.5000 -331.3000)// 40.0000
  ( -29.3449 -29.3449 -331.3000)// 41.0000
  ( -29.3449 29.3449 -331.3000)// 42.0000
  ( 0 -41.5000 -331.3000)// 43.0000);
blocks
( hex ( 0 3 1 2 12 15 13 14) (14 7 45) simpleGrading (1 1 1)//1

```

```

hex ( 4 0 2 6 16 12 14 18)(7 7 45) simpleGrading (1 1 1)//2
hex ( 6 2 1 5 18 14 13 17)(7 14 45) simpleGrading (1 1 1)//3
hex ( 3 7 5 1 15 19 17 13)(7 7 45) simpleGrading (1 1 1)//4
hex ( 8 4 6 10 20 16 18 22)(7 7 45) simpleGrading (1 1 1)//5
hex (10 6 5 9 22 18 17 21)(7 14 45) simpleGrading (1 1 1)//6
hex ( 7 11 9 5 19 23 21 17)(7 7 45) simpleGrading (1 1 1)//7
hex (12 15 13 14 24 27 25 26)(14 7 45) simpleGrading (1 1 1)//8
hex (16 12 14 18 28 24 26 30)(7 7 45) simpleGrading (1 1 1)//9
hex (18 14 13 17 30 26 25 29)(7 14 45) simpleGrading (1 1 1)//10
hex (15 19 17 13 27 31 29 25)(7 7 45) simpleGrading (1 1 1)//11
hex (20 16 18 22 32 28 30 34)(7 7 45) simpleGrading (1 1 1)//12
hex (22 18 17 21 34 30 29 33)(7 14 45) simpleGrading (1 1 1)//13
hex (19 23 21 17 31 35 33 29)(7 7 45) simpleGrading (1 1 1)//14
hex (24 27 25 26 36 39 37 38)(14 7 45) simpleGrading (1 1 1)//15
hex (28 24 26 30 40 36 38 42)(7 7 45) simpleGrading (1 1 1)//16
hex (30 26 25 29 42 38 37 41)(7 14 45) simpleGrading (1 1 1)//17
hex (27 31 29 25 39 43 41 37)(7 7 45) simpleGrading (1 1 1)//18);
edges
(
  arc 5 6 ( -41.5000 0 0)
  arc 5 7 ( -15.8814 -38.3410 0)
  arc 6 4 ( -15.8814 38.3410 0)
  arc 10 9 ( -83.0000 0 0)
  arc 9 11 ( -31.7627 -76.6820 0)
  arc 10 8 ( -31.7627 76.6820 0)
  arc 17 18 ( -41.5000 0 -127.0000)
  arc 17 19 ( -15.8814 -38.3410 -127.0000)
  arc 18 16 ( -15.8814 38.3410 -127.0000)
  arc 22 21 ( -60.5000 0 -127.0000)
  arc 21 23 ( -23.1523 -55.8947 -127.0000)
  arc 22 20 ( -23.1523 55.8947 -127.0000)
  arc 29 30 ( -41.5000 0 -239.3000)
  arc 29 31 ( -15.8814 -38.3410 -239.3000)
  arc 30 28 ( -15.8814 38.3410 -239.3000)
  arc 34 33 ( -60.5000 0 -239.3000)
  arc 33 35 ( -23.1523 -55.8947 -239.3000)
  arc 34 32 ( -23.1523 55.8947 -239.3000)
  arc 41 42 ( -41.5000 0 -331.3000)
  arc 41 43 ( -15.8814 -38.3410 -331.3000)
  arc 42 40 ( -15.8814 38.3410 -331.3000));
boundary
(
  Inlet
  {
    type patch;
    faces
    (
      ( 0 3 1 2)
      ( 4 0 2 6)
      ( 6 2 1 5)
      ( 3 7 5 1)
      ( 8 4 6 10)
      (10 6 5 9)
      ( 7 11 9 5) );
  }
  Outlet
  {
    type patch;
    faces
    (
      (36 39 37 38)
      (40 36 38 42)
      (42 38 37 41)
      (39 43 41 37) );
  }
  Wall
  {
    type wall;
    faces
    (
      ( 8 10 22 20)
      ( 9 10 22 21)
      ( 11 9 21 23)
      ( 20 22 34 32)
      ( 21 22 34 33)
      ( 23 21 33 35)
      ( 32 28 30 34)
      ( 34 30 29 33)
      ( 31 35 33 29)
    )
  }
)

```

```

( 28 30 42 40)
( 29 30 42 41)
( 29 31 43 41) );
}
Sym
{
  type symmetryPlane;
  faces
  (( 0 4 16 12)
( 3 0 12 15)
( 7 3 15 19)
( 11 7 19 23)
( 4 8 20 16)
( 12 16 28 24)
( 15 12 24 27)
( 19 15 27 31)
( 23 19 31 35)
( 16 20 32 28)
( 24 28 40 36)
( 27 24 36 39)
( 31 27 39 43) );
}
);
mergePatchPairs
();

```

2. triSurface directory

(Contains all necessary .stl files)

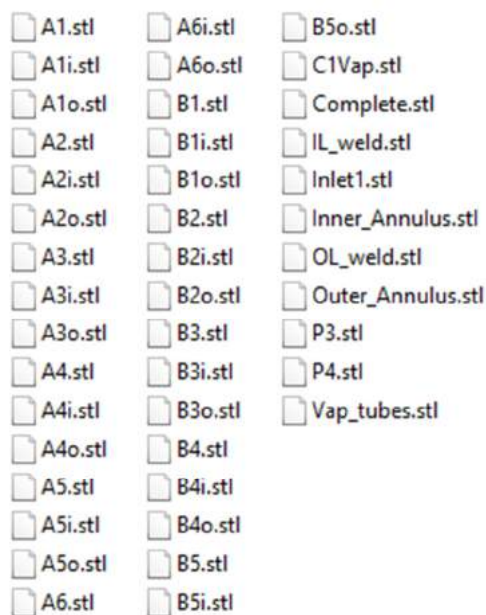


Figure B. 1: All necessary .stl files.

B.1.3. system directory

controlDict

```

libs
( "libOpenFOAM.so");
application pisoFoam;
startFrom latestTime;
startTime 0;
stopAt endTime;

```

```

endTime          12;
deltaT           1e-6;
writeControl     timeStep;
writeInterval    1000;
purgeWrite       0;
writeFormat      ascii;
writePrecision   6;
writeCompression uncompressed;
timeFormat       general;
timePrecision    6;
runTimeModifiable true;

functions
{
    A1 //Similar functions for the mass flow through A2-A6, B1-B5, and
    //C1_and_Vaporizer tubes (Removed due to space limitations)
    {
        type                faceSource;
        functionObjectLibs  ("libfieldFunctionObjects.so");
        enabled              true;
        outputControl        outputTime;
        // Output to log&file (true) or to file only
        log                   true;
        valueOutput          true;
        surfaceFormat        vtk;
        source                sampledSurface;
        sampledSurfaceDict
        {
            type            sampledTriSurfaceMesh;
            surface         A1.stl;
            source          cells;
            interpolate     false;
        }
        operation          areaNormalIntegrate;
        fields
        (
            U
        );
    }

    A1a //Similar functions for the average velocity through A2-A6, B1-B5, and
    //C1_and_Vaporizer tubes (Removed due to space limitations)
    {
        type                faceSource;
        functionObjectLibs  ("libfieldFunctionObjects.so");
        enabled              true;
        outputControl        outputTime;
        // Output to log&file (true) or to file only
        log                   true;
        valueOutput          true;
        surfaceFormat        vtk;
        source                sampledSurface;
        sampledSurfaceDict
        {
            type            sampledTriSurfaceMesh;
            surface         A1.stl;
            source          cells; // sample cells or boundaryFaces
            interpolate     false;
        }
        operation          areaNormalAverage;
        fields
        (
            U
        );
    }

    A1i //Similar functions for the pressure inside A2-A6, B1-B5, and
    //C1_and_Vaporizer tubes (Removed due to space limitations)
    {
        type                faceSource;
        functionObjectLibs  ("libfieldFunctionObjects.so");
        enabled              true;
        outputControl        outputTime;
        // Output to log&file (true) or to file only
        log                   true;
        valueOutput          true;
        surfaceFormat        vtk;
        source                sampledSurface;
        sampledSurfaceDict
        {
            type            sampledTriSurfaceMesh;
            surface         A1i.stl;
            source          cells;
            interpolate     false;
        }
        operation          areaNormalAverage;
    }
}

```

```

        fields
        ( p );
    }
    A10 //Similar functions for the pressure outside A2-A6, B1-B5, and
    //C1_and_Vaporizer tubes (Removed due to space limitations)
    { type                faceSource;
      functionObjectLibs  ("libfieldFunctionObjects.so");
      enabled              true;
      outputControl       outputTime;
      // Output to log&file (true) or to file only
      log                  true;
      valueOutput          true;
      surfaceFormat        vtk;
      source                sampledSurface;
      sampledSurfaceDict
      { type                sampledTriSurfaceMesh;
        surface            A10.stl;
        source              cells;
        interpolate        false; }
      operation            areaNormalAverage;
      fields
      ( p );
    }
    Inner_Annulus //For sampling the average pressure in the inner annulus
    { type                faceSource;
      functionObjectLibs  ("libfieldFunctionObjects.so");
      enabled              true;
      outputControl       outputTime;
      log                  true;
      valueOutput          true;
      surfaceFormat        vtk;
      source                sampledSurface;
      sampledSurfaceDict
      { type                sampledTriSurfaceMesh;
        surface            Inner_Annulus.stl;
        source              cells; // sample cells or boundaryFaces
        interpolate        false; }
      operation            areaNormalAverage;
      fields
      ( p );
    }
    Outer_Annulus //For sampling the average pressure in the outer annulus
    { type                faceSource;
      functionObjectLibs  ("libfieldFunctionObjects.so");
      enabled              true;
      outputControl       outputTime;
      // Output to log&file (true) or to file only
      log                  true;
      valueOutput          true;
      surfaceFormat        vtk;
      source                sampledSurface;
      sampledSurfaceDict
      { type                sampledTriSurfaceMesh;
        surface            Outer_Annulus.stl;
        source              cells; // sample cells or boundaryFaces
        interpolate        false; }
      operation            areaNormalAverage;
      fields
      ( p );
    }
    P3 //Sampling the pressure at the inlet of the combustion chamber (behind the
    diffuser)
    { type                faceSource;
      functionObjectLibs  ("libfieldFunctionObjects.so");
      enabled              true;
      outputControl       outputTime;
      // Output to log&file (true) or to file only
      log                  true;
      valueOutput          true;
      surfaceFormat        vtk;
      source                sampledSurface;

```

```

        sampledSurfaceDict
        {
            type            sampledTriSurfaceMesh;
            surface         P3.stl;
            source          cells;
            interpolate     false;
        }
        operation          areaNormalAverage;
        fields
        (
            p
        );
    }
P4 //Sampling the pressure at the outlet of the combustion chamber
{
    type                  faceSource;
    functionObjectLibs   ("libfieldFunctionObjects.so");
    enabled               true;
    outputControl         outputTime;
    // Output to log&file (true) or to file only
    log                  true;
    valueOutput           true;
    surfaceFormat         vtk;
    source                sampledSurface;
    sampledSurfaceDict
    {
        type            sampledTriSurfaceMesh;
        surface         P4.stl;
        source          cells;
        interpolate     false;
    }
    operation          areaNormalAverage;
    fields
    (
        p
    );
}
};

```

fvSchemes

```

ddtSchemes
{
    default            Euler;
}
gradSchemes
{
    default            Gauss linear;
}
divSchemes
{
    default            none;
    div(phi,U)        Gauss limitedLinearV 1;
    div(phi,k)        Gauss limitedLinear 1;
    div(phi,epsilon)  Gauss limitedLinear 1;
    div(phi,R)        Gauss limitedLinear 1;
    div(R)            Gauss linear;
    div(phi,nuTilda)  Gauss limitedLinear 1;
    div((nuEff*dev(T(grad(U)))) Gauss linear;
}
laplacianSchemes
{
    default            Gauss linear corrected;
}
interpolationSchemes
{
    default            linear;
}
snGradSchemes
{
    default            corrected;
}
fluxRequired
{
    default            no;
    p                  ;
}

```

fvSolution

```

solvers
{
    p
    {
        solver          GAMG;
        tolerance       1e-06;
        relTol          0.05;
        smoother        GaussSeidel;
        cacheAgglomeration true;
        nCellsInCoarsestLevel 10;
        agglomerator    faceAreaPair;
        mergeLevels     1;
    }
    pFinal
    {
        $p;
        tolerance       1e-04;
        relTol          0;
    }
    U
}

```

```

    {
        type            coupled;
        solver          PBiCCCG;
        preconditioner  DILU;
        tolerance       (1e-05 1e-05 1e-05);
        relTol          (0 0 0);
    }
    "(k|epsilon|R|nuTilda)"
    {
        solver          smoothSolver;
        smoother        GaussSeidel;
        tolerance       1e-05;
        relTol          0;
    }
}
PISO
{
    nCorrectors        2;
    nNonOrthogonalCorrectors 0;
    pRefCell           0;
    pRefValue          0;
    residualControl
    {
        p              1e-4;
        U              1e-6;
        "(k|epsilon)"  1e-7;
    }
}
relaxationFactors
{
    fields
    {
        p              0.2;
    }
    equations
    {
        U              0.6;
        k              0.3;
        "epsilon.*"    0.3;
    }
}
snappyHexMeshDict
castellatedMesh true;
snap           true;
addLayers      false;
geometry
{
    Vap_tubes.stl
    {
        type triSurfaceMesh;
        name Vap_tubes;
    }
    Inlet1.stl
    {
        type triSurfaceMesh;
        name Inlet1;
    }
    IL_weld.stl
    {
        type triSurfaceMesh;
        name IL_weld;
    }
    OL_weld.stl
    {
        type triSurfaceMesh;
        name OL_weld;
    }
    Complete.stl
    {
        type triSurfaceMesh;
        name Complete;
    }
};
castellatedMeshControls
{
    maxLocalCells 30000000;
    maxGlobalCells 100000000;
    minRefinementCells 0;
    nCellsBetweenLevels 1;
    features
    (
        { file "Vap_tubes.extendedFeatureEdgeMesh";
          level 6;
        }
        { file "Inlet1.extendedFeatureEdgeMesh";
          level 4;
        }
        { file "IL_weld.extendedFeatureEdgeMesh";
          level 4;
        }
        { file "OL_weld.extendedFeatureEdgeMesh";
          level 6;
        }
        { file "Complete.extendedFeatureEdgeMesh";
          level 4;
        }
    );
    refinementSurfaces

```

```

    { Vap_tubes
      { level (3 3);          }
      Inlet1
      { level (2 2);          }
      IL_weld
      { level (2 2);          }
      OL_weld
      { level (3 3);          }
      Complete
      { level (2 2);          }
    }
    resolveFeatureAngle 30;
    locationInMesh (-0.001 -0.001 -0.001); // Inside point
    allowFreeStandingZoneFaces true;
  }
  snapControls
  { nSmoothPatch 3;
    tolerance 1.0;
    nSolveIter 300;
    nRelaxIter 5;
      nFeatureSnapIter 10;
      implicitFeatureSnap false;
      explicitFeatureSnap true;
      multiRegionFeatureSnap true;
  }
  addLayersControls
  { relativeSizes true;
    { "Vap_tubes_.*"
      { nSurfaceLayers 3;          }
      "Inlet1_.*"
      { nSurfaceLayers 3;          }
      "IL_weld_.*"
      { nSurfaceLayers 3;          }
      "OL_weld_.*"
      { nSurfaceLayers 3;          }
      "Complete_.*"
      { nSurfaceLayers 3;          }
    }
    expansionRatio 1.0;
    finalLayerThickness 0.3;
    minThickness 0.25;
    nGrow 0;
    featureAngle 30;
    nRelaxIter 5;
    nSmoothSurfaceNormals 1;
    nSmoothNormals 3;
    nSmoothThickness 10;
    maxFaceThicknessRatio 0.5;
    maxThicknessToMedialRatio 0.3;
    minMedianAxisAngle 90;
    nBufferCellsNoExtrude 0;
    nLayerIter 50;
    nRelaxedIter 20;
  }
  meshQualityControls
  { #include "meshQualityDict"
    relaxed
    { maxNonOrtho 75;          }
    nSmoothScale 4;
    errorReduction 0.75;
  }
  writeFlags
  ( scalarLevels // write volScalarField with cellLevel for postprocessing
    layerSets // write cellSets, faceSets of faces in layer
    layerFields // write volScalarField for layer coverage
  );
  mergeTolerance 1E-6;

```

surfaceFeatureExtractDict

Vap_tubes.stl

```

{ extractionMethod extractFromSurface;
  extractFromSurfaceCoeffs
  { includedAngle 150; }
  writeObj yes;
}
Inlet1.stl
{ extractionMethod extractFromSurface;
  extractFromSurfaceCoeffs
  { includedAngle 150; }
  writeObj yes;
}
IL_weld.stl
{ extractionMethod extractFromSurface;
  extractFromSurfaceCoeffs
  { includedAngle 150; }
  writeObj yes;
}
OL_weld.stl
{ extractionMethod extractFromSurface;
  extractFromSurfaceCoeffs
  { includedAngle 150; }
  writeObj yes;
}
Complete.stl
{ extractionMethod extractFromSurface;
  extractFromSurfaceCoeffs
  { includedAngle 150; }
  writeObj yes;
}

```

B.2. Case Files for the Swirling Flow Case

All files in the swirling flow case are the same as for the axial case, excluding the `blockMeshDict` file. A `createPatchDict` file is added to the system directory as well. Once `createPatch` is run in the terminal, another timestep directory is written. The files describing the boundary and initial conditions are changed to include the new patches. Only the “epsilon” file will be shown, because the “k”, “nut”, “nuTilda”, “p” and “U” files all have the same “Sym” boundary removed and the same cyclic patches added in the next timestep directory.

blockMeshDict

```

convertToMeters 0.001;
vertices
( ( 0 0 0.0000)//11
( 0 25.0000 0.0000)//12
( -25.0000 25.0000 0.0000)//13
( -25.0000 0 0.0000)//14
( -25.0000 -25.0000 0.0000)//15
( 0 -25.0000 0.0000)//16
( 0 41.5000 0.0000)//17
( -29.3449 29.3449 0.0000)//18
( -41.5000 0 0.0000)//19
( -29.3449 -29.3449 0.0000)//20
( 0 -41.5000 0.0000)
( 0 83.0000 0.0000)
( -58.6899 58.6899 0.0000)
( -83.0000 0 0.0000)
( -58.6899 -58.6899 0.0000)
( 0 -83.0000 0.0000)
( 0 0 -127.0000)
( 0 25.0000 -127.0000)
( -25.0000 25.0000 -127.0000)
( -25.0000 0 -127.0000)
( -25.0000 -25.0000 -127.0000)
( 0 -25.0000 -127.0000)

```

```

(      0      41.5000 -127.0000)
( -29.3449  29.3449 -127.0000)
( -41.5000      0 -127.0000)
( -29.3449 -29.3449 -127.0000)
(      0 -41.5000 -127.0000)
(      0      60.5000 -127.0000)
( -42.7799  42.7799 -127.0000)
( -60.5000      0 -127.0000)
( -42.7799 -42.7799 -127.0000)
(      0 -60.5000 -127.0000)
(      0      0 -239.3000)
(      0      25.0000 -239.3000)
( -25.0000  25.0000 -239.3000)
( -25.0000      0 -239.3000)
( -25.0000 -25.0000 -239.3000)
(      0 -25.0000 -239.3000)
(      0      41.5000 -239.3000)
( -29.3449  29.3449 -239.3000)
( -41.5000      0 -239.3000)
( -29.3449 -29.3449 -239.3000)
(      0 -41.5000 -239.3000)
(      0      60.5000 -239.3000)
( -42.7799  42.7799 -239.3000)
( -60.5000      0 -239.3000)
( -42.7799 -42.7799 -239.3000)
(      0 -60.5000 -239.3000)
(      0      0 -331.3000)
(      0      25.0000 -331.3000)
( -25.0000  25.0000 -331.3000)
( -25.0000      0 -331.3000)
( -25.0000 -25.0000 -331.3000)
(      0 -25.0000 -331.3000)
(      0      41.5000 -331.3000)
( -29.3449  29.3449 -331.3000)
( -41.5000      0 -331.3000)
( -29.3449 -29.3449 -331.3000)
(      0 -41.5000 -331.3000));
blocks
(hex ( 1 0 3 2 17 16 19 18 )(14 14 45) simpleGrading (1 1 1)
hex ( 0 5 4 3 16 21 20 19 )(14 14 45) simpleGrading (1 1 1)
hex ( 6 1 2 7 22 17 18 23 )(14 14 45) simpleGrading (1 1 1)
hex ( 2 3 8 7 18 19 24 23 )(14 14 45) simpleGrading (1 1 1)
hex ( 3 4 9 8 19 20 25 24 )(14 14 45) simpleGrading (1 1 1)
hex ( 5 10 9 4 21 26 25 20 )(14 14 45) simpleGrading (1 1 1)
hex ( 11 6 7 12 27 22 23 28 )(14 14 45) simpleGrading (1 1 1)
hex ( 7 8 13 12 23 24 29 28 )(14 14 45) simpleGrading (1 1 1)
hex ( 8 9 14 13 24 25 30 29 )(14 14 45) simpleGrading (1 1 1)
hex ( 10 15 14 9 26 31 30 25 )(14 14 45) simpleGrading (1 1 1)
hex ( 17 16 19 18 33 32 35 34 )(14 14 45) simpleGrading (1 1 1)
hex ( 16 21 20 19 32 37 36 35 )(14 14 45) simpleGrading (1 1 1)
hex ( 22 17 18 23 38 33 34 39 )(14 14 45) simpleGrading (1 1 1)
hex ( 18 19 24 23 34 35 40 39 )(14 14 45) simpleGrading (1 1 1)
hex ( 19 20 25 24 35 36 41 40 )(14 14 45) simpleGrading (1 1 1)
hex ( 21 26 25 20 37 42 41 36 )(14 14 45) simpleGrading (1 1 1)
hex ( 27 22 23 28 43 38 39 44 )(14 14 45) simpleGrading (1 1 1)
hex ( 23 24 29 28 39 40 45 44 )(14 14 45) simpleGrading (1 1 1)
hex ( 24 25 30 29 40 41 46 45 )(14 14 45) simpleGrading (1 1 1)
hex ( 26 31 30 25 42 47 46 41 )(14 14 45) simpleGrading (1 1 1)
hex ( 33 32 35 34 49 48 51 50 )(14 14 45) simpleGrading (1 1 1)
hex ( 32 37 36 35 48 53 52 51 )(14 14 45) simpleGrading (1 1 1)
hex ( 38 33 34 39 54 49 50 55 )(14 14 45) simpleGrading (1 1 1)
hex ( 34 35 40 39 50 51 56 55 )(14 14 45) simpleGrading (1 1 1)
hex ( 35 36 41 40 51 52 57 56 )(14 14 45) simpleGrading (1 1 1)
hex ( 37 42 41 36 53 58 57 52 )(14 14 45) simpleGrading (1 1 1));
edges
( arc 11 12 ( -31.7627  76.6820  0.0000)
  arc 13 12 ( -76.6820  31.7627  0.0000)
  arc 13 14 ( -76.6820 -31.7627  0.0000)
  arc 14 15 ( -31.7627 -76.6820  0.0000)
  arc 6 7 ( -15.8814  38.3410  0.0000)
  arc 7 8 ( -38.3410  15.8814  0.0000)

```

```

arc 8 9 ( -38.3410 -15.8814 0.0000)
arc 9 10 ( -15.8814 -38.3410 0.0000)
arc 27 28 ( -23.1523 55.8947 -127.0000)
arc 29 28 ( -55.8947 23.1523 -127.0000)
arc 29 30 ( -55.8947 -23.1523 -127.0000)
arc 30 31 ( -23.1523 -55.8947 -127.0000)
arc 22 23 ( -15.8814 38.3410 -127.0000)
arc 23 24 ( -38.3410 15.8814 -127.0000)
arc 24 25 ( -38.3410 -15.8814 -127.0000)
arc 25 26 ( -15.8814 -38.3410 -127.0000)
arc 43 44 ( -23.1523 55.8947 -239.3000)
arc 45 44 ( -55.8947 23.1523 -239.3000)
arc 45 46 ( -55.8947 -23.1523 -239.3000)
arc 46 47 ( -23.1523 -55.8947 -239.3000)
arc 38 39 ( -15.8814 38.3410 -239.3000)
arc 40 39 ( -38.3410 15.8814 -239.3000)
arc 40 41 ( -38.3410 -15.8814 -239.3000)
arc 41 42 ( -15.8814 -38.3410 -239.3000)
arc 54 55 ( -15.8814 38.3410 -331.3000)
arc 56 55 ( -38.3410 15.8814 -331.3000)
arc 56 57 ( -38.3410 -15.8814 -331.3000)
arc 57 58 ( -15.8814 -38.3410 -331.3000 );
boundary
( Inlet
  { type patch;
    faces
      ( ( 1 0 3 2)
        ( 0 5 4 3)
        ( 6 1 2 7)
        ( 2 3 8 7)
        ( 3 4 9 8)
        ( 5 10 9 4)
        ( 11 6 7 12)
        ( 7 8 13 12)
        ( 8 9 14 13)
        ( 10 15 14 9));
    }
  Outlet
  { type patch;
    faces
      ( (49 48 51 50 )
        (48 53 52 51 )
        (54 49 50 55 )
        (50 51 56 55 )
        (51 52 57 56 )
        (53 58 57 52 ) );
    }
  Wall
  { type wall;
    faces
      (( 12 11 27 28)
        ( 29 13 12 28)
        ( 30 14 13 29)
        ( 14 15 31 30)
        ( 28 27 43 44)
        ( 45 29 28 44)
        ( 46 30 29 45)
        ( 30 31 47 46)
        ( 39 38 54 55)
        ( 39 40 56 55)
        ( 40 41 57 56)
        ( 41 42 58 57)
        ( 43 38 39 44)
        ( 39 40 45 44)
        ( 40 41 46 45)
        ( 42 47 46 41) );
    }
  cycl
  { type patch;
    faces
      ( ( 6 22 27 11)

```

```

( 1 17 22 6)
( 0 16 17 1)
( 22 38 43 27)
( 17 33 38 22)
( 16 32 33 17)
( 33 49 54 38)
( 32 48 49 33)      );
}
cyc2
{ type          patch;
  faces
  (( 15 31 26 10)
( 10 26 21 5)
( 5 21 16 0)
( 31 47 42 26)
( 26 42 37 21)
( 21 37 32 16)
( 42 58 53 37)
( 37 53 48 32)      );
}
);
mergePatchPairs
();

```

createPatchDict

```

pointSync false;
patches
( { name cyc_half0;
  patchInfo
  { type cyclic;
    neighbourPatch cyc_half1;
    transform rotational;
    rotationAxis (0 0 1);
    rotationCentre (0 0 0);
    matchTolerance 0.001;      }
  constructFrom patches;
  patches (cyc1);      }
{ name cyc_half1;
  patchInfo
  { type cyclic;
    neighbourPatch cyc_half0;
    transform rotational;
    rotationAxis (0 0 1);
    rotationCentre (0 0 0);
    matchTolerance 0.001;      }
  constructFrom patches;
  patches (cyc2);      }
);

```

epsilon

```

dimensions      [ 0 2 -3 0 0 0 0 ];
internalField   uniform 26.663e-6;
boundaryField
{ Inlet
  { type          turbulentMixingLengthDissipationRateInlet;
    mixingLength  0.00575;
    value         $internalField;      }
  Outlet
  { type          inletOutlet;
    inletValue    $internalField;      }
  Wall
  { type          epsilonWallFunction;
    value         $internalField;      }
  Sym
  { type          symmetryPlane;      }
  Inlet1
  { type          epsilonWallFunction;
    value         $internalField;      }
  OL_weld
  { type          epsilonWallFunction;

```

```
    value          $internalField;  }
IL_weld
{  type          epsilonWallFunction;
  value          $internalField;  }
Vap_tubes
{  type          epsilonWallFunction;
  value          $internalField;  }
Complete
{  type          epsilonWallFunction;
  value          $internalField;  }
cyc_half0
{  type          cyclic;  }
cyc_half1
{  type          cyclic;  }
}
```

APPENDIX C: DETAILED TUTORIAL ON HOW THE MESH WAS CREATED

The mesh was made by creating a blockMesh of the outer domain structure and then using .stl files created in Autodesk Inventor 2014 and snappyHexMesh to mesh the finer details.

The mesh was created by dividing the circular structure into seven sections, in order to create a circular mesh with hexahedral cells. A larger outer circular structure was added, in order to simplify creating the lateral face before the exhaust section. Figure C. 1 shows the basic shape of the circular structure.

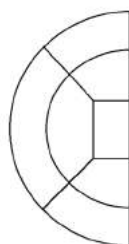


Figure C. 1: Shape required for circular hexahedral mesh.

The structure shown in Figure C. 1 was used at every face where the computational domain's radius changed. This includes the inlet of the adapter nozzle, the inlet of the combustor housing section, the outlet of the combustor housing section and the inlet of the exhaust section and lastly, the outlet of the exhaust section as well. The vertices necessary were numbered as follows in Figure C. 2. These numbers correspond to the blockMeshDict file found in section B.1.2. in Appendix B.

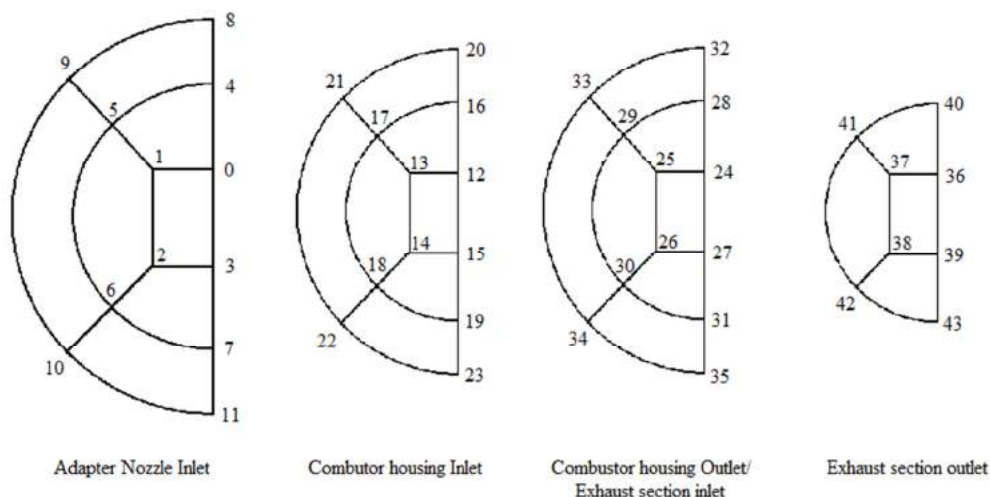


Figure C. 2: Numbered vertices of blockMesh.

The hexes were then defined as specified in OpenFOAM (2013: 15) and can be seen in the blockMeshDict file in section B.1.2. The arcs were then defined. The boundaries were specified as seen in Figure C. 3 in the blockMeshDict file

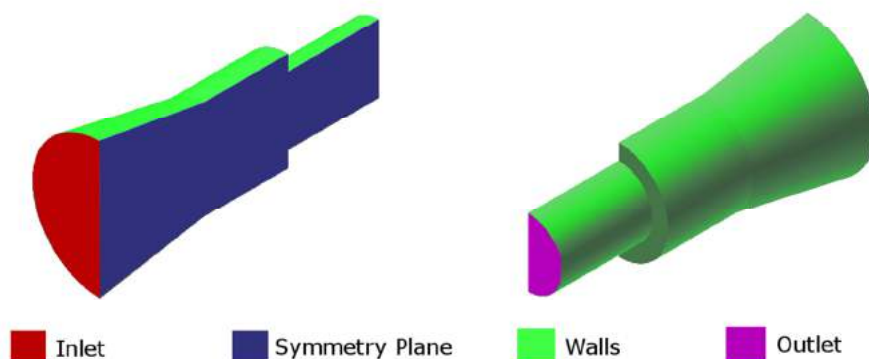


Figure C. 3: Boundary patches as defined in blockMeshDict.

Once the blockMeshDict file was set up blockMesh was run from the terminal. Afterwards, checkMesh was run to ensure that the mesh was of a high standard.

The snappyHexMesh file was then set up. The geometries to be snapped were specified as tri-surface meshes and were all contained in the constant/triSurface directory. The maximum number of local and global cells were set very large, in order to ensure that the surfaces were meshed accurately without being restricted by number of cells. When these figures were set to lower values it was found that the finer details of the geometry would not be meshed, especially the smaller holes in the combustion chamber's inner and outer liners.

For the features sub-dictionary in the snappyHexMeshDict file, the level for any cell intersected by its edges was set to level 6 for the vaporizer tubes and outer liner and level 4 for the other specified geometries. The level for the vaporizer tubes and outer liner were set higher, due to the rigid edges in those geometries. It was also found that if these levels were set any higher, the meshing process would become rather time consuming.

The refinement level for all surfaces was then specified. In the refinementSurfaces sub-dictionary a maximum and a minimum refinement level is specified. Every cell intersecting a surface would be refined up to the minimum value; a cell intersected multiple times would be refined up to the maximum level. It was specified that all surfaces had the same maximum and minimum refinement. It was found that changing these values did not noticeably improve the mesh, but increased meshing time. The refinement level specified for most surfaces was level 2, while level 3 was specified for the vaporizer tubes and the inner and outer liner, since these surfaces had sections where the y^+ value is of interest.

The "location in mesh" point was determined to be (-0.001 -0.001 -0.001). This point was chosen, because it fell inside the computational domain, but not within

the locations of the inner structures. This meant that the mesh would be snapped around the geometry. If a point inside the geometry was specified, the geometry would be meshed.

It was specified in the snappyHexMeshDict file that at least three layers should be added to the mesh forming from the wall. This was done, because it was found that the layer formation does not impact this complex mesh noticeably, but increased the meshing time. It was found that refining the mesh in the blockMesh file was much more effective than trying to add layers through the layers sub-dictionary in snappyHexMeshDict. An expansion ratio of 1 was chosen. The final layer thickness and minimum thickness setting is a relative height. It was also found that in this complex mesh these settings were not very effective.

The controls of snappyHexMesh are summarized by Jackson (2012).

REFERENCES

- JACKSON, A., 2012.** *A Comprehensive Tour of snappyHexMesh*. [Online].
openfoamwiki.net/images/f/f0/Final-AndrewJacksonSlidesOFW7.pdf.
[Accessed 14th of August 2015].

APPENDIX D: RESULTS

D.1. Experimental Results

The mass flow distribution determined experimentally for each inlet velocity for the axial flow case is presented in Table D. 1.

Table D. 1: Experimental mass flow distribution for each of the axial cases.

Case	Ax1	Ax2	Ax3	Ax4	Ax5	Ax6	Ax7
	Mass flow distribution [%]						
A1	3.0874	2.7996	2.9138	2.8032	2.9939	2.9710	3.0753
A2	3.4415	3.2536	3.2048	3.2898	3.3198	3.2450	3.3929
A3	3.0930	2.8769	3.0015	2.9810	3.1221	3.1965	3.1775
A4	13.929	13.843	13.836	13.990	14.105	14.088	14.107
A5	18.422	18.272	18.328	18.169	18.260	18.418	18.420
A6	6.7739	6.6897	6.7605	6.7702	6.9763	7.0358	7.0092
B1	1.7270	1.6992	1.6449	1.8584	1.9927	1.7645	1.7468
B2	3.3498	3.3633	3.3492	3.3218	3.6505	3.5640	3.6595
B3	3.6528	3.7880	3.6507	3.6845	3.9879	3.8649	3.8910
B4	7.2213	7.0023	7.0425	6.9208	7.1501	7.1582	7.1914
B5	19.104	18.956	19.024	19.001	19.195	19.261	19.228
C1 and Vaporizer Tubes	19.689	19.476	19.663	19.682	19.908	19.869	19.928

The mass flow distribution determined experimentally for each inlet velocity for the R9 flow case is presented in Table D. 2.

Table D. 2: Experimental mass flow distribution for each of the R9 cases.

Case	R9.1	R9.2	R9.3	R9.4	R9.5	R9.6	R9.7
	Mass flow distribution [%]						
A1	2.8528	2.6580	2.6502	2.7130	2.7356	2.6992	2.7617
A2	3.0238	2.8985	2.8414	3.0590	3.0957	3.0259	3.1855
A3	2.9839	2.9943	2.9052	2.9605	2.9835	3.0060	3.1155
A4	13.871	13.572	13.555	13.582	13.687	13.806	13.775
A5	18.488	17.850	18.081	18.186	18.106	18.072	18.146
A6	6.8730	6.5741	6.6195	6.5506	6.6736	6.7614	6.6750
B1	2.2040	2.0238	2.0032	1.9415	2.0239	2.0006	1.9269
B2	4.1035	3.9067	3.8462	3.9258	3.9480	4.0312	3.9386
B3	4.2462	4.2007	4.1879	4.1549	4.0678	3.9900	4.1232
B4	7.1471	6.9794	7.0045	6.9502	7.1278	7.1672	7.1948
B5	18.840	18.854	18.800	18.672	18.888	18.968	18.926
C1 and Vaporizer Tubes	20.653	20.307	20.968	20.495	20.428	20.518	20.285

The mass flow distribution determined experimentally for each inlet velocity for the R7 flow case is presented in Table D. 3.

Table D. 3: Experimental mass flow distribution for each of the R7 cases.

Case	R7.1	R7.2	R7.3	R7.4	R7.5	R7.6	R7.7
	Mass flow distribution [%]						
A1	3.1246	2.8583	3.0430	3.1320	3.1328	3.0634	3.0968
A2	3.1940	3.1404	3.1795	3.2915	3.3066	3.3653	3.3440
A3	3.2308	3.1511	3.2263	3.3550	3.3745	3.4317	3.3608
A4	13.778	13.863	13.858	13.921	14.004	13.987	13.842
A5	18.613	18.464	18.582	18.658	18.601	18.665	18.618
A6	6.7682	6.7043	6.7858	6.8506	6.9098	6.9792	6.8586
B1	1.5993	1.4793	1.4581	1.5672	1.6644	1.7445	1.7271
B2	3.4252	3.4590	3.4078	3.5155	3.6766	3.6830	3.6077
B3	3.6165	3.5067	3.4994	3.5795	3.6614	3.7393	3.7160
B4	7.3039	7.1101	7.1152	7.1809	7.3222	7.3454	7.3101
B5	19.188	19.040	19.261	19.369	19.279	19.344	19.272
C1 and Vaporizer Tubes	20.546	20.608	20.772	20.813	20.887	20.782	20.871

D.2. Numerical Results

The mass flow distribution determined numerically for each inlet velocity for the axial flow case is presented in Table D. 4.

Table D. 4: Numerical mass flow distribution for each of the axial cases.

Case	Ax1	Ax2	Ax3	Ax4	Ax5	Ax6	Ax7
	Mass flow distribution [%]						
A1	2.5409	2.5299	2.5290	2.5140	2.5177	2.5057	2.4773
A2	2.5129	2.4959	2.4925	2.4821	2.4735	2.4853	2.4525
A3	2.4547	2.4411	2.4337	2.4271	2.4194	2.4150	2.3943
A4	11.574	11.5620	11.560	11.543	11.554	11.576	11.476
A5	20.608	20.662	20.620	20.591	20.706	20.562	20.489
A6	5.3764	5.3176	5.3344	5.3199	5.2986	5.2543	5.2255
B1	0.5606	0.5823	0.5673	0.5527	0.5409	0.5520	0.5055
B2	2.7545	2.8121	2.8494	2.7736	2.7724	2.8495	2.7230
B3	2.9176	2.8728	2.9146	2.8569	2.8482	2.8764	2.8168
B4	8.0052	7.9895	8.0438	7.9936	8.0334	8.0051	7.9068
B5	24.974	24.877	24.758	25.036	24.867	24.846	25.499
C1 and Vaporizer Tubes	15.718	15.856	15.895	15.907	15.966	16.071	16.032

The mass flow distribution determined numerically for each inlet velocity for the R9 flow case is presented in Table D. 5.

Table D. 5: Numerical mass flow distribution for each of the R9 cases.

Case	R9.1	R9.2	R9.3	R9.4	R9.5	R9.6	R9.7
	Mass flow distribution [%]						
A1	2.6095	2.6038	2.6027	2.5993	2.6006	2.6006	2.5989
A2	2.5406	2.5329	2.5307	2.5234	2.5238	2.5228	2.5193
A3	2.4478	2.4416	2.4389	2.4338	2.4325	2.4335	2.4304
A4	12.061	12.066	12.079	12.083	12.095	12.105	12.101
A5	21.275	21.298	21.283	21.286	21.295	21.286	21.306
A6	5.5445	5.5316	5.5232	5.5011	5.5013	5.5006	5.4792
B1	0.4883	0.4844	0.4721	0.4664	0.4699	0.4665	0.4563
B2	2.7256	2.7062	2.6935	2.6423	2.6547	2.6233	2.6227
B3	2.9828	2.9760	2.9691	2.9539	2.9616	2.9593	2.9501
B4	8.3306	8.3508	8.3520	8.3709	8.3741	8.3847	8.3953
B5	24.481	24.442	24.435	24.473	24.416	24.390	24.389
C1 and Vaporizer Tubes	14.511	14.564	14.619	14.665	14.673	14.726	14.749

The mass flow distribution determined numerically for each inlet velocity for the R7 flow case is presented in Table D. 6.

Table D. 6: Numerical mass flow distribution for each of the R7 cases.

Case	R7.1	R7.2	R7.3	R7.4	R7.5	R7.6	R7.7
	Mass flow distribution [%]						
A1	2.6274	2.6026	2.6238	2.6058	2.6043	2.6033	2.5995
A2	2.5394	2.5222	2.5238	2.5243	2.5199	2.5209	2.5175
A3	2.4540	2.4325	2.4487	2.4310	2.4319	2.4305	2.4298
A4	12.165	12.160	12.181	12.155	12.159	12.179	12.166
A5	21.425	21.480	21.573	21.446	21.460	21.466	21.475
A6	5.4894	5.4417	5.4519	5.5105	5.5166	5.4994	5.5021
B1	0.5220	0.4714	0.4870	0.4660	0.4698	0.4536	0.4465
B2	2.3858	2.5985	2.5876	2.4505	2.3875	2.3531	2.3139
B3	2.8541	2.9120	2.9410	2.8341	2.8082	2.8065	2.7654
B4	8.3210	8.3861	8.3370	8.3156	8.3022	8.3078	8.2992
B5	24.591	24.323	24.208	24.494	24.579	24.572	24.624
C1 and Vaporizer Tubes	14.623	14.668	14.634	14.765	14.759	14.806	14.858

The recirculation zone and impinging jets of the swirling flow case R9.7 are presented in Figure D. 1.

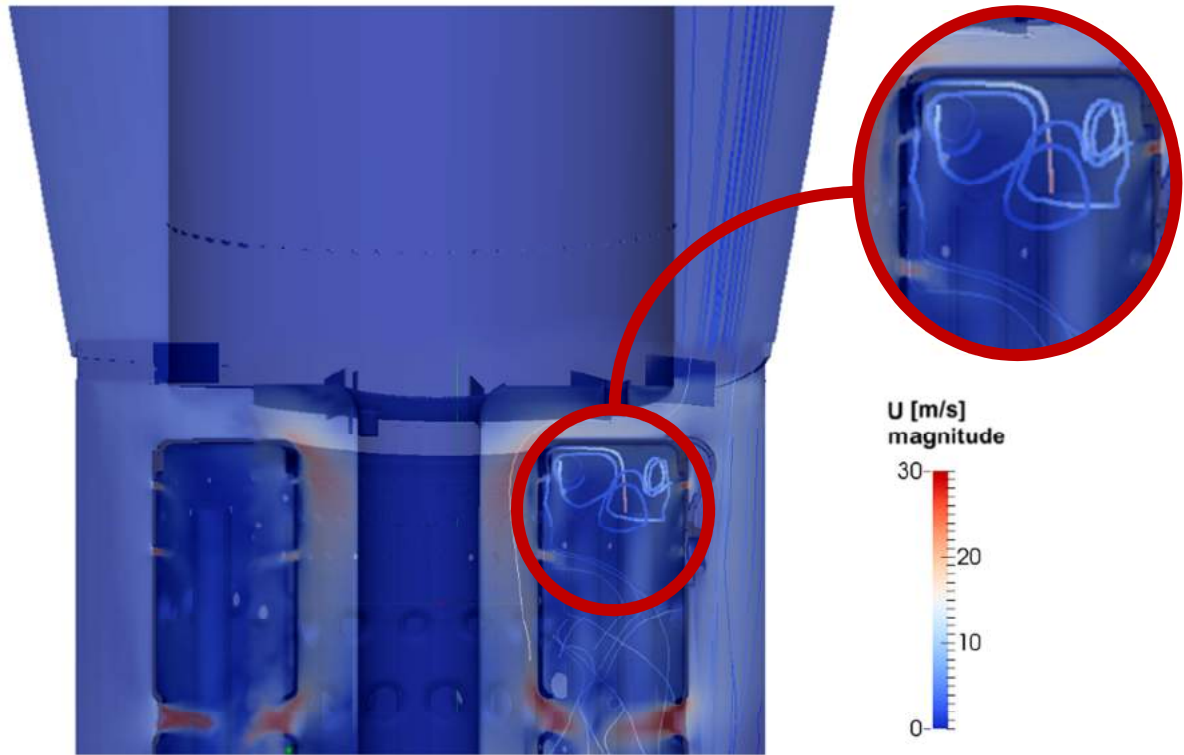


Figure D. 1: Recirculation zone of the R9.7 case.

APPENDIX E: CALIBRATION PROCEDURES

E.1. Pressure Transducers

The pressure transducers used were the Endress&Hauser Deltabar M PMD55 and the Endress&Hauser Cerabar M PMC51. According to the manufacturer, the uncertainty associated with these pressure transducers are as shown in Table E. 1.

Table E. 1: Uncertainty of the Pressure Transducers.

Pressure Transducer	Uncertainty [%]	Uncertainty [Pa]
Deltabar M PMD55	0.16 %	± 5 Pa
Cerabar M PMC51	0.033 %	± 10 Pa

The pressure transducers were calibrated using a Betz manometer. Plastic tubing was connected to the pressure transducer and the Betz manometer by using a t-section. The third leg of the t-section was used to increase the pressure. The strain experienced by the pressure transducer in question was then captured with an Agilent 34970A Data Acquisition Unit.

Care was taken to ensure that the Betz manometer was completely level and that it displayed 0 Pa at atmospheric conditions. Figure E. 1. and Figure E. 2 show the calibration curves obtained for the pressure transducers.

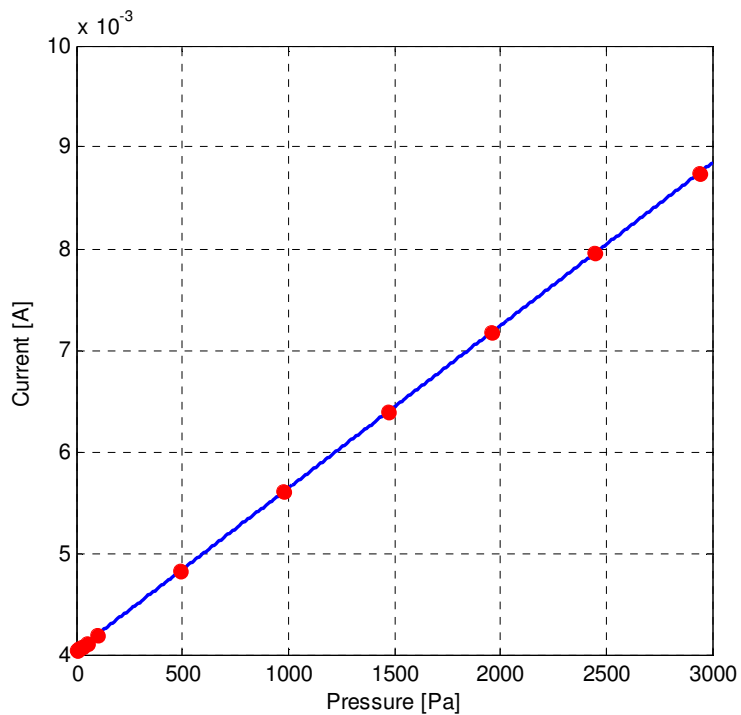


Figure E. 1: Calibration curve for Cerabar pressure transducer.

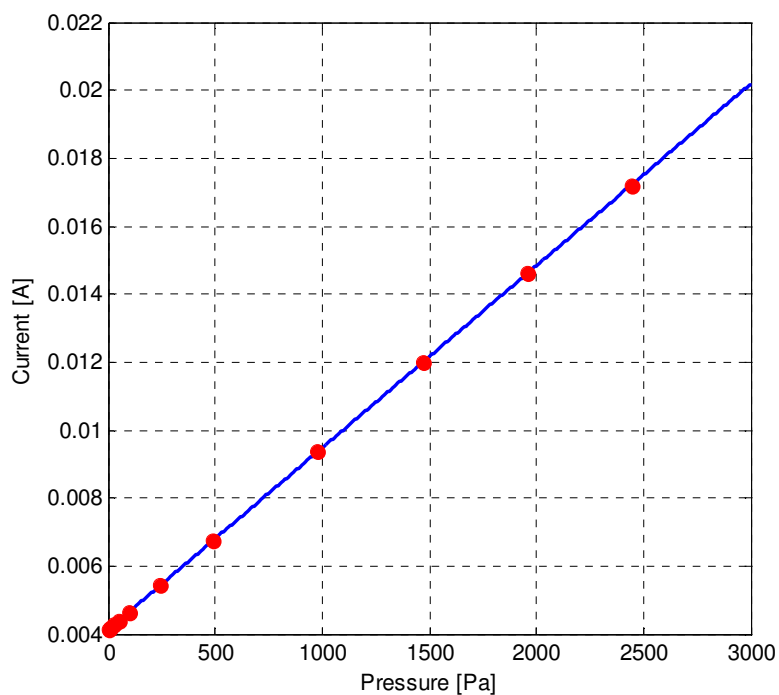


Figure E. 2: Calibration curve for Deltabar pressure transducer.

It can be seen that the calibration indicates that the relationship between the measured strain and the pressure is linear. At lower pressures some deviation was experienced. A smaller orifice plate (ensuring that large pressures were measured) was then designed and manufactured in order to reduce error in the pressure measurements.

E.2. Thermocouples

An Isotech 4 W model platinum resistance thermometer (Calibrated on 4 Feb 2013: Certificate RAP15738) was used along with a Hewlett Packard 34401A multimeter to calibrate the thermocouples. A custom aluminium billit that could hold eight thermocouples at once, with the platinum resistance thermometer in the center was slotted into a Fluke Metrology Well, so that the temperature of the platinum resistance thermometer and thermocouples could be controlled and kept the same.

The temperature measured by the platinum resistance thermometer was then compared to the temperature measured by the thermocouples as shown in Figure E. 3.

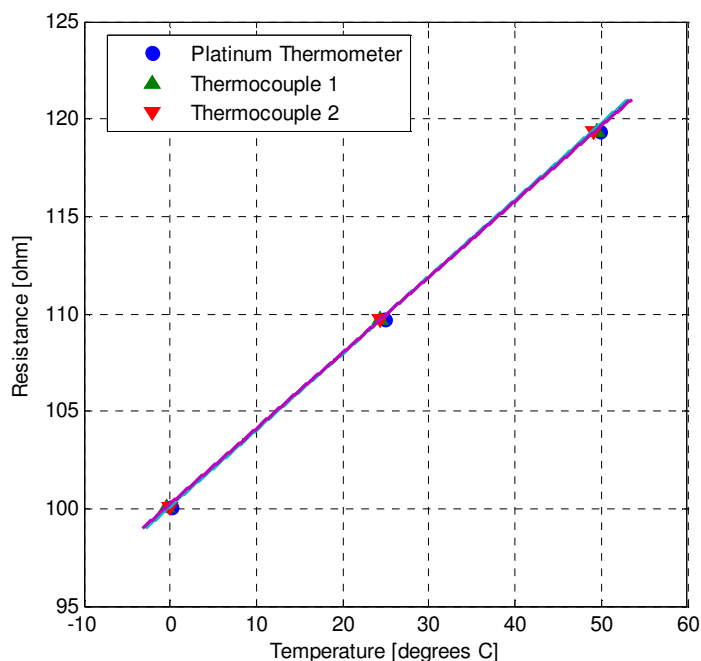


Figure E. 3: Comparison of thermocouple measurements to the platinum thermometer measurements.

From Figure E. 3 it can be seen that the measurements taken by the platinum thermometer are almost exactly the measurements taken with the thermocouples. The largest error obtained between the measurements was 0.73 % for Thermocouple 2. It was then deemed that no adjustments needed to be made for the thermocouples and that they measured accurately.

E.3. Orifice Plate

The smaller orifice plate was designed to operate between $0.001 \text{ kg/s} < \dot{m} < 0.045 \text{ kg/s}$. The minimum value in the range was determined by the minimum flow estimated through the leakages at the lowest pressure drop over the entire system. The maximum was determined by the flow through the combustion chamber. The orifice plate was also designed with the minimum and maximum ranges of the pressure transducers in mind.

According to ISO (2003: 13-14) the following should be considered when calculating the relative uncertainty of an orifice plate:

Uncertainty for the discharge coefficient:

$$= 0.5 \% \quad \text{For } \beta = 0.2169 \quad (\text{E.1})$$

The uncertainty introduced by the expansibility factor is described as follows:

$$= 3.5 \frac{\Delta p}{\kappa p_1} \% \quad (\text{E.2})$$

In equation 2 Δp is the differential pressure measured over the orifice plate, κ is the specific heat ratio of air and p_1 is the static pressure upstream of the orifice plate.

The experimental method required that mass flows be measured for the “forward” case and the “inverse” case for each set of holes resulting in a large dataset. Therefore the calculated uncertainties were only determined for the Ax4 “forward” case and are shown in Table E. 2.

Table E. 2: Uncertainties for the small orifice plate.

Set of holes	Mass Flow [kg/s]	Uncertainty [kg/s]	Uncertainty [%]
Primary Case	0.0308	0.0008085	2.6247
A1	0.0014	0.0000089	0.6317
A2	0.0015	0.0000096	0.6360
A3	0.0014	0.0000088	0.6302
A4	0.0060	0.0000599	0.9925
A5	0.0078	0.0000909	1.1682
A6	0.0031	0.0000225	0.7373
B1	0.0007	0.0000045	0.5954
B2	0.0016	0.0000102	0.6411
B3	0.0018	0.0000118	0.6535
B4	0.0034	0.0000262	0.7660
B5	0.0085	0.0001065	1.2470
Vaporizer tubes and cooling holes	0.0082	0.0000996	1.2127

APPENDIX F: LEAKAGE INVESTIGATION

A leakage investigation was performed, in order to minimise the effect of the leakages on the results.

The leakages were determined by first measuring the mass flow through the combustor with all of the sets of holes open and determining the pressure drop over the entire system. All the sets of holes of the combustor were then blocked and the pressure drop over the entire system was increased to the value determined previously (Thus applying the “forward”-method, but with all the sets of holes blocked). Therefore, there were no outlets open. The mass flow rate determined for this case was the mass flow rate of the leakages.

Originally the leakage mass flow rate was determined to be around 24 %. Steps were then taken to reduce the leakages.

- The combustor exhaust was sealed to the exhaust of the test section with epoxy.
- The adapter nozzle flange was sealed to the test section using window sealant.
- Gaskets were used between flanges that needed to be disassembled regularly.



Figure F. 1: Measures taken to reduce leakages (a) Epoxy seal inside combustor (b) Epoxy seal on the outside of the combustor (c) Window sealant used to seal flanges (d) Gaskets used where frequent disassembly is necessary.

Figure F. 1. shows the leakage reduction measures taken. After these measures were taken, the leakages were reduced to around 8 %, as shown in Table F. 1.

Table F. 1. Reduced leakages.

Case	Leakages before adjustments [%]	Leakages after adjustments [%]
Ax1	24.0291	8.7559
Ax2	24.1007	8.7969
Ax3	24.1659	8.8320
Ax4	24.2204	8.7628
Ax5	24.4244	8.8212
Ax6	24.4025	8.7773
Ax7	24.4630	8.8135

The leakages were determined for multiple test cases (Ax1-Ax7, R7.1-R7.7, and R9.1-R9.7) and were also determined during the repeatability tests and are summarized in Table F. 2.

Table F. 2: Leakages repeatability.

Case	Leakages [%]					
	Ax1-Ax7	R7.1-R7.7	R9.1-R9.7	Ax1-Ax7 Repeatability	R7.1-R7.7 Repeatability	R9.1-R9.7 Repeatability
1	8.1954	8.1137	8.3752	8.7286	8.0229	8.7152
2	8.6144	8.3461	8.5845	8.9441	8.2146	8.6329
3	8.5829	8.5450	8.6485	8.9701	8.2552	9.7248
4	8.6318	8.5582	8.6262	9.0268	8.2004	8.9250
5	8.6236	8.5306	8.6285	9.0439	8.3000	8.8477
6	8.7603	8.5635	8.6746	9.1260	8.3439	9.1860
7	8.8224	8.6727	8.7955	9.1088	8.4434	8.7433